Production mechanisms for inertial instability in the upper troposphere

By

Ian C. Beckley

A dissertation submitted in partial fulfillment of
the requirements for the degree of

Doctor of Philosophy
(Atmospheric and Oceanic Sciences)

at the
UNIVERSITY OF WISCONSIN-MADISON
2026

Date of final oral examination: 27 April 2026

The dissertation is approved by the following members of the Final Oral Committee:

Ángel F. Adames Corraliza, Associate Professor, Atmospheric and Oceanic Sciences
Larissa E. Back, Professor, Atmospheric and Oceanic Sciences
Andrea L. Lang, Associate Professor, Atmospheric and Oceanic Sciences
Jonathan E. Martin, Professor, Center for Climatic Research
Daniel J. Vimont, Professor, Nelson Institute for Environmental Studies

Dissertation Declaration and Approval

I, Ian C. Beckley, declare that this Dissertation titled 'Production mechanisms for inertial instability in the upper troposphere' and the work presented in it are my own.

Ian C. Beckley		
Author	Signature	Date

I hereby approve and recommend for acceptance this work in partial fulfillment of the requirements for the degree of Doctor of Philosophy:

Ángel F. Adames Corraliza		
Committee Chair	Signature	Date
Larissa E. Back		
Faculty Member	Signature	Date
Andrea L. Lang		
Faculty Member	Signature	Date
Jonathan E. Martin		
Faculty Member	Signature	Date
Daniel J. Vimont		
Outside Member	Signature	Date

Abstract

Production mechanisms for inertial instability in the upper troposphere

by Ian C. Beckley

Inertial instability is a hydrodynamic instability that can arise when the local absolute vorticity becomes anticyclonic. This type of instability was long thought to be short lived, if it occurred at all on synoptic scales, since its release is associated with wave-like perturbations which act to re-establish a balanced state. Recent climatological analysis, however, reveals that these events may be more common than previously thought, especially as filamentary features on the equatorward side of the upper-tropospheric jet streams. In addition, there is growing evidence that these events, which are sometimes hazardous to aircraft due to associated clear-air turbulence, may become increasingly common in the near future due to climate change. Generally missing from this discussion, however, have been robust investigations regarding the mechanisms with which these events are produced.

This document is divided into four chapters, the first of which describes a jet-stream-following event climatology, while the remaining three each describe different production mechanisms for inertially unstable conditions. The first of these is an adiabatic mechanism associated with vortex tilitng in regions of large-scale descent. The second considers a moist potential vorticity perspective with discussion tailored to the extra-tropical transition of tropical cyclones. The final chapter describes the production of inertially unstable outflow in the tropical cyclone environment through a dry potential vorticity perspective.

Palmen's emphasis upon examining the underlying mechanisms of individual eddy disturbances was motivated not by their intrinsic interest, but also by an effort to counteract "a tendency to regard what is commonly called the general circulation as nothing but the statistical manifestation of currents as they appear". While valuing the statistical calculation, he felt that their physical nature could only be understood through detailed analyses of characteristic disturbances in the "actual atmosphere". Thus, Palmen regarded the Ferrel circulation as essentially a statistical manifestation of the systematic vertical motion patterns in the disturbances...the sense of whose circulation depends on the reference frame: the indirect Ferrel cell resulting from zonal averaging, the direct circulation resulting from averaging with respect to the meandering polar-front zone itself.

Adapted from Newton (1986)

This work is dedicated to John Pitz, who taught me that math is the universal language.

Acknowledgements

The overarching theme of this doctoral research was influenced by a number of UW-Madison faculty through conversations both in and outside the classroom. In no particular order, Professors Ángel Adames Corraliza, Jon Martin, Greg Tripoli, Michael Morgan, Matt Hitchman, and the included committee members were instrumental in the development of several embedded theses. In addition, I want to thank Professor Angela Rowe for approaching me with kindness and understanding during a period of disengagement. Professor Elizabeth Maroon provided critical professional guidance, especially when I served as her teaching assistant. Professors Nick Metz, Neil Laird, and Jon Forde of Hobart and William Smith Colleges provided terrific undergraduate teaching/mentorship.

This work was supported by NSF Award AGS-2236433. Professor Ángel F. Adames Corraliza provided steady, attentive mentorship throughout my PhD studies. I thank him and the members of his laboratory for their friendship and constructive criticism which contributed greatly to the quality of this document.

The manuscript constituting Chapter 2 benefited from constructive criticism by Dr. Michael C. Morgan, Dr. Jonathan E. Martin and three anonymous reviewers.

The manuscript constituting Chapter 3 benefited from constructive criticism by Dr. Andrew C. Winters, Dr. Alexander Lojko, and two anonymous reviewers. We thank Dr. Michael A. Sprenger for his assistance with the Lagrangian analysis tool, and acknowledge Dr. Jon E. Martin, Dr. Greg Tripoli, and Dr. Matt Hitchman for many insightful conversations. The MPAS simulation of Hurricane Fiona was performed on the National Center for Atmospheric Research's Derecho supercomputer thanks to extra compute time organized by Dr. May Wong, Dr. Bill Skamarock, and Michael Duda after the corresponding author's attendance to an MPAS tutorial in September 2025.

Contents

List of Figures

List of Tables

Chapter 1

A jet-following climatology of anticyclonic absolute vorticity

1.1 Primer

Inertial instability can arise in regions of strong anticyclonic vorticity when the product of the Coriolis parameter (f) and the geostrophic absolute vorticity (η_g) is negative (van Mieghem, 1951). In such environments, small cross-flow parcel displacements result in an imbalance between local pressure gradient and Coriolis forces. The net acceleration is in the direction of initial displacement, the flow re-arranges irreversibly, and perturbations grow exponentially at the rate of $F = \sqrt{f\eta_g}$, the inertial frequency controlling the oscillatory behavior of perturbations. These unstable perturbations mix momentum laterally, thus decreasing the horizontal shear until inertial stability is restored (Stone,

1972, Holton and Hakim, 2013). This can be thought of as an analog to static instability, the release of which results in convective turbulence which re-instates a dry-adiabatic lapse rate from one that is superadiabatic. Given that inertial instability is associated with strongly anticyclonic flow, two potential regions for large-scale instability arise in the mid-latitude upper troposphere: 1) along the anticyclonic shear side of intense jet streaks and 2) the interior of strong anticyclones.

With the release of inertial instability posing a distinct dynamical limit on the growth of anticyclonic disturbances, it is not unreasonable to assume that persistent regions of inertial instability be rare on synoptic scales (e.g. Holton, 1979, their pg. 216). Indeed, despite early observational evidence suggesting the presence of instability on the equatorward side of jet streaks (Schaefer and Hubert, 1955), the issue remains contested into the 21st century (e.g. Holton and Hakim, 2013, pg. 139). Thompson et al. (2018) provide a robust history of this disagreement while introducing their modern climatology of inertial instability events in the upper-troposphere. Their findings agree with several contemporary analyses that events are more common than previously thought (Sato and Dunkerton, 2002, Knox and Harvey, 2005, Lojko et al., 2024, Beckley and Corraliza, 2026).

The main purpose of this document is to describe the physical mechanisms responsible for the production of inertial instability in the large-scale flow. Chapter 2 describes the

production of inertial instability events in clear-sky environments associated with quasi-geostrophic (QG) subsidence. Chapter 3 describes the role of diabatic heating in producing inertial instability events through a moist potential vorticity (MPV) framework. Finally, Chapter 4 applies an existing potential vorticity (PV) perspective to negative PV production in the tropical cyclone environment. The remainder of Chapter 1 introduces basic inertial instability criteria and demonstrates their application to a jet-following event climatology. A more rigorous discussion of inertial instability criteria appears in Chapter 2.1.

1.2 Motivation for a jet-following event climatology

The mid-latitude upper troposphere is characterized by climatological westerly winds which maximize in what are known as jets or jet streams. The prevailing notion is that separate subtropical and polar jet streams exist throughout the year (bimodality, e.g. Manney and Hegglin, 2018), the former associated with angular-momentum conserving convective outflow in the tropics, the latter an "eddy-driven" jet consistent with a strong mid-latitude temperature gradient. While it is well-known that these distinct jet features retract poleward in the summer hemisphere (e.g. Fleming et al., 1987), recent investigations by Martin (2021), Martin and Norton (2023), and Orr (2024) indicate that the warm-season jet structure is more unimodal than previously thought. Each of these distinct jets (cold-season subtropical/polar and warm-season unimodal) can be characterized climatologically in specific isentropic layers via a core isertel, the line of constant PV upon which the circulation maximizes. While the physical reasoning as to why the jet streams

reside in specific isentropic and isertellic layers on any given day remains an interesting research question, it has become increasingly clear that seasonal analysis of jet-level features will have increased fidelity using the seasonally bimodal/unimodal paradigm.

One jet-level phenomenon which has historically enjoyed relatively little attention is inertial instability (i.e. where the absolute vorticity is signed oppositely the Coriolis parameter). This instability has, however, been linked to clear-air turbulence (CAT) hazardous to aircraft (Knox, 1997, Thompson and Schultz, 2021), and the size of anticyclonic absolute vorticity is embedded in several CAT indicators. This research area is receiving renewed attention from the aviation industry due to projections that clear-air turbulence may become substantially more likely in the future, a seemingly non-linear response to external forcing on our climate system (Williams, 2017, Storer et al., 2017). Asymmetry in the climatological distribution of inertial instability events appears to closely match that associated with the northern-hemispheric storm tracks (Hoskins and Valdes, 1990, Thompson et al., 2018), thus there is likely an intimate relationship between changes in the mid-latitude storm track and inertial instability (and therefore CAT) in global climate models.

This relationship is best described physically using the several inertial instability production mechanisms discussed in Chapters 2–4, however, the remainder of Chapter 1 is dedicated to a simple inertial instability identification method. Combined with the jet-identification methodology of Martin (2021), a similar study could be easily applied to a variety of global climate models for jet-following investigations of inertial instability

occurrence. The subsequent section describes basic inertial instability criteria. Chapter 1.4 contains relevant methodology and details the isentropic housings and core isertels for the seasonal jet streams. Chapter 1.5 includes a global climatology of inertial instability, and Chapter 1.6 presents discussion, with special attention to the application of this methodology to future climate simulations.

1.3 Basic inertial instability theory and criteria

Inertial instability is a fundamental hydrodynamic instability arising from an imbalance between local pressure-gradient and Coriolis forces (van Mieghem, 1951). When conditions for instability are present, horizontally displaced fluid parcels accelerate away from their initial locations, the fluid rearranges irreversibly, and wave-like perturbations arising from the release of instability mix momentum along isentropes until stability is returned (Holton and Hakim, 2013). The traditional criterion for the presence of inertial instability is when the product of the geostrophic absolute (η_g) and planetary vorticity (f, the Coriolis parameter) is negative,

$$\eta_g f < 0, \tag{1.1}$$

where η_g is the sum of geostrophic relative (ζ_g) and planetary vorticity (Cushman-Roisin and Beckers, 2011, see their Ch. 17.2). Since ζ_g can be partitioned into shear (ζ_s) and curvature (ζ_c) components (e.g. Bell and Keyser, 1993), Eq. (1.1) can be re-written

$$(\zeta_s + \zeta_c + f)f < 0, \tag{1.2}$$

and candidate regions for instability arise: 1) the interior of strong anticyclones where both ζ_c and ζ_s are anticyclonic, and 2) the anticyclonic shear side of strong jet streaks where ζ_s is strongly anticyclonic and ζ_c small. Both of these phenomena manifest as perturbations along the mid-latitude, upper-level westerlies and can be identified using analyses of geostrophic streamfunction.

There is some debate as to whether the instability criterion as derived for a geostrophic flow is representative in regions where curvature is important (see Appendix B.3). This issue arises near trough and ridge axes where the flow is sub and super geostrophic, respectively, and gradient balance is more appropriately assumed. For example, the anticyclonic shear side of an upper-level jet streak embedded in a trough (ridge) may appear inertially unstable (stable) from the geostrophic perspective, but stable (unstable) using the full flow. Further, it is worth considering whether or not derivations of inertial stability criteria (whose equilibrium states are geostrophic or gradient balance) have much meteorological significance in the deep tropics. That said, in agreement with a recent global climatology by Thompson et al. (2018), we substitute the full-flow absolute vorticity (η) for its geostrophic counterpart in Eq. (1.1) such that the inertial instability criterion becomes

$$\eta f < 0. \tag{1.3}$$

This introduces the possibility of under (over) estimations of inertial instability events in troughs (ridges). The anticyclonic shear sides of relatively straight jet streaks, however, should be captured regardless of choice.

Although it was historically contested whether inertial instability actually occurs on synoptic scales (Knox, 1997, see their Section 3), it is now generally accepted that events are relatively common on the anticyclonic shear side of mid-latitude jet streaks (Oertel et al., 2020, Harvey et al., 2020, Lojko et al., 2024, Beckley and Corraliza, 2026). The most recent global climatology (Thompson et al., 2018, as of writing) focuses solely on the 250, 500 and 850 hPa isobaric surfaces. While the 250 and 500 hPa surfaces frequently intersect the cold-season subtropical and polar jets, respectively, the use of these surfaces arises implicitly from standard forecast practices rather than objective analysis. Provided new knowledge regarding the seasonality of specific mid-latitude jet streams (e.g. Orr, 2024), there is a distinct opportunity to perform an inertial instability climatology with increased spatial and seasonal fidelity. That said, we do not intend to be overly critical of the antecedent climatology. A particular goal of this investigation is to identify inertial instability events as they relate to the upper-level jet streams, something that should not be assumed of all prior literature.

1.4 Methods

Computations were performed in a meteorological python environment (May et al., 2016, 2022) using the 6-hourly, 1.25° Japanese Reanalysis for Three Quarters of a Century (JRA3Q, Kosaka et al., 2024) which recently superseded the Japanese 55-year Reanalysis (JRA55, Kobayashi et al., 2015). Although the JRA3Q is available in isentropic coordinates at 10 K intervals, isobaric fields of relative vorticity (45 vertical levels, every 50 hPa in the mid- and upper troposphere) were interpolated to isentropic coordinates at 5 K intervals consistent with Orr (2024). Given questions regarding the fidelity of reanalysis data prior to the widespread use of geostationary satellite observation, analysis was restricted to 1979–2024.

The specific seasonality, isentropic layers, and core isertels which define the jet streams are provided in Tables 1 & 2 for both the Northern and Southern Hemispheres. These jets were identified in isentropic space by recording the isentropic level upon which local winds maximize at each analysis period. The jets are further isolated in horizontal space by identifying the isertel upon which the horizontal circulation per unit area maximizes in each analysis period. This is called the "core isertel," the mean of which effectively defines the climatological jet in a given isentropic layer. This identification method is particularly robust due to the relationship between balanced wind speed and the horizontal PV gradient (Hoskins et al., 1985). While the values employed here were chiefly identified in the analysis by Orr (2024), their methodology is nearly identical to that used by Martin (2021) & Martin and Norton (2023).

The presence of inertial instability is evaluated at each point in the 6-hourly JRA3Q using

$$(\zeta + f)f < 0, \tag{1.4}$$

where f and ζ are the planetary and full-flow relative vorticities, respectively. In order to reduce errors associated with finite-differencing on non-native grids, Eq. (1.4) was calculated using the JRA3Q model-output relative vorticity. Instances of inertial instability were counted and averaged across the isentropic layer characteristic of each jet for the corresponding month (see Table 1.1). Data was then subset and averaged across months depending on jet modality (see Table 1.1). This results in a frequency distribution of inertial instability events for the subtropical, polar and warm-season unimodal jets. In addition, we have calculated the percentage of time a grid point experiences inertial instability relative to the expectation at that latitude, a pseudo-zonal anomaly field that helps identify regional differences in event occurrence.

The potential vorticity (PV) was calculated using the approximation

$$P \approx -g\frac{\partial\theta}{\partial p}(\zeta + f), \tag{1.5}$$

where g is the Earth's gravitational acceleration and ζ is the full relative vorticity (Holton and Hakim, 2013, , see their Eq. 4.28). This approximation is best for quasi-geostrophic flows (i.e. where the Rossby number is small) and has utility in this application since

TABLE 1.1: Isentropic housings (K) for the upper-tropospheric jet streams in the JRA55 (Orr, 2024). When one interval is provided the jet is unimodal. Independent polar and subtropical jets exist when two intervals are separated by an em-dash. The subtropical jet is always found at higher potential temperatures than its polar counterpart.

Month	Northern Hemisphere	Southern Hemisphere
Nov	*Transition*	315–330
Dec	310–325 — 335–350	320–335
Jan	310–325 — 340–355	325–340
Feb	310–325 — 340–355	320–335
Mar	315–330 — 340–355	320–335
Apr	*Transition*	*Transition*
May	330–345	310–325 — 340–355
Jun	335–350	310–325 — 335–350
Jul	330–345	310–325 — 335–350
Aug	330–345	310–325 — 335–350
Sep	330–345	310–325 — 340–355
Oct	325–340	*Transition*

the resulting isertels have improved representation near regions of extreme terrain (e.g. Andean and Himalayan Mountains). Since the upper troposphere is almost always statically stable (i.e. $-\frac{\partial\theta}{\partial p} > 0$), this approximate PV also contains information regarding the inertial stability. Use of Eq. (1.4) produced nearly identical results over a subset period when $(\eta + f)$ is substituted for the full Ertel's PV available in the JRA55 & JRA3Q. We elect to use the traditional criterion [Eq. (1.4)], however, as it greatly reduces the amount of requisite data.

TABLE 1.2: Climatological core isertels (PVU, rounded to the tenths place) for each upper-tropospheric jet (Martin, 2021, Martin and Norton, 2023, Orr, 2024). NH and SH refer to the Northern and Southern Hemispheres, respectively

Jet	JRA3Q/JRA55 core isertel (PVU)
NH Polar	2.4
NH Subtropical	2.1
NH Unimodal	3.0
SH Polar	-1.3
SH Subtropical	-1.9
SH Unimodal	-3.1

1.5 Results

1.5.1 Boreal polar jet

The Boreal polar jet is defined between Dec–Mar in, approximately, the 320–335 K isentropic layer. Its climatological location is between 30–35°N, with notable asymmetry arising in both the northeastern Pacific and Atlantic basins. Both of these locations lie immediately east of distinct local maxima in inertial instability occurrence, the first of which extends from the South China/Philippine Seas towards Japan, then eastward across the central Pacific (Fig. 1.1b). Inertial instability occurs approximately 4.25% of the time immediately east of Luzon, and a similar amount of time in the Gulf of Thailand (Fig. 1.1a). Events are less common throughout the central Pacific (<1.75% of the time), though the local maximum extends over about 60° longitude.

The other primary zonal anomaly in event occurrence extends from the mid-Atlantic region of the United States, through the coastal Canadian Maritime, and eastwards towards Great Britain (Fig. 1.1b). Inertial instability is expected about 0.75% of the time in this

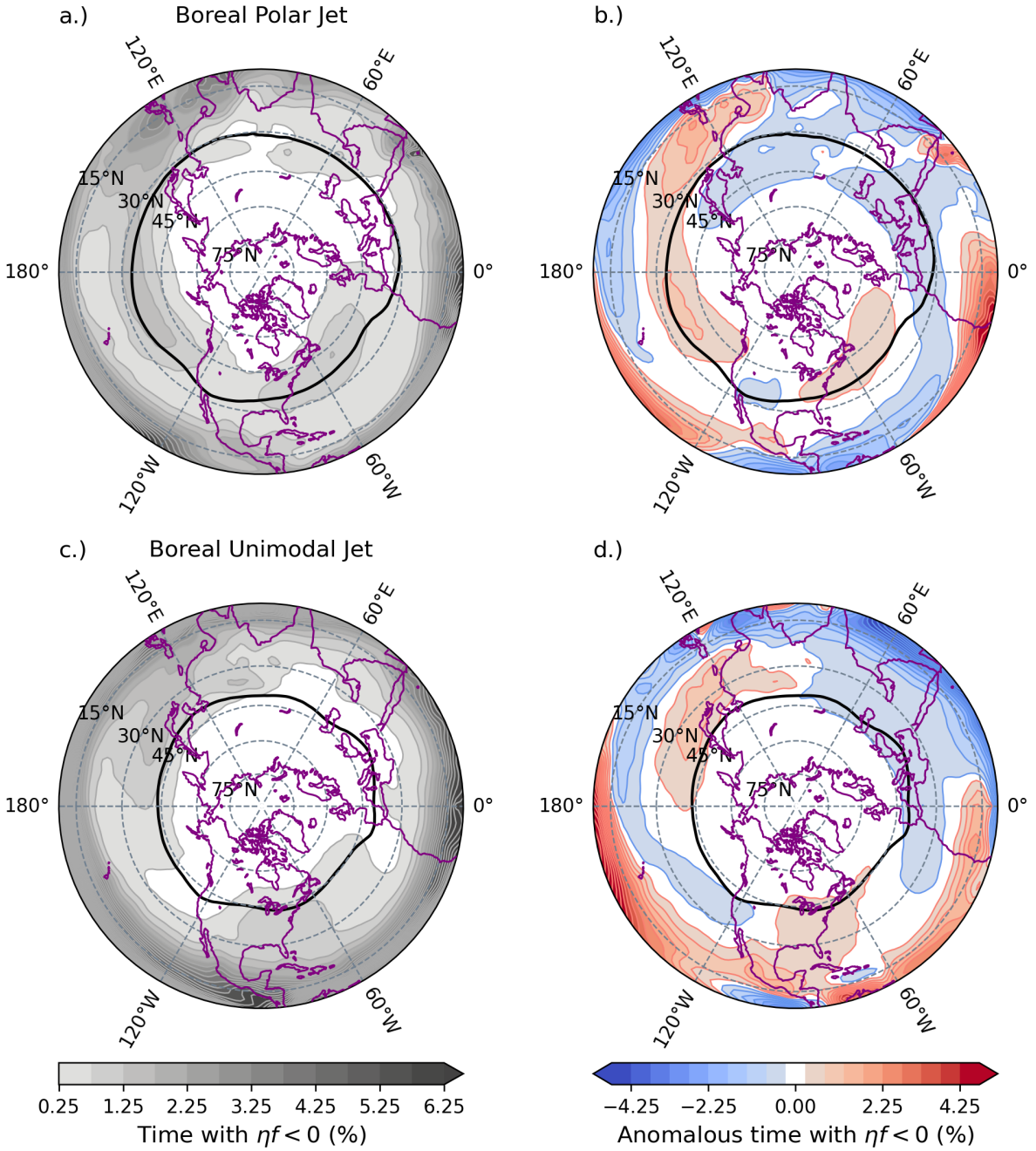

FIGURE 1.1: a.) Percentage of time with $\eta f < 0$ in the isentropic layer defining the Boreal polar jet (see Table 1.1), the climatological location of which is defined by the 2.4 PVU isertel (solid black). b.) As in a.), except the anomalous time with $\eta f < 0$ (percent) relative to the expectation at that latitude. c.) as in a.) except for the Boreal unimodal jet, the climatological location of which is given by the 3.0 PVU isertel (solid black). d.) as in b.) except for the Boreal unimodal jet.

region, though the 0.25% contour extends from the Pacific, across the United States to far-western Europe (Fig. 1.1a). There is a notable minimum in event occurrence extending across much of Europe and Eurasia (Fig. 1.1b).

1.5.2 Boreal unimodal jet

The Boreal unimodal jet is defined between the months May–Oct in, approximately, the 330–345 K isentropic layer. Its typical latitude is near 45°N (Fig. 1.1c). While the near-jet local maximum in inertial instability event occurrence are similar to that observed for the polar jet (Fig. 1.1a), note that closed contours are not present in the northwestern Atlantic or Pacific Oceans (Fig. 1.1c). The local maximum in the northwest Atlantic extends further westward into the continental United States. Simultaneously, events are rarer in the north-central Atlantic and far-western Europe than for the Boreal polar jet (Fig. 1.1a & c). The region of increased event expectation over far-eastern Asia now extends from the Korean Peninsula, across southern Japan till its end near the date line (Fig. 1.1d).

1.5.3 Boreal subtropical jet

The Boreal subtropical jet is defined between the months of Dec–Mar in, approximately, the 340–355 K isentropic level. Note that events are far more common along this particular jet stream, with inertial instability occurring between 1–6 % of the time immediately equatorward of the climatological jet (Fig. 1.2a). The 1% contour is nearly congruent with the 2.1 PVU isertel, further confirmation that inertial instability is effectively confined

to the equatorward side of the subtropical jet (in this isentropic layer). The gradient in event occurrence is strong from 8–18°N in northern South America, central Africa, and across the Atlantic Ocean. This is also true in the central Pacific, however, events are less common in this region (Fig. 1.2b).

Those deep-equatorial regions of high event occurrence, however, are relatively far from the subtropical jet itself (Fig. 1.2a). Zonal anomalies in event occurrence which occur along the subtropical jet extend across the central Atlantic (events are relatively rare) and along an east-northeast axis extending from Myanmar into the west-central Pacific (Fig. 1.2b). The local maximum in event occurrence in central Africa does, however, extend poleward into southeast Asia where it is in close proximity to the climatological jet.

1.5.4 Austral subtropical jet

Compared to the Boreal subtropical jet, the Austral subtropical jet is strongly symmetrical about the 28°S parallel (Fig. 1.2c). This jet stream is defined between the months of May–Sep in, approximately, the 335–350 K isentropic layer. There is some likeness with its Boreal counterpart in that events are quite common in the deep-tropical regions of South America, Africa and the central Atlantic (Fig. 1.2a & c). There are more events, however, observed in the far eastern Pacific and over Oceania. Like its Boreal counterpart, the core isertel dips equatorward when the number of instability events is low relative to the expectation at that latitude (Fig. 1.2b & d).

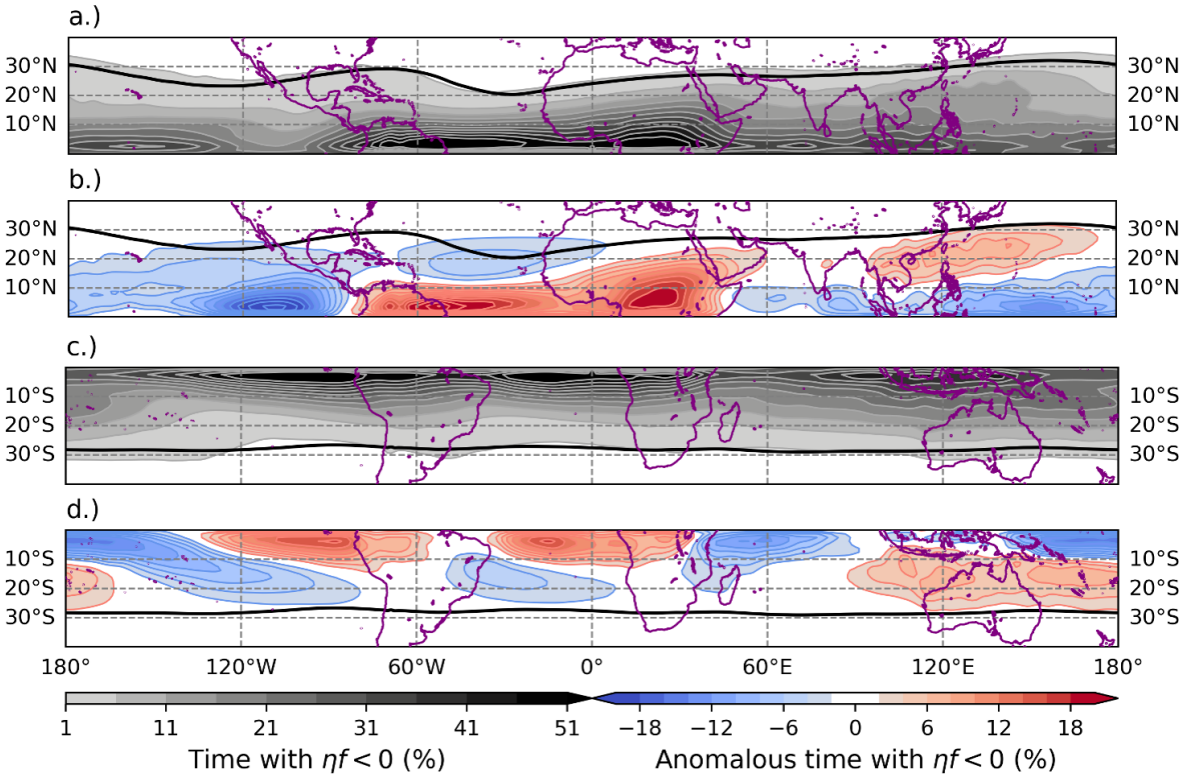

FIGURE 1.2: a.) Percentage of time with $\eta f < 0$ in the isentropic layer defining the Boreal subtropical jet (see Table 1.1), the climatological location of which is defined by the 2.1 PVU isertel (solid black). b.) As in a.), except the anomalous time with $\eta f < 0$ (percent) relative to the expectation at that latitude. c.) as in a.) except for the Austral subtropical jet, the climatological location of which is given by the -1.9 PVU isertel (solid black). d.) as in b.) except for the Austral subtropical jet.

1.5.5 Austral polar jet

The Austral polar jet is defined by the -1.3 PVU isertel in the 310–325 K isentropic layer from May–Jun. Its most poleward extent is found from 20–80°E when the climatological jet location is between 42–44°S (Fig. 1.3a). In other parts of the hemisphere it is found from 38–42°S. Inertial instability is relatively common in a near-jet region extending from eastern South America to the 0° meridian between 30–40°S (Fig. 1.3b). Another region where inertial instability is relatively common extends from deep-tropical Oceania, along

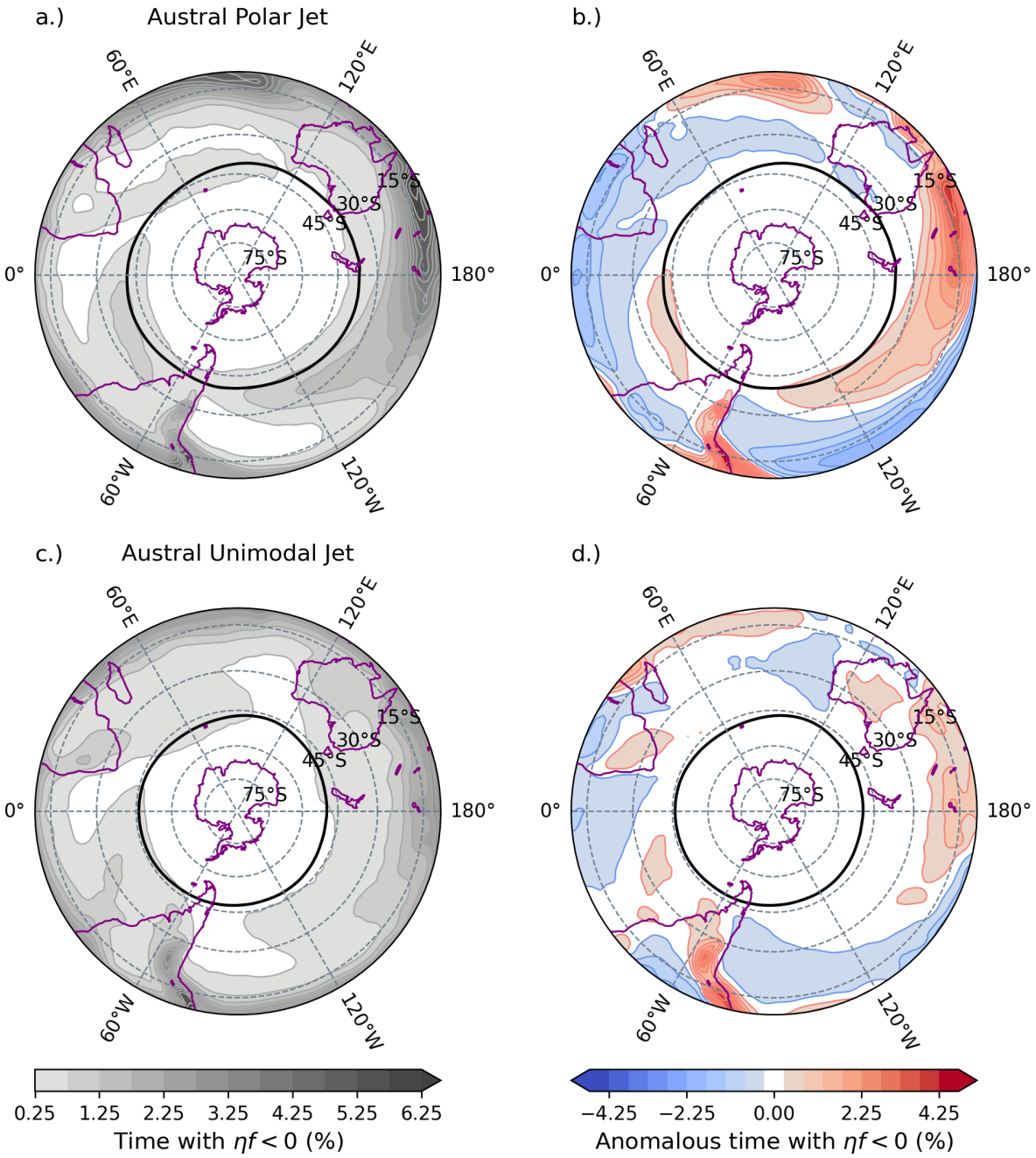

FIGURE 1.3: a.) Percentage of time with $\eta f < 0$ in the isentropic layer defining the Austral polar jet (see Table 1.1, the climatological location of which is defined by the -1.3 PVU isertel (solid black). b.) As in a.), except the anomalous time with $\eta f < 0$ (percent) relative to the expectation at that latitude. c.) as in a.) except for the Austral unimodal jet, the climatological location of which is given by the -3.1 PVU isertel (solid black). d.) as in b.) except for the Austral unimodal jet.

northern Australia and east-southeastward across the Pacific Ocean where, by 120°W, it reaches 40°S (Fig. 1.3b). The subtropical Indian Ocean is associated with relatively few events compared to other subtropical locations. It is unclear whether the region of enhanced event occurrence along the southern extent of the Andes Mountains is a real depiction of inertial instability events or an error originating due to high terrain.

1.5.6 Austral unimodal jet

The Austral unimodal jet is defined by the -3.1 PVU isertel in, approximately, the 335–350 K isentropic layer from May through September (Fig. 1.3c). There are relatively few notable zonal asymmetries arising immediately adjacent the jet, and, unlike most other jet features, zonal asymmetries that do arise do not necessarily become increasingly intense in the sub and deep tropics (Fig. 1.3d). Events are still relatively common in the deep and subtropical region southeast of Australia, through the date line and to about 160°E.

1.6 Discussion

The distribution of events along the polar and unimodal jets in both hemispheres are strongly suggestive of a relationship to the mid-latitude storm tracks (Hoskins and Valdes, 1990, Hoskins and Hodges, 2005). The physicality of this relationship is supported by a growing body of work indicating that negative PV (and, thus inertial instability) can arise due to sub-synoptic diabatic heating in the warm-conveyor belt airstream of mid-latitude cyclones (Harvey et al., 2020, see our Chapter 4 for discussion). That said, there are

also large-scale regions of enhanced event occurrence which originate from the deep and subtropics, especially in the Pacific Ocean basin. These regions are likely reflective of convective outflow associated with the Hadley cell circulation (e.g. Sato and Dunkerton, 2002). The extension of this feature into mid-latitudes is potentially associated with the downstream transport of existing unstable features and/or the role of convective outflow in invigorating the Pacific storm track in both hemispheres.

One limitation of this methodology is that it specifically targets the upper-tropospheric jet stream environment and, thus, potentially overlooks other regions where inertial instability is observed such as the Somali jet, low-level "tip jets" arising due to orography, mountain-gap flow and, in the subtropical high (Thompson et al., 2018). While this limitation can be overcome using different methodological choices in regional analyses, the advantage of this jet-following methodology is that it evaluates the event distribution associated with each respective upper-level jet. For example, it is shown in Fig. 1.1a that a closed contour of high event occurrence is present over the Northwestern Atlantic. This is a strong indication that inertial instability events in this region do not always originate in sub or deep tropical convective outflow; some events are produced *in situ*.

Given recent indications that inertial instability events (and CAT) may become increasingly common due to external forcing on the climate system (Williams, 2017, Storer et al., 2017), application of this methodology to global climate models goes as follows. First, one must confirm the preferred isentropic layers and core isertels of upper-level jet features (these will likely change in a warmer climate) following the methodology of Martin

(2021). Once the isertellic and isentropic housings for each seasonal jet are known (like those included in Tables 1.1 & 1.2), one may evaluate a variety of jet-level phenomena such as inertial instability occurrence. One can then compare past, present, and future distributions of inertial instability occurrence by the respective jet, rather than isobaric level. While this does not imply that isobaric evaluations of event occurrence are without value, note that mid-latitude inertial instability events are directly linked to gradients in upper-level winds due to requisite anticyclonic relative vorticity. From this perspective, the "native" coordinate with which to evaluate inertial instability events in middle latitudes is one which follows the jet itself.

Chapter 2

Persistence and adiabatic generation of inertial instability on the equatorward side of upper-level jet streaks

2.1 Introduction

Inertial instability can arise in regions of strong anticyclonic shear when the product of the Coriolis parameter (f) and the geostrophic absolute vorticity ($\eta_g = \zeta_g + f$) is negative (van Mieghem, 1951). In such environments, small cross-flow parcel displacements result in an imbalance between local pressure gradient and Coriolis forces. The net acceleration is in

the direction of initial displacement, the flow re-arranges irreversibly, and perturbations grow following

$$\Delta x = X \exp(iFt), \tag{2.1}$$

where x is the horizontal displacement, X an initial displacement, and $F = \sqrt{f\eta_g}$, is the inertial frequency controlling the oscillatory behavior of perturbations. These unstable perturbations mix momentum laterally along isentropes, thus decreasing the horizontal shear until inertial stability is restored (Stone, 1972, Holton and Hakim, 2013). These disturbances were associated with weak to moderate clear air turbulence in a recent idealized simulation by Thompson and Schultz (2021), further corroborating evidence of clear-air turbulence in flights on the anticyclonic flank of strong upper-level jets (e.g. Mogil and Holle, 1972, Knox, 1997).

With the release of inertial instability posing a distinct dynamical limit on the growth of quasi-geostrophic (QG) anticyclonic disturbances, it is not unreasonable to assume that persistent regions of inertial instability be rare on synoptic scales (e.g. Holton, 1979, their pg. 216). Indeed, despite early observational evidence suggesting the presence of instability on the equatorward side of jet streaks (Schaefer and Hubert, 1955), the issue remains contested into the 21st century (e.g. Holton and Hakim, 2013, pg. 139). Thompson et al. (2018) provide a robust history of this disagreement while introducing

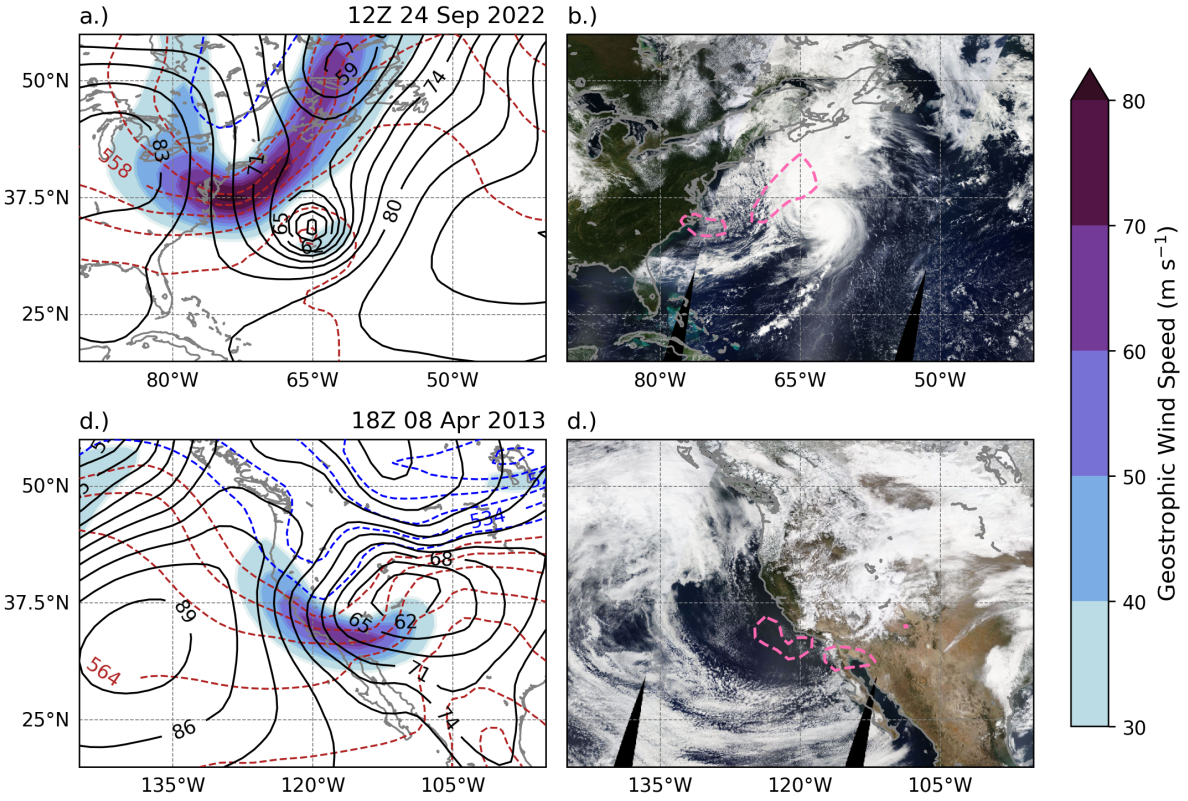

FIGURE 2.1: a.) 1000–500 hPa thickness (dashed red every 6 dam, changing to blue at 540 dam), 925 hPa geopotential heights (solid black every 3 dam), and 300 hPa geostrophic wind speed (shaded) at 12Z on 24 Sep 2022. b.) Anticyclonic geostrophic absolute vorticity at 300 hPa (dashed pink) upon composite visible satellite imagery from mid-day on 24 Sep 2022 during the extra-tropical transition of Hurricane Fiona. c.) As for a.) except with 400 hPa geostrophic wind speed (shaded) at 18Z on 8 April 2013. d.) as for b.) except for anticyclonic geostrophic absolute vorticity at 400 hPa and imagery from the afternoon of 8 April 2013 during the development of a strong upper-level jet streak.

their modern climatology of inertial instability events in the upper-troposphere. Their findings agree with several contemporary analyses that events are more common than previously thought (Sato and Dunkerton, 2002, Knox and Harvey, 2005, Lojko et al., 2024). The distribution of events is asymmetric about the mid-latitude upper troposphere, with preferred regions extending across the Pacific and Atlantic oceans in the Northern Hemisphere (Thompson et al., 2018, see their Figs. 1, 2 & 3).

Harvey et al. (2020) investigated regions of inertial instability along the North Atlantic jet using a potential vorticity (PV) perspective. They found that the appearance of negative Ertel's PV (and anticyclonic absolute vorticity) was sometimes associated with sub-synoptic diabatic heating in the presence of strong vertical wind shear. This phenomenon was evident during the extra-tropical transition of Hurricane Fiona (Fig. 2.1a-b). Robust cloud coverage associated with the post-tropical cyclone was embedded in the anticyclonic shear side of a strong upper-level front/jet with inertial instability in its equatorward exit. This diabatic production mechanism is thought to manifest in the warm conveyor belt of mid-latitude cyclones (Oertel et al., 2020, see their Fig. 13), and Grams and Archambault (2016) indicated similar regions of negative PV arise during the extra-tropical transition of tropical cyclones in the Northwest Pacific (see their Fig. 8c). Given their relationship to diabatic heating, this variety of inertial instability event is typically found downstream of large-scale trough axes (Lojko et al., 2024, see their Fig. 6a & 6b).

In their climatology of negative PV-jet interactions, Lojko et al. (2024) implicitly indicated that inertial instability can arise at jet-level seemingly without direct association with convection. Anecdotally, these events often occur in environments characterized by synoptic-scale descent (and, thus, clear skies); for example, in northwesterly flow upstream of an upper-level trough axis (e.g. Fig. 2.1c-d). Such events can persist even in cyclonic curvature, an indication that shear vorticity plays a vital role (Hakim, 2000, see their Fig. 4). The goal of this study is to evaluate whether dry processes alone are sufficient to generate anticyclonic geostrophic absolute vorticity that persists over several

analysis periods on near-synoptic scales. The subsequent section addresses event persistence by comparing the e-folding timescale of inertial instability with parcel residence time in strong jets. It is later argued that tilting of horizontal vorticity by differential QG vertical motion in the jet entrance/exit regions is the mechanism which modulates the sign of absolute vorticity following the flow. This process is illustrated in both real and idealized cases of robust upper-level jet development in regions of synoptic-scale descent.

2.2 Persistence of inertial instability near upper-level jets

Cushman-Roisin and Beckers (2011, see their Ch. 17.2) provide a detailed derivation of hydrodynamic instability criteria using a two-dimensional system of linear, ordinary differential equations describing the evolution of parcel displacements in the lateral (x) and vertical (z), directions for a meridional flow (v),

$$\frac{d^2\Delta x}{dt^2} - f\Delta v = -\frac{1}{\rho_0}\left(\frac{\partial^2 p}{\partial x^2}\right)\Delta x - \frac{1}{\rho_0}\left(\frac{\partial^2 p}{\partial x \partial z}\right)\Delta z \tag{2.2}$$

$$\frac{d^2\Delta z}{dt^2} = -\frac{1}{\rho_0}\left(\frac{\partial^2 p}{\partial x \partial z}\right)\Delta x - \frac{1}{\rho_0}\left(\frac{\partial^2 p}{\partial z^2}\right)\Delta z, \tag{2.3}$$

where ρ_0 is the mean density of dry air, f is the Coriolis parameter, p is pressure, t is time and Δx and Δz are horizontal and vertical displacements, respectively. Assuming

an f-plane, $\Delta v = -f\Delta x$ and, Eqs. (2.2) & (2.3) have solutions

$$\Delta x = X \exp(i\Omega t) \tag{2.4}$$

$$\Delta z = Z \exp(i\Omega t), \tag{2.5}$$

where Ω controls the growth/decay of horizontal and vertical displacements and is defined

$$\Omega^2 = \frac{F^2 + N^2 \pm \sqrt{(F^2 - N^2)^2 + 4G^4}}{2}, \tag{2.6}$$

where $F^2 = f\eta_g$ is the inertial frequency, N^2 the Brunt-Väisälä frequency, and $G^2 = f_0\frac{\partial v}{\partial z}$, is the strength of thermal wind balance. Instability arises when Ω has a non-zero imaginary component. For the case of pure horizontal shear instability (e.g. at jet level where $|\frac{\partial u}{\partial z}| << |\frac{\partial v}{\partial x}|$), N^2 and $G^2 \rightarrow 0$ such that $\Omega = F$ and the time taken for displacements associated with the release of inertial instability to grow by a factor of e is

$$\tau_i = \frac{1}{\sqrt{f\eta_g}}, \tag{2.7}$$

where η_g is the sum of planetary (f) and geostrophic relative (ζ_g) vorticity.

Consider an intense mid-latitude jet like that diagnosed from isohypses near 35°N, 120°W in Fig. 2.2b. When a parcel traveling along the equatorward side of the jet passes through the $\eta_g \approx 0$ isopleth, f and ζ_g must be of the same order and oppositely signed such that their sum is a small residual (i.e. $\eta_g \approx 1 \times 10^{-5}$ s^{-1}). Taking f and ζ_g on the order of 1×10^{-4} s^{-1},

$$\tau_i \approx \frac{1}{\sqrt{10^{-4}\ \text{s}^{-1} \times 10^{-5}\ \text{s}^{-1}}}, \tag{2.8}$$

about 9 hours. Compare this with the time it takes for a parcel to travel through the jet streak itself,

$$\tau_{\text{adv}} \approx \frac{L}{U}, \tag{2.9}$$

where U is the wind speed and L is the length of the anticyclonic absolute vorticity feature. If $U \approx 50$ m s^{-1} and $L \approx 10^6$ m, τ_{adv} is only about 6 hours. This approximation is best for slowly propagating and quasi-stationary phenomena (i.e. feature celerity << embedded windspeeds).

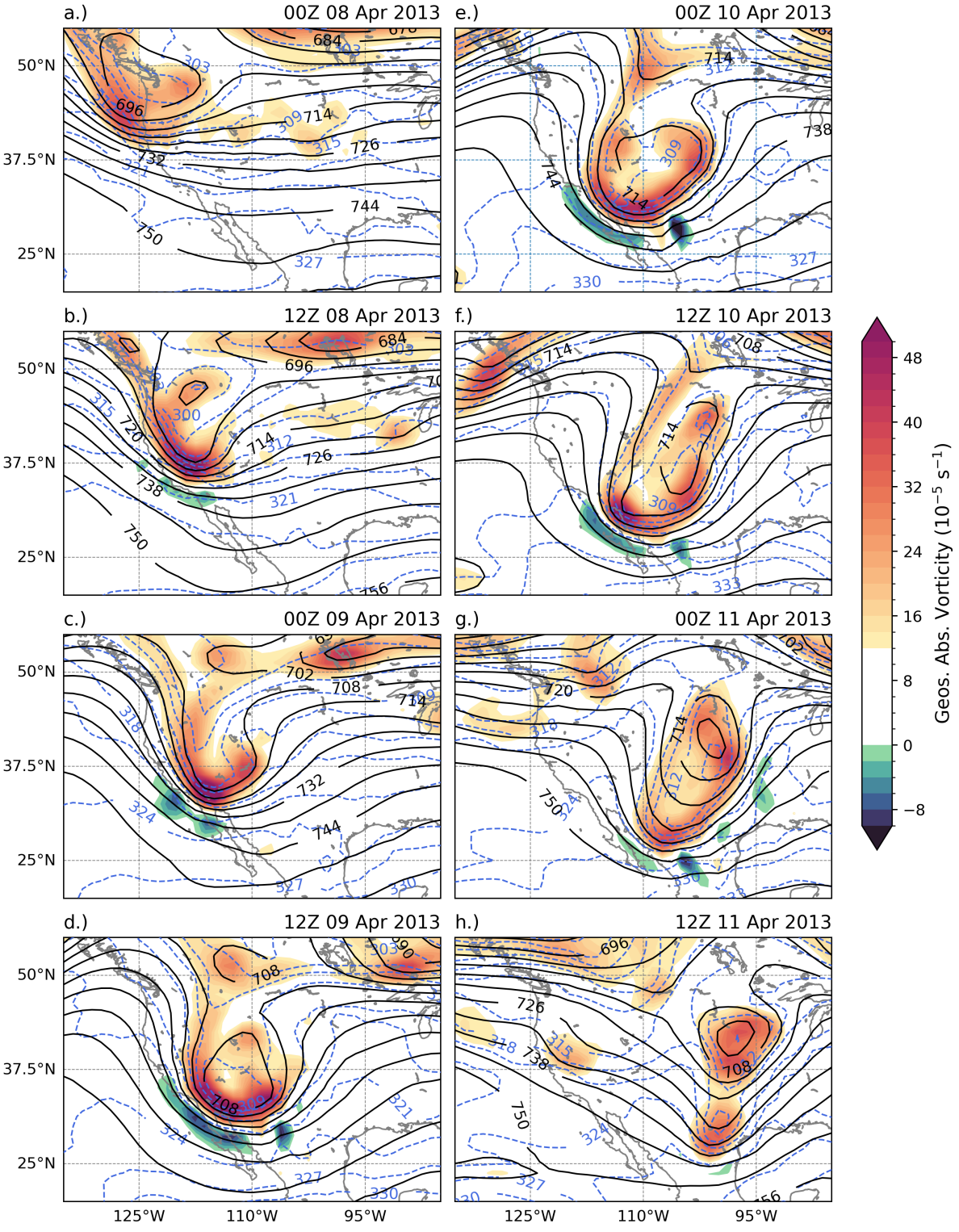

FIGURE 2.2: a.) 400 hPa geopotential height (solid black every 6 dam), potential temperature (dashed blue every 3 K) and geostrophic absolute vorticity (shaded) at 00Z 8 April 2013. b-h.) as in a.) except at the labeled time.

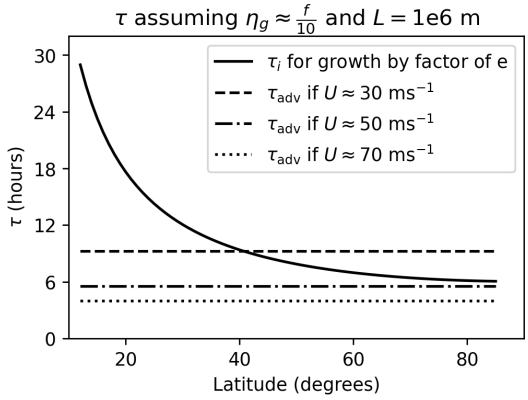

FIGURE 2.3: τ_{adv}, the time required for parcels traveling at 30, 50, and 70 m s^{-1} to pass through a 1000 km jet streak (black dashed, dash-dotted and dotted, respectively), and τ_i, the time required for unstable disturbances to grow by an order of e, calculated assuming $\eta_g = \frac{f}{10}$ and plotted as a function of latitude (solid black).

Fig. 2.3 contains lines of approximate τ_{adv} for hypothetical 1000 km jet streaks of 30, 50 and 70 m s^{-1} (dashed, dash-dotted, and dotted lines, respectively). The time required for unstable disturbances to grow by an order of e (solid) is calculated assuming that $\eta_g \sim \frac{f}{10}$ and plotted as a function of latitude. Even for a jet streak of approximately 50 m s^{-1} (dash-dotted line), $\tau_i > \tau_{\text{adv}}$ across subtropical and middle latitudes. This inequality grows for faster winds (dotted line) and shorter jet streaks (smaller L, not shown). Parcels flowing along the anticyclonic shear side of an upper-level jet may exit the region of instability before displacements associated with the release of inertial instability grow to meaningful size. This indicates that regions of anticyclonic geostrophic absolute vorticity associated with shear vorticity can be relatively long-lived, especially if there is a persistent production mechanism.

2.3 Adiabatic production of inertial instability

The prevailing paradigm describing the distribution of vertical motion in the vicinity of upper-level jet streaks arises from the Sutcliffe-Trenberth form of the (QG) ω-equation,

$$\left(\nabla^2 + \frac{f_0^2}{\sigma}\frac{\partial^2}{\partial p^2}\right)\omega_{\mathrm{qg}} \approx \frac{2}{\sigma}\left[f_0 \frac{\partial \mathbf{V_g}}{\partial p} \cdot \nabla \eta_g\right], \tag{2.10}$$

where $\sigma = -\frac{1}{\rho}\frac{\partial \ln \theta}{\partial p}$ is the stratification parameter and $\mathbf{V_g}$ the geostrophic wind (Sutcliffe, 1947, Trenberth, 1978). Since vorticity can be partitioned into shear and curvature components (e.g. Bell and Keyser, 1993), Eq. (2.10) can be re-written as

$$\left(\nabla^2 + \frac{f_0^2}{\sigma}\frac{\partial^2}{\partial p^2}\right)\omega_{\mathrm{qg}} \approx \frac{2}{\sigma}\left[f_0 \frac{\partial \mathbf{V_g}}{\partial p} \cdot \nabla (\zeta_s + \zeta_c + f)\right] \tag{2.11}$$

such that the three-dimensional second derivative of QG vertical motion is given by the linear combination of geostrophic shear, geostrophic curvature and planetary vorticity advection by the thermal wind ($\frac{\partial \mathbf{V_g}}{\partial p} = \left(\frac{-R}{fp}\right)\hat{k} \times \nabla T$, Martin, 2006a, their Eq. 4.27b). Since the thermal wind blows along isotherms/isentropes/thickness contours with cold air to its left (in the Northern Hemisphere), one can evaluate Eq. (2.10) and diagnose

the distribution of QG vertical motion using only maps of upper-level temperature and geostrophic vorticity.

Consider the jet-entrance region of a hypothetical upper-level jet streak like that pictured in Fig. 2.4a. In the poleward entrance region there is strong anticyclonic geostrophic vorticity advection by the thermal wind (AVA) associated with the downstream vorticity maximum. Oppositely signed geostrophic vorticity advection by the thermal wind is present in the equatorward entrance region (CVA), and there is a thermally direct circulation straddling the jet-entrance region. This ageostrophic circulation serves to maintain thermal wind balance despite the geostrophic wind's self-destructive tendency (i.e. simultaneous confluent frontogenesis and negative geostrophic momentum advection, Martin, 2006a, see their Ch. 6.4.1).

Developing upper-level waves are characterized by a phase-lag between upper-level height and thermal fields such that the environment upstream of the trough axis is prone to cold air advection (Rotunno et al., 1994). A hypothetical jet-entrance region characterized by geostrophic cold advection is provided in Fig. 2.4b. Evaluation of Eq. (2.10) indicates the thermally direct circulation associated with confluent frontogenesis is shifted such that descent (AVA) is maximized immediately along the jet core. A cross section through this region indicates that differential vertical motion will act to tilt a horizontal vortex tube associated with the vertical shear of the overlying jet into the vertical (Fig. 2.5). This occurs in the warm air where the relative vorticity is already anticyclonic (Fig. 2.4b

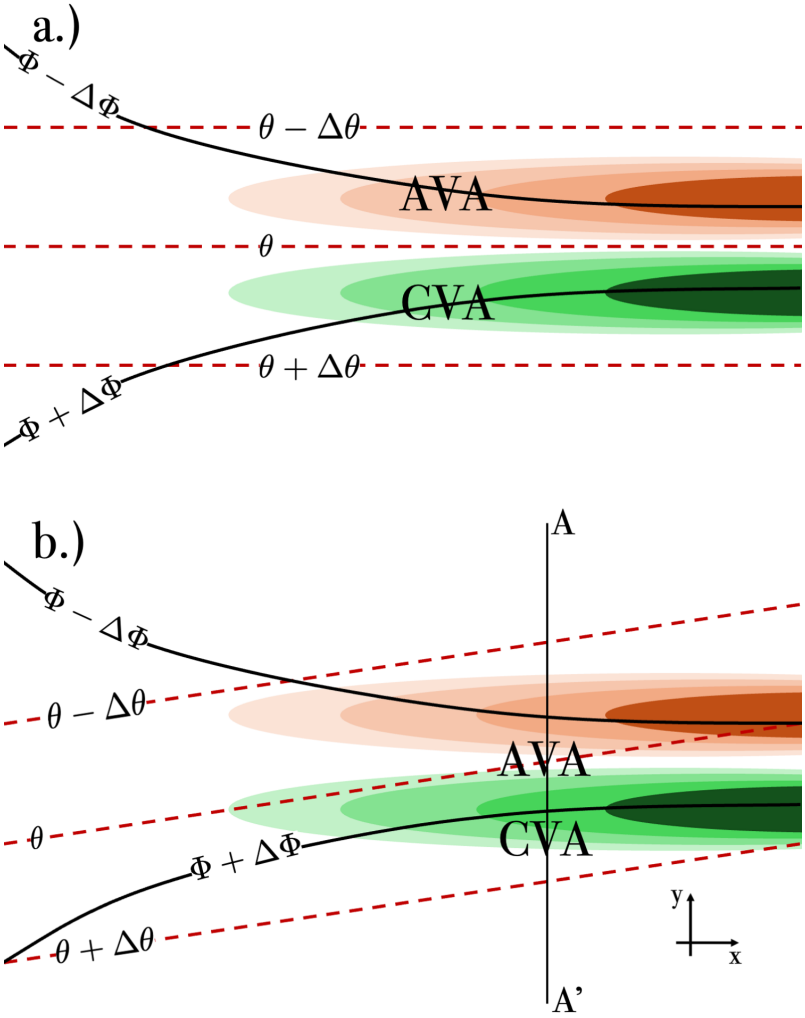

FIGURE 2.4: a.) Isohypses (solid black), isentropes (dashed red) and geostrophic cyclonic (red shaded) and anticyclonic (green shaded) shear vorticity) for a hypothetical jet-entrance region. AVA (CVA) indicates one location characterized by strong anticyclonic (cyclonic) geostrophic vorticity advection by the thermal wind. b.) As in a.) except for a jet characterized by cold air advection.

& 2.5). Since the thermal wind also represents the large-scale horizontal vorticity, these vortex tubes can be inferred from the distribution of temperature.

The frictionless, isobaric vorticity equation is given

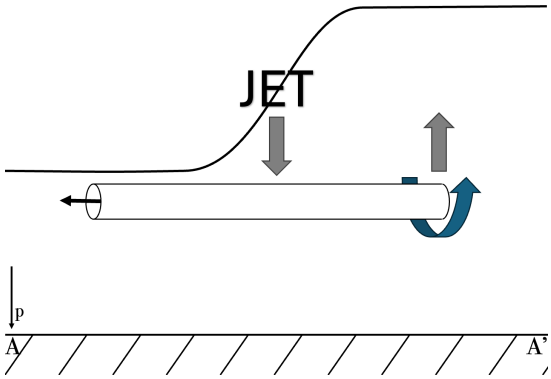

FIGURE 2.5: A hypothetical cross-section through the jet-entrance depicted in Fig. 2.4b. The jet core is identified (JET) along the steepest portion of the dynamic tropopause (solid black). The distribution of vertical motion is indicated by the grey vectors, and a horizontal vortex tube associated with the vertical shear of the jet is indicated by the white cylinder. This vortex tube is subject to tilting by the QG vertical motion.

$$\frac{\partial \eta}{\partial t} = -\mathbf{V} \cdot \nabla \eta + \omega \frac{\partial \zeta}{\partial p} - \eta(\nabla \cdot \mathbf{V}) + \hat{k} \cdot \left(\frac{\partial \mathbf{V}}{\partial p} \times \nabla \omega \right), \tag{2.12}$$

where $\eta = \zeta + f$ is the full absolute vorticity, ζ the full relative vorticity, and ω is the full vertical motion comprised of QG (ω_{qg}) and non-QG components (ω^*). The first two terms on the right-hand side (rhs) are horizontal and vertical vorticity advection, respectively. The third term is the tendency associated with convergence/divergence in the presence of absolute vorticity (i.e. stretching/squashing). The fourth term is the tendency associated with tilting of horizontal vortex tubes into the vertical (i.e. tilting). In the traditional QG vorticity equation the second and fourth terms on the rhs are discarded since ζ is assumed to be small relative to f. In this case, however, f and ζ are of comparable magnitude and each term on the rhs should be retained.

We can isolate sign changes in η following the horizontal flow by moving all horizontal advective terms to the left-hand side (lhs).

$$\frac{d_h \eta}{dt} = -\omega \frac{\partial \zeta}{\partial p} - \eta(\nabla \cdot \mathbf{V}) + \hat{k} \cdot \left(\frac{\partial \mathbf{V}}{\partial p} \times \nabla \omega \right), \tag{2.13}$$

where $\frac{d_h}{dt}$ is a horizontal flow-following total derivative. Consider the vorticity tendency for flow entering the anticyclonic flank of a westerly jet streak in middle latitudes. If $\eta \approx f$, the relative vorticity must drop by the magnitude of $f \approx 1 \times 10^{-4}$ s^{-1} before the absolute vorticity becomes anticyclonic. If this change occurs over about 3 hours, $\frac{d_h \eta}{dt}$ is approximately 1×10^{-8} s^{-2}. If this change occurs over about 1 day, the required tendency is on the order of 1×10^{-9} s^{-2}. This threshold is similarly reduced when the initial value of absolute vorticity is low, as is observed on the anticyclonic shear side of the mid-latitude jet streams.

Since we are concerned with situations wherein the absolute vorticity changes sign, consideration of the physical manifestation of these terms in the jet-trough entrance region leads to important insights. As $\eta \to 0$, so must the second (stretching) term on the rhs of Eq. (2.13). It follows that vortex squashing can lead to low values of η, but can not be directly responsible for producing anticyclonic values. Further, while the vertical advection term is expected to be non-negligible, ω can only transport existing vorticity from one isobaric surface to another. This means that vertical advection can only be responsible

for sign changes if absolute vorticity of the opposite sign already exists somewhere in the domain. This isolates tilting as the sole adiabatic process capable of turning the absolute vorticity anticyclonic.

Consider conditions in the equatorward entrance region of a jet streak characterized by cold air advection (as in Fig. 2.6c). Immediately beneath the jet core the geostrophic vertical shear/horizontal vorticity ($\frac{\partial \mathbf{V_g}}{\partial p}$) is approximately -1×10^{-3} m s^{-1} Pa^{-1} and the vertical motion changes by approximately 10 dPa s^{-1} between the jet core and the ambient environment. If this distance is 1000 km, the tilting term on the rhs of Eq. (2.13) scales like -1×10^{-9} s^{-2}, and is another order of magnitude larger if the change in vertical motion occurs over 100 km. While a similarly sized and signed tilting mechanism is expected in the poleward exit of a jet characterized by warm air advection (not shown), this action occurs where the absolute vorticity is strongly cyclonic. Similarly, while a jet not experiencing temperature advection can still have robust gradients in vertical motion (as given by QG forcing for ascent in Fig. 2.4a), these gradients are laterally displaced relative to existing critical points in relative vorticity. Thus, the equatorward jet entrance region is a special case where an anticyclonic tendency associated with tilting acts on flow that already has anticyclonic relative vorticity.

2.4 Methods

2.4.1 April 2013 case

Analysis was performed in a meteorological python environment (May et al., 2022) using 1.25° Japanese Reanalysis for Three Quarters of a Century (JRA3Q, Kosaka et al., 2024) data at 6-hr resolution and 45 isobaric levels (every 50 hPa in the mid- and upper troposphere). The presence of instability was confirmed in 0.25° analyses from the European Centre for Medium-Range Forecasting's v5 Reanalysis (ERA5, Hersbach et al., 2020). Composite visible satellite imagery from the Moderate Resolution Imaging Spectroradiometer (MODIS) was retrieved from the National Aeronautics and Space Administration's online Worldview tool. Geostrophic shear and curvature vorticity were calculated following Bell and Keyser (1993, see their Eq. A.3a-b). The quality of this partition was confirmed by comparing the sum of the latter and planetary vorticity with an independent calculation of the absolute geostrophic vorticity. In addition, the difference between τ_i and τ_{adv} was calculated using JRA3Q geostrophic absolute vorticity and full winds at 12Z on 8 Apr 2013. At that time, the length of the inertially unstable region [L in Eq. (2.9)] was approximately 1000 km (see Fig. 2.2b).

The rhs of Eq. (2.11) was expanded into three terms representing forcing for QG ascent consistent with shear, curvature and planetary geostrophic vorticity advection by the thermal wind. These terms were calculated using a horizontally discretized stratification parameter approximated using a two-point finite difference taken over 200 hPa layers (e.g.

300–500 hPa for the 400 hPa isobaric surface). This difference was chosen since it was the finest resolution at which the stratification parameter was positive everywhere in the middle and upper troposphere. The Coriolis parameter was held constant at 40°N. Since the Laplacian and its inverse are linear operators, the vertical motion associated with these processes can be solved individually using the successive over-relaxation technique. This inversion scheme was applied over a subset of JRA3Q data (20–60°N, 90–150°W) with zero vertical motion at the boundaries. This methodology is nearly identical to that used by Martin (2014) except they used a constant stratification parameter and the Q-vector form of Eq. (2.10) described by Martin (2006b). Allowing the stratification parameter to vary in space potentially allows for a more robust diagnosis of QG vertical motion in regions where the stability varies dramatically (e.g. near the dynamic tropopause).

We are specifically interested in large-scale processes associated with an anticyclonic vorticity tendency. In order to isolate these terms, we adapt Eq. (2.13) as

$$\frac{d_h \eta}{dt} = -\omega_{\mathrm{qg}} \frac{\partial \zeta}{\partial p} - \eta \frac{\partial \omega_{\mathrm{qg}}}{\partial p} + \hat{k} \cdot \left(\frac{\partial \mathbf{V_g}}{\partial p} \times \nabla \omega_{\mathrm{qg}} \right) + \mathrm{RES}, \tag{2.14}$$

where RES contains vertical advection, tilting and stretching processes associated with non-QG vertical motion. Calculating the tilting term using the Sutcliffe-Trenberth species of ω_{qg} specifically neglects the role of small-scale turbulence, deformation and diabatic processes. Though slightly weaker in magnitude (i.e. $\approx 1 \times 10^{-9}$ s^{-2}), the distribution

of tilting by ω_{qg} was very similar when the geostrophic shear was substituted for the full shear (see Fig. B.1b & e). This indicates that the horizontal vorticity can be diagnosed with reasonable fidelity using only the distribution of temperature. We also offer a brief analysis of the first three terms on the rhs of Eq. (2.14) to demonstrate that QG dynamics qualitatively capture the expected vorticity tendencies in the broader trough environment. The full vorticity budget is not provided for the April 2013 case due to distinct closure issues in modern reanalysis products (Morris et al., 2025). This further emphasizes the utility of the QG perspective since 1) ω_{qg} is already known to be responsible for upper-level jet development in these specific cases (Martin, 2014) and 2) the jet development, let alone the appearance of anticyclonic geostrophic absolute vorticity, goes unexplained when JRA3Q (or ERA5) model ω is employed (see Fig. B.1c & f).

2.4.2 Idealized case

In order to bolster confidence in results from the April 2013 case study, a similar analysis was performed on the development of anticyclonic absolute vorticity on the equatorward side of a jet streak in an idealized simulation of a baroclinic wave. This simulation was performed within the University of Wisconsin Non-hydrostatic Modeling System (UW-NMS, Tripoli, 1992) and is identical to that described in Martin (2014, see their Section 2.2). The initial output (126×100 km at 40 vertical levels extending to 20.5 km) was interpolated to a 1° grid at 19 isobaric levels. Terms in Eq. (2.14) were calculated as described in the preceding subsection to produce distributions of vorticity tendency associated with the QG vertical motion.

The relative contribution of tilting on the rhs of Eq. (2.14) towards the horizontal flow-following vorticity tendency (LHS) is given by

$$\mathrm{Proj_t} = \left| \frac{d_h \eta}{dt} \times \left(\frac{\partial u_g}{\partial p} \frac{\partial \omega_{\mathrm{qg}}}{\partial y} - \frac{\partial v_g}{\partial p} \frac{\partial \omega_{\mathrm{qg}}}{\partial x} \right) \right| / \left(\frac{d_h \eta}{dt} \right)^2, \tag{2.15}$$

where a contribution of 1 (0) indicates that all (none) of the horizontal flow-following vorticity tendency can be explained by QG tilting. Other values indicate the presence of budget residuals and/or the influence of competing processes on the rhs of Eq. (2.14). Since we are primarily concerned with regions where processes are strong, $\mathrm{Proj_t}$ was only calculated where the magnitude of vorticity tendency associated with QG tilting exceeded $|0.5 \times 10^{-9}|$ s^{-2}. This is a simple application of a technique employed in the evaluation of moist static energy (Andersen and Kuang, 2012, Arnold et al., 2015, Mayta and Adames, 2023), precipitation (Adames, 2017) and moist potential vorticity (Adames et al., 2022) budgets. Rather than average conditions throughout an area or period, Eq. (2.15) is evaluated for all points in the 350–450 hPa isobaric layer at forecast hours 42, 48 and 54, the period over which anticyclonic geostrophic absolute vorticity arises in the UW-NMS simulation. Noise is subsequently reduced using a 9-point horizontal smoother. Conclusions drawn from this analysis did not change substantially when smoothing was not applied. A layer-average perspective was taken in order to demonstrate that this is a moderately deep phenomenon occurring in the vertically-sheared region beneath the

equatorward-entrance region.

This idealized case is included partially due to issues with vorticity budget closure in popular reanalysis products (as discussed in the preceding subsection, e.g. Morris et al., 2025). While budget residuals associated with computational errors, sub-grid, and non-QG processes persist in both analyses, residuals associated with analysis increments are thought to be slightly lesser in the UW-NMS output since it is unconstrained by observations. That said, complete budget closure should not be expected in either case since the QG vertical motion employed in Eq. (2.14) explicitly neglects deformation, diabatic heating and other sub-grid processes. Vorticity budgets needn't close, however, for physical inferences to be made (e.g. Martin, 2014). This is especially true when a portion of the budget tendency can be attributed to a distinct physical process. Ideally, budget residuals are second order tendencies, though this is rarely feasible when using finite-differencing schemes on data at coarse spatial and temporal resolutions. That said, since the vorticity tendency associated with QG tilting is calculated at each grid point, evaluation of Eq. (2.15) explicitly evaluates the local explanatory power of the proposed tilting mechanism. This allows for relatively robust physical attribution even when the relative size of budget residuals vary in the domain.

2.5 Analysis

2.5.1 April 2013 case

At 00Z on 8 April 2013, an upper-level jet was embedded within strong northwesterly flow just offshore the west coast of the United States (Fig. 2.2a). Both the entrance and exit regions were characterized by strong temperature advection at 400 hPa. Over subsequent analysis periods, a semi-continuous region of weak inertial instability developed in a strip stretching from the waters offshore Point Conception, CA (35°N, 122.5°W) to Northern Baja near Mexicali, MX (32.4°N, 115.5°W). At 12Z on 8 April, this feature had elongated to approximately 1000 km in length while maintaining the narrow, sub-synoptic width characteristic of upper-level jet/front features (Fig. 2.2b). 24 hours later, the feature had elongated to approximately 1500 km (Fig. 2.2d). The upper-level trough 'cut-off' (a closed isohypse near the geopotential height minimum) and remained quasi-stationary for nearly 36 hours (Fig. 2.2d-g). The anticyclonic geostrophic absolute vorticity minimum maintained synoptic (sub-synoptic) length (width) characteristics throughout this period, however, by 00Z on 11 April the feature lost continuity and, 12 hours later, vanished (Fig. 2.2g-h).

The geostrophic vorticity at 12Z on 8 April 2013 was partitioned into shear and curvature components (Fig. 2.6a & b, respectively). This is the first 12-hr analysis period where anticyclonic geostrophic absolute vorticity appeared in the JRA3Q (Fig. 2.2b). At 400 hPa the geostrophic wind increases with height consistent with thermal wind balance. This

shear is associated with horizontal vortex tubes (black arrows) which point towards cold air, orthogonal to isentropes (Fig. 2.6a-c). Since the jet-entrance region is characterized by strong cold air advection (Fig. 2.2c), advection of shear vorticity by the thermal wind contributes substantially to QG descent in an oblong distribution maximizing within the jet core (Fig. 2.6a). The horizontal gradient in vertical motion on the equatorward side of the jet entrance acts to tilt horizontal vorticity into the vertical (blues, Fig. 2.6d). This process is most robust along the 732–714 dam isohypses. A more isotropic region of QG ascent in the jet exit region acts to tilt horizontal vorticity into the vertical, thereby quickly re-establishing inertial stability of parcels exiting the jet (Fig. 2.6a & d).

A similar distribution of QG vertical motion associated with geostrophic curvature vorticity advection also produces couplets of oppositely signed vortex tilting in the jet entrance and exit regions (Fig. 2.6b). Though slightly weaker, these vortex tilting couplets are of similar magnitude to those associated with shear vorticity advection, act in the same direction and maximize along the same bundle of isohypses (732–714 dam). This indicates the importance of considering tilting by the full QG vertical motion, as provided in Fig. 2.6c & f.

While the anticyclonic tendency associated with tilting in the equatorward entrance is comparatively weak relative to other jet-quadrants (Fig. 2.6f), a parcel flowing along the 726 dam isohypse in Fig. 2.6f and Fig. 2.7a experiences an anticyclonic vorticity tendency of order $1\text{–}4 \times 10^{-9}$ s^{-2} for approximately $\tau_{\text{adv}} \approx 6$ hrs. The relative vorticity of parcels approaching the anticyclonic side of the jet core could be expected to drop by

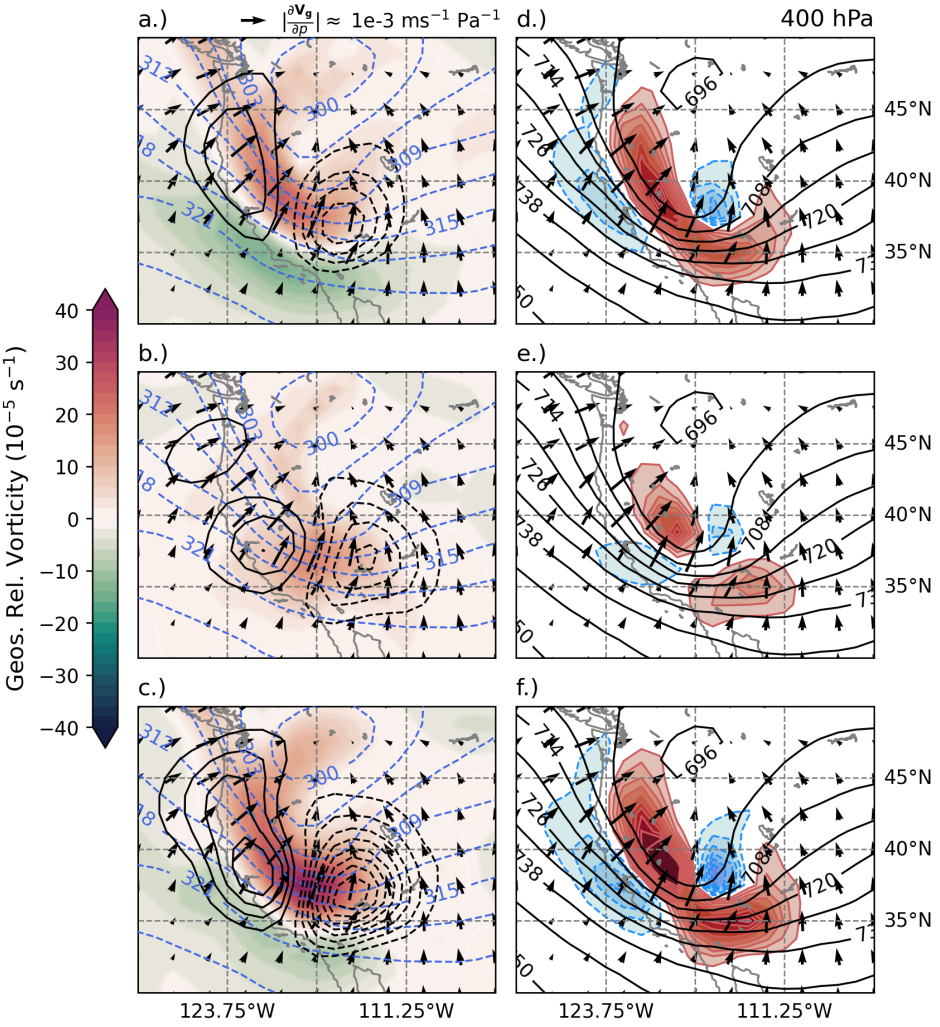

FIGURE 2.6: a.) 400 hPa isentropes (dashed blue every 3 K), geostrophic shear vorticity (shaded), horizontal vortex tubes arising from the geostrophic vertical shear (black arrows) and QG vertical motion consistent with shear vorticity advection by the thermal wind (black contours every 2 dPa s^{-1} from 2 and -2 dPa s^{-1}) at 12Z on 8 April 2013. b.) as in a.) except with geostrophic curvature vorticity and the vertical motion arising from its advection by the thermal wind. c.) as in a.) except for the geostrophic relative vorticity and vertical motion arising from its advection by the thermal wind. d.) 400 hPa isohypses (solid black every 6 dam), horizontal vortex tubes arising from the geostrophic vertical shear (black arrows), and the vorticity tendency (shaded blues and reds every 1 $\times 10^{-9}$ s^{-2} from -1 and 1 $\times 10^{-9}$ s^{-2}, respectively) associated with tilting of the geostrophic vertical shear by the QG vertical motion in a.). e.) as in d.) except for the vorticity tendency associated with tilting by the QG vertical motion in b.). f.) as in d.) except for the vorticity tendency associated with tilting by the QG vertical motion in c.).

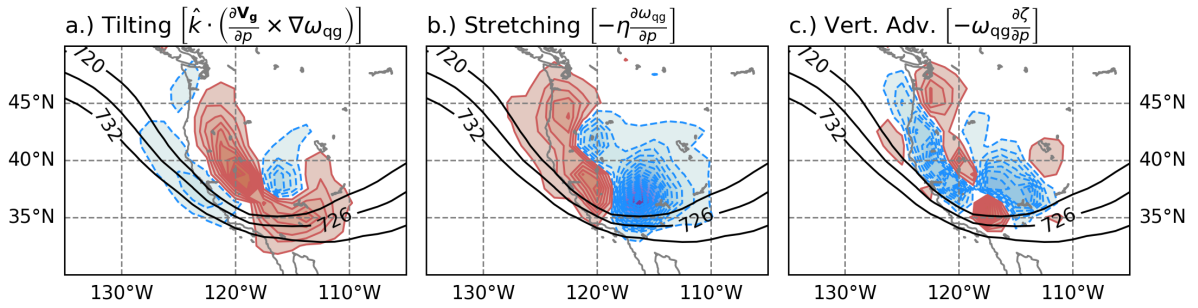

FIGURE 2.7: a.) 400 hPa geopotential heights (solid black at 732, 726 and 720 dam) and the vorticity tendency associated with tilting (shaded blues and reds every 2×10^{-9} s^{-2} from -1 and 1×10^{-9} s^{-2}, respectively) at 12Z on 8 April 2013. b.) as in a.) except for the tendency arising from stretching. c.) as in a.) except for the tendency arising from vertical advection.

over 2×10^{-5} s^{-1} in that time. While stretching (Fig. 2.7b) and vertical advection (Fig. 2.7c) are both important processes, neither contribute strongly to anticyclonic vorticity tendencies along the 732–720 dam isohypses. Since the anticyclonic vorticity tendency maximizes in a region already characterized by relative vorticity between -6×10^{-5} s^{-1} and -8×10^{-5} s^{-1} (see Fig. 2.6c), we determine that tilting processes are responsible for the anticyclonic geostrophic absolute vorticity feature.

An inertially unstable region associated with a vigorous jet streak can be persistent due to the difference between parcel residence time and that required for unstable perturbations to develop (see Chapter 2.2). Parcel residence times (τ_{adv}) and perturbation e-folding times (τ_i) were calculated in the JRA3Q data using the full wind speed and a feature length scale of 1000 km, similar to that observed in Fig. 2.2b. The difference between τ_i and τ_{adv} was plotted against geostrophic absolute vorticity for each grid point on the 400 hPa isobaric surface in a domain surrounding the anticyclonic geostrophic absolute

vorticity feature at 12Z on 8 Apr 2013 (Fig. 2.8a). The vast majority of points characterized by inertial instability featured parcel residence times shorter or approximately equal to the time required for unstable perturbations to develop. This indicates that unstable parcels leave the jet before perturbations grow by an order of e. In this case, feature persistence is a function of both an ongoing production mechanism and the inability for unstable perturbations to sufficiently mix momentum.

2.5.2 Idealized case

An idealized simulation of a developing baroclinic wave was performed in the UW-NMS model. Between forecast hour 18 (F18) and F60 the amplitude of an upper-level wave within both height and thermal fields increased, eventually resulting in a cut-off trough aloft (Fig. 2.9a-h). Tightly packed isohypses on the equatorward side of this cut-off feature were associated with a strong jet streak, its horizontal shear so intense that the geostrophic absolute vorticity became anticyclonic on its equatorward side despite the presence of cyclonic curvature (Fig. 2.9f-h).

Prescribed in this idealized development is an approximately quarter-wavelength lag between sinusoidal patterns in upper-level height and thermal fields. This guarantees prolonged cold air advection in the northwesterly flow upstream of the trough axis, an arrangement of isohypses and isentropes resulting in anticyclonic geostrophic vorticity advection by the thermal wind which maximizes within the jet core (Fig. 2.9e & Fig. 2.10a). Strong gradients in vertical motion flanking jet entrance and exit regions act to tilt horizontal vortex tubes associated with the vertical shear into the vertical (Fig.

2.10a-c). The resulting vorticity tendencies are on the order of 1×10^{-9} s^{-2} and persist over several analysis periods (Fig. 2.10e-f). As in the April 2013 case, the anticyclonic tendency associated with QG tilting occurs in a region where the geostrophic relative vorticity was already anticyclonic (approximately -5×10^{-5} s^{-1}, see Fig. 2.10a).

Tilting of horizontal vortex tubes by the QG vertical motion explains over two thirds of the horizontal flow-following vorticity tendency in a narrow strip on the equatorward fringe of the jet-entrance region (see black dots in Fig. 2.10d-f). This strip of high relative contribution [$\text{Proj}_\text{t} > 0.66$, see Eq. (2.15)] lies immediately upstream the region of anticyclonic geostrophic absolute vorticity and acts on the same bundle of isohypses (732–714 dam) over several analysis periods. A like-signed vorticity tendency is apparent in the poleward exit region, though this occurs in a region characterized by strongly cyclonic geostrophic relative vorticity. This further supports the conclusion that the equatorward entrance region of jet streaks characterized by cold advection are uniquely favorable towards the production of anticyclonic geostrophic absolute vorticity. Though the tendency associated with tilting is relatively weak (i.e. -1×10^{-9} s^{-2}), it arises slowly from the evolution of the large-scale flow and acts on a narrow region already characterized by anticyclonic relative vorticity.

The strong winds and short length scale associated with this inertially unstable region indicates that parcel residence times (τ_adv) may be small relative to the time required for unstable perturbations associated with the release of inertial instability to grow by an order of e (τ_i). The difference between τ_i and τ_adv is plotted against geostrophic

absolute vorticity in a region surrounding the inertially unstable region at F54 (Fig. 2.8b, using 25–40°N and 75–105°W). The e-folding timescale for unstable perturbations is always greater than parcel residence time when the absolute geostrophic vorticity is anticyclonic. As in the April 2013 case, feature persistence is related to both an ongoing production mechanism and the inability for perturbations to sufficiently mix momentum before parcels leave the unstable region.

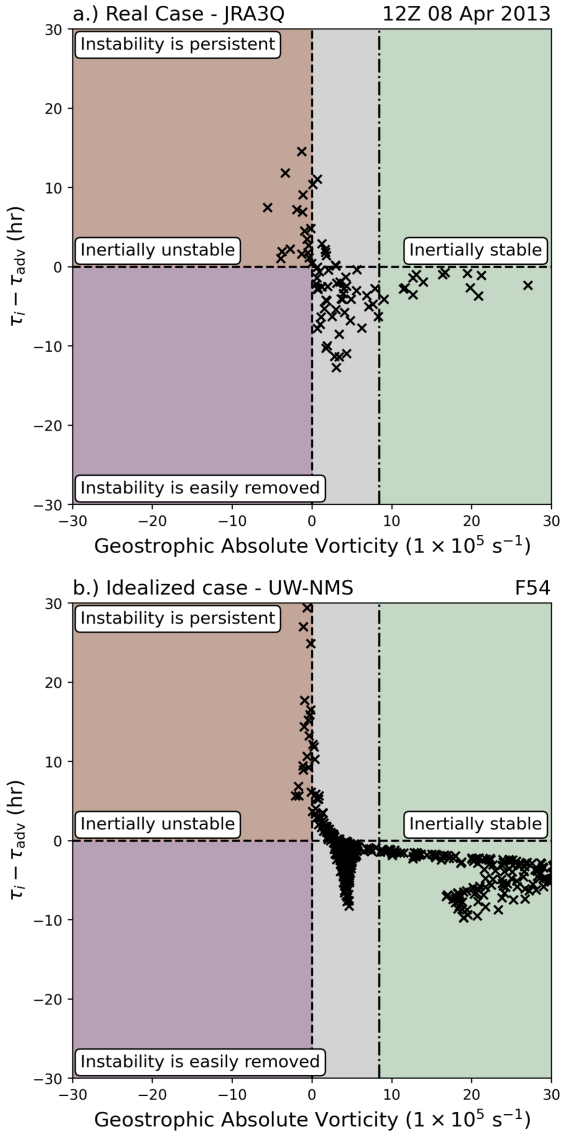

FIGURE 2.8: a.) The difference between τ_i and τ_{adv} plotted against η_g for a region surrounding the anticyclonic η_g feature (30–40°N, 110–130°W) at 12Z on 8 April 2013 (see Fig. 2.2b) using JRA3Q data at 400 hPa. The green region at high η_g is strongly inertially stable. The grey region bounded by $\eta_g = 0$ (vertical dashed black) and f (vertical dash-dotted black) is weakly inertially stable. The red region at anticyclonic η_g and positive $\tau_i - \tau_{\text{adv}}$ is a persistent inertially unstable regime. The violet region at anticyclonic η_g and negative $\tau_i - \tau_{\text{adv}}$ is the regime wherein unstable perturbations are expected to quickly remove instability. b.) as in a.) except for the region surrounding the anticyclonic η_g feature (25–35°N, 75–95°W) at F54 (see Fig. 2.9g) in the idealized UW-NMS simulation at 400 hPa.

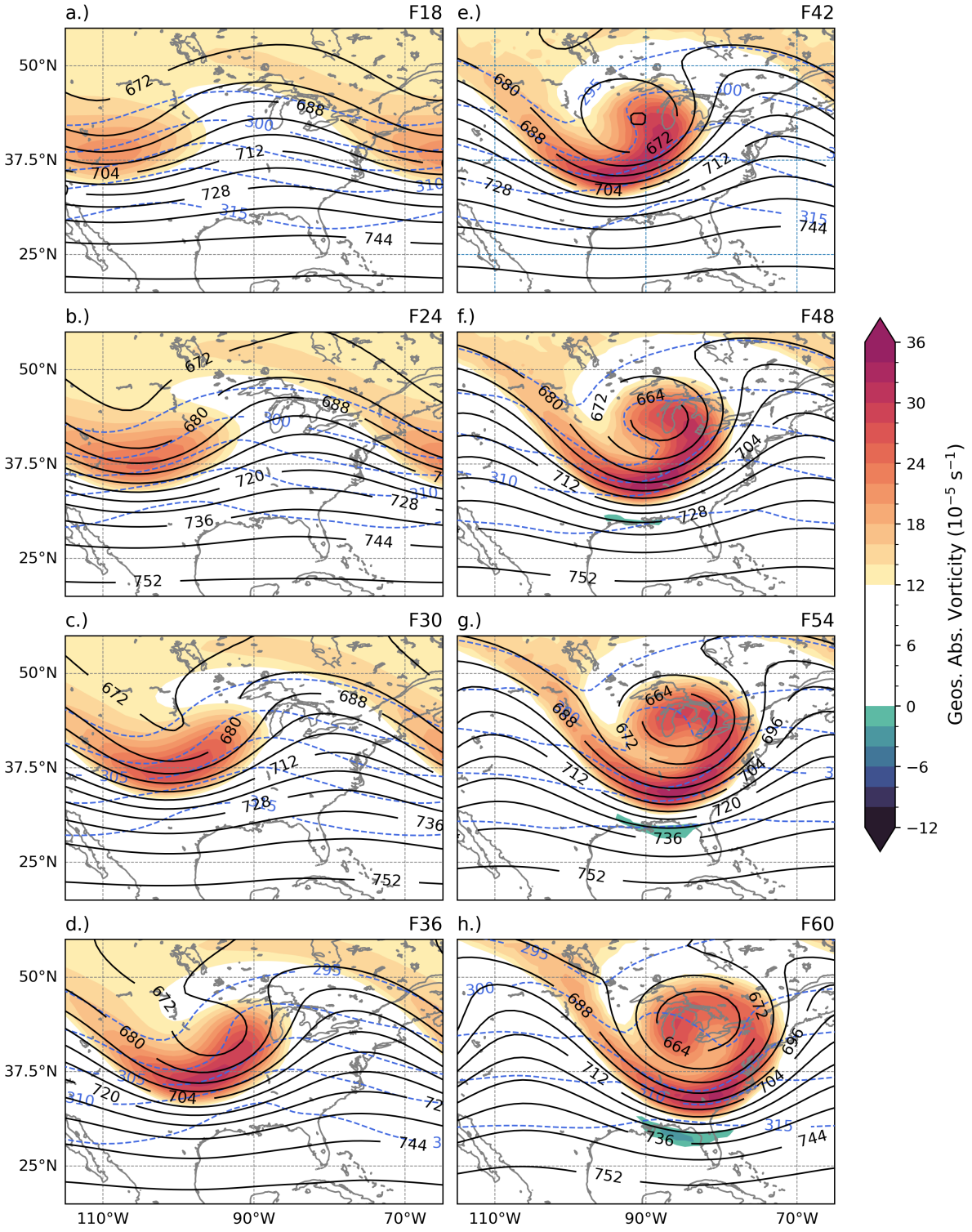

FIGURE 2.9: a.) As in Fig. 2.2 except with geopotential height (solid black every 8 dam) and potential temperature (dashed blue every 5 K) for forecast hour 18 (F18) at 400 hPa in the idealized UW-NMS simulation. b-h.) as in a.) except for F24–F60 at 6 hr intervals.

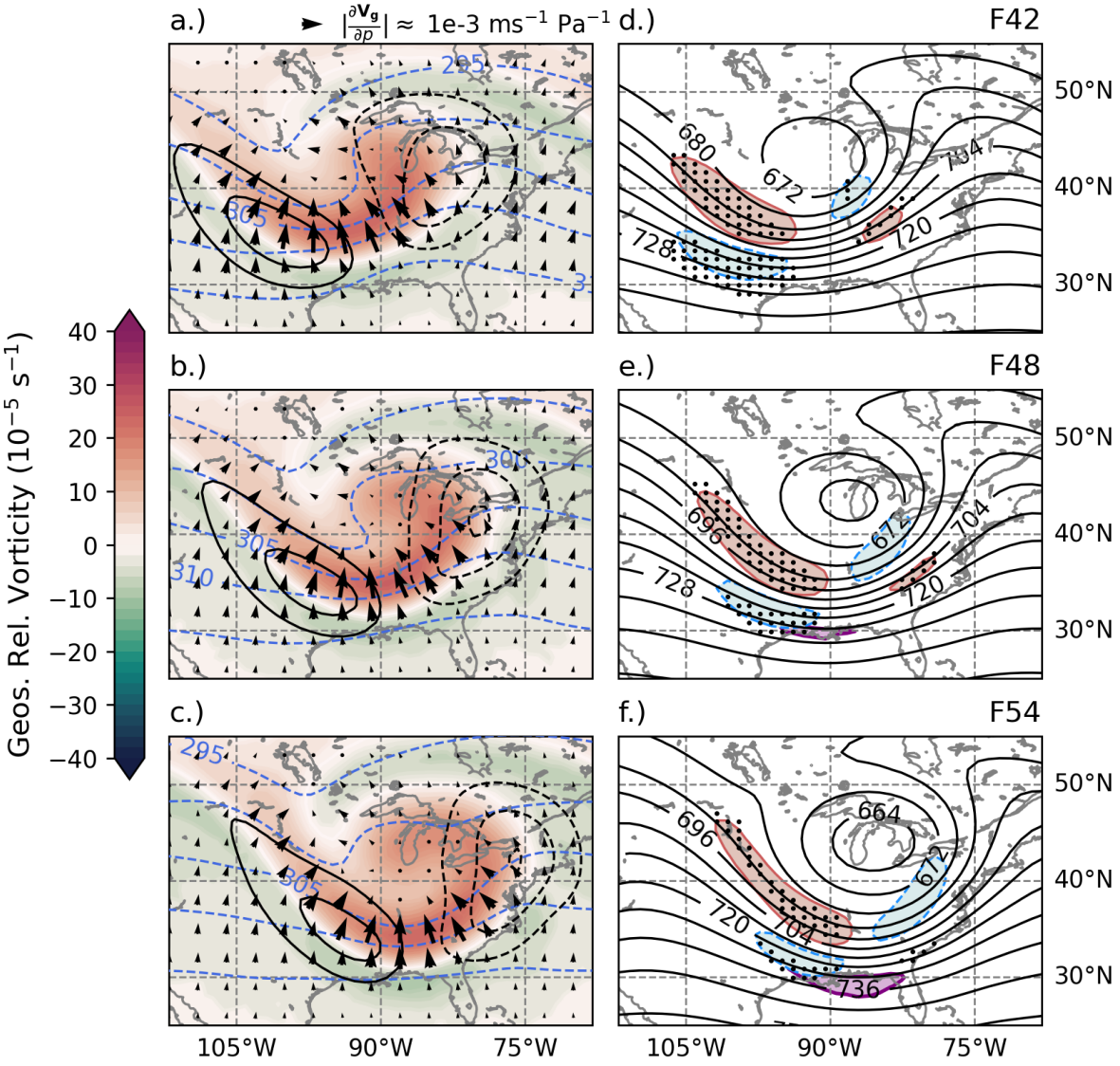

FIGURE 2.10: a.) As in Fig. 2.6c except averaged over the 450–350 hPa layer at F42, the 6-hr forecast period immediately before anticyclonic geostrophic absolute vorticity arises in the idealized UW-NMS simulation (see Fig. 2.9f). b-c.) as in a.) except for F48 and F54, respectively. d.) as in Fig. 2.6f except averaged over the 450–350 hPa layer at F42. Grid points wherein $\text{Proj}_t > 0.66$ [see Eq. (2.15)] are stippled (black dots) only where the vorticity tendency associated with tilting processes is $> |0.25 \times 10^{-9}|$ s^{-2}. e-f.) as in d.) except for F48 and F54, respectively.

2.6 Discussion

2.6.1 Conclusions

Recent climatological investigations of anticyclonic geostrophic absolute vorticity reveal that, though relatively rare, inertial instability can occur along the equatorward side of the mid-latitude jet streams. These regions have been linked to clear-air turbulence arising from perturbations inherent to the release of instability. These gravity wave-like perturbations mix momentum laterally along isentropes until the local geostrophic absolute vorticity collapses to zero. It was because of this mechanism, and the limitations of mid-20th century observations, that led early synopticians to view regions of inertial instability as necessarily short-lived, if they existed at all on larger scales. It is our perspective, however, that under certain conditions these features can persist despite the release of inertial instability.

Several investigations have now linked anticyclonic absolute vorticity features near the mid-latitude jets to diabatic heating in sub-synoptic scale features like tropical cyclones (Prince and Evans, 2022), or the warm conveyor belts embedded within mid-latitude cyclones (Harvey et al., 2020, Oertel et al., 2020). Case study analysis, however, indicates that pervasive anticyclonic geostrophic absolute vorticity features can arise in synoptic environments characterized by strong QG descent and clear skies. The primary example of this arises during the development of strong upper-level jet streaks in northwesterly flow immediately upstream of a large-scale trough. This is a region predisposed to geostrophic

cold air advection such that anticyclonic geostrophic vorticity advection by the thermal wind (consistent with QG descent) maximizes along the jet core. This shifts the distribution of vortex tilting such that a strong anticyclonic vorticity tendency acts on parcels in the equatorward entrance region.

Since the thermal wind blows along isotherms with cold air to its left (in the Northern Hemisphere), one can diagnose this phenomenon using only standardized maps of upper-level isotherms, isohypses and geostrophic vorticity. This analysis was performed in both real and idealized cases of upper-level jet development and is best summarized in Fig. 2.11 using analyses similar to that in Fig. 2.6c. Consider a parcel flowing along the anticyclonic side of the upper-level jet (Fig. 2.11, isohypses in bottom panel). This parcel will experience a negative vorticity tendency associated with tilting (blue dashed contours, bottom panel), diagnosed from the distribution of vertical motion (solid black contours, top panel) and its action on horizontal vorticity (black arrows, middle panel). This ultimately results in a downstream region of anticyclonic geostrophic absolute vorticity (purple, middle panel). Since the large-scale horizontal vorticity (i.e. the geostrophic shear/thermal wind) can be inferred by the distribution of temperature, the middle panel is unnecessary in an operational setting. It is thought that the ingredients for anticyclonic geostrophic absolute vorticity production frequently exist on the equatorward side of upper-level jet streaks due to the observed lag between height and thermal fields in developing planetary waves; one should expect cold air advection upstream the trough axis. Whether or not the absolute geostrophic vorticity on their equatorward side actually

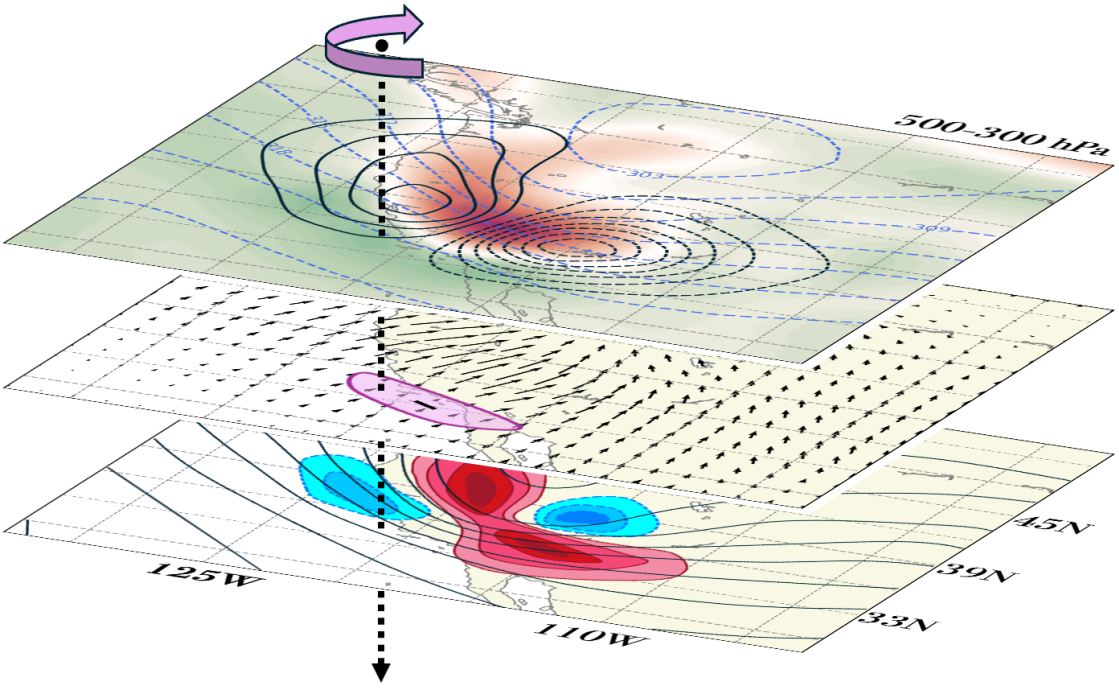

FIGURE 2.11: A three-dimensional depiction of the mechanism leading to anticyclonic absolute vorticity on the equatorward side of an intense jet-trough couplet over the western Continental United States at 12Z on 8 April 2013. The dashed black and heavy purple arrows indicate the orientation and spin, respectively, of a hypothetical anticyclonic vortex tube. All quantities were averaged over the 300–500 hPa layer and smoothed manually. Top: geostrophic relative vorticity (shaded greens/reds every 1 $\times 10^{-5}$ s^{-1}), isentropes (dashed red every 3 K) and ω_{qg} (black contours every 2 dPa s^{-1} from -2 and 2 dPa s^{-1}). Middle: horizontal vorticity associated with the vertical shear of the geostrophic wind (black vectors), and the approximate location of inertial instability (purple shaded). Bottom: tilting of horizontal vorticity by the differential QG vertical motion (shaded blues and reds every 1×10^{-8} s^{-2} from -1 and 1 $\times 10^{-8}$ s^{-2}, respectively).

becomes anticyclonic is a function of the initial geostrophic vorticity and the intensity of tilting processes.

Feature persistence is addressed via linear hydrodynamic instability theory. It is shown

that the e-folding time for the growth of perturbations associated with the release of inertial instability is greater than that required for a parcel to travel through the region of instability itself. This is contextualized in Fig. 2.3 using simple scaling arguments. For example, at 40°N a parcel traveling at 50 m s^{-1} will pass through a 1000 km jet streak before unstable perturbations grow by an order of e. This inequality ($\tau_i > \tau_{\text{adv}}$) was observed for the vast majority of grid points characterized by inertial instability in both real and idealized cases (Fig. 2.8, the "instability is persistent" regime). This inequality will diminish and eventually reverse with decreasing wind speeds, increasing length scales, or when feature celerity increases relative to the flow speed (Fig. 2.8, the "instability is easily removed" regime). Contrary to prior perspectives, it is concluded that inertially unstable regions of limited spatial scales (approximately 100 km × 1000 km) can persist in middle latitudes for several days, especially in the presence of an ongoing production mechanism.

2.6.2 Limitations, implications and future work

These findings have important implications for the forecasting of clear-air turbulence in the upper troposphere. Although we have indicated that unstable perturbations are unlikely to remove the instability before parcels leave the jet region, the continued release of such perturbations poses an ongoing risk to aviation. This risk is prolonged when unstable regions are persistent. Exploration of non-linear inertial instability theory, and the high-resolution modeling of the resulting disturbances is warranted. While the use of linear theory is a distinct limitation of the present study (non-linear e-folding times may

be substantially shorter), we posit that the persistence theory outlined in Chapter 2.2 succinctly describes why anticyclonic geostrophic absolute vorticity sometimes persists on synoptic length and timescales.

Another limitation is the use of relatively low resolution reanalysis data in the calculation of vertical motion and its dependencies. Anecdotally, the magnitude of ω_{qg} and its gradient does not necessarily increase with decreasing horizontal resolution. For example, the magnitude of tilting on the rhs of Eq. (2.14) was still on the order of 1×10^{-9} s^{-2} when using ω_{qg} inverted from 0.25° ERA5 analyses. When JRA3Q model vertical motion was used, the distribution of tilting processes was similar in the jet-entrance region, though magnitudes of vorticity tendency associated with tilting were weaker by about 1–2×10^{-9} s^{-2}. When ERA5 model vertical motion was used, the distribution of tilting processes (though sometimes on the order of 1×10^{-8} s^{-2}) lacked coherent structure unless a substantial amount of smoothing was applied. This alludes to the difficulty of performing robust momentum budget analysis using reanalysis datasets. We rely on the QG vertical motion since it is already known to be the principal portion of vertical motion associated with upper-level jet development in these specific cases (Martin, 2014). Further, QG descent is fairly representative of the total adiabatic descent (as calculated from the thermodynamic equation) in the idealized simulation (Fig. B.2).

We have elected to use a traditional definition of inertial instability which, by assuming a geostrophic equilibrium state, is diagnosed using the geostrophic absolute vorticity. This is primarily due to our interest in diagnosing instability in jet streak features which, when

straight, are well described by geostrophy. An instability criterion which incorporates centrifugal forces arising from curvature may also be employed (by using the full absolute vorticity, e.g. Knox, 1997). Regardless of criterion choice, anticyclonic absolute vorticity values are observed immediately after robust QG tilting processes were diagnosed on 8 April 2013 (Fig. B.3). From the perspective of aviation operations, caution is warranted regardless of whether both criteria agree. Future work will consider the role of curvature in potentially stabilizing (destabilizing) flow in the trough (ridge) region.

It is curious to consider what becomes of the resultant anticyclonic geostrophic absolute vorticity after it is produced. We propose that the region can be removed via oppositely signed tilting processes, diabatic processes (Oertel et al., 2020), and its inherent unstable perturbations. It is possible that the inertially unstable region can become a focal point for mesoscale convective system outflow (Blanchard et al., 1998). This would be an interesting, cross-scale phenomenon wherein tilting associated with large-scale subsidence produces an initial anticyclonic disturbance which is potentially maintained by diabatic processes excited by its presence.

Chapter 3

A moist potential vorticity perspective on the origin of inertial instability in the upper troposphere during the extra-tropical transition of tropical cyclones

3.1 Introduction

Inertial instability is a hydrodynamic instability arising from an imbalance between local pressure gradient and Coriolis forces (van Mieghem, 1951). This instability is said to be

present when the product of the absolute vorticity (ζ_a) and the local Coriolis parameter (f) is negative,

$$\zeta_a f < 0, \tag{3.1}$$

where ζ_a is the sum of relative (ζ) and planetary (f) vorticity. This criterion is sometimes met on the equatorward side of jet streaks embedded within upper-level jet streams (Ciesielski et al., 1989, Holton and Hakim, 2013, Beckley and Corraliza, 2026). Inertially unstable jets have been shown to emit wave-like perturbations which mix momentum laterally until gradient wind balance is achieved (Stone, 1966, 1972, Holton and Hakim, 2013, Thompson and Schultz, 2021). This behavior limits the strength of anticyclones in the large-scale environment, and can be associated with clear-air turbulence potentially hazardous to aircraft (Knox, 1997, Thompson and Schultz, 2021).

Because it was assumed that the release of instability would quickly re-instate gradient balance, it has been disputed whether inertial instability really occurred on synoptic spatial or temporal scales (e.g., Mogil and Holle, 1972, Holton, 1979, Ciesielski et al., 1989). Recent climatological analyses, however, indicate it is actually fairly common, even along the mid-latitude jets (e.g., Schultz and Schumacher, 1999, Sato and Dunkerton, 2002, Knox and Harvey, 2005, Thompson et al., 2018, Lojko et al., 2024).

Since the upper troposphere is almost always statically stable (i.e. potential temperature increases with height), an alternative approach to Eq. (3.1) is to consider the sign of the oft-dominant vertical component of potential vorticity (PV)

$$P \approx \rho^{-1} \zeta_a \frac{\partial \theta}{\partial z} \tag{3.2}$$

where ρ is the density and θ is the potential temperature. An isentropic PV perspective affords further insights due to the conservation of PV for frictionless, adiabatic flow (Hoskins et al., 1985). Since the time-mean PV in the upper-troposphere is signed like f, regions of negative PV (NPV) in the Northern Hemisphere represent substantial departures from climatology. An airmass with these characteristics must have either been transported from the Southern Hemisphere, or been modified in-situ by diabatic processes. While the former has been shown to occur during periods of cross-equatorial flow (Dunkerton, 1981, Thompson et al., 2018), the relatively rapid release of inertial instability indicates that local diabatic heating is the likely progenitor of NPV outside the tropics (e.g. Harvey et al., 2020).

A recent climatology from Lojko et al. (2024) demonstrates that upper-level NPV events *and* NPV-jet interaction events are common in the Northwest Atlantic relative to other regions at similar latitudes (see their Fig. 3 & 4). This feature is also observed in 1.25° Japanese Reanalysis for Three-Quarters of a Century (JRA3Q, Kosaka et al., 2024,

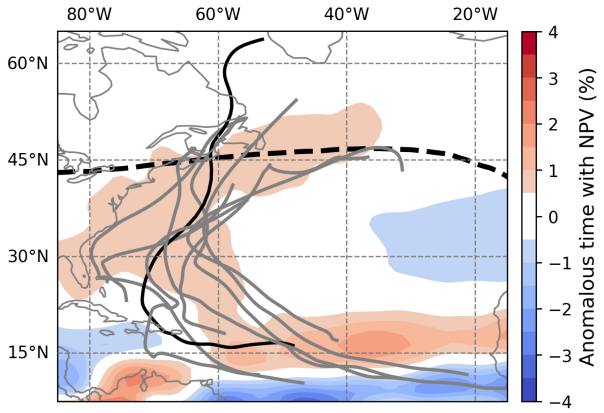

FIGURE 3.1: The climatological location of the September unimodal jet (3.1 PVU isertel over the 330–350 K isentropic layer, heavy dashed black), anomalous time with NPV relative to the expectation at that latitude for the 330–350 K isentropic layer average (red/blue shaded), and the paths of nine September hurricanes which transitioned into extra-tropical cyclones from 2018–2023 (heavy grey; heavy black for Hurricane Fiona).

see our Fig. 3.1). During the month of September, for example, there is a strip of anomalously high NPV expectation extending from East Africa, across the subtropical Atlantic, and northwestward into the North Atlantic (Fig. 3.1). The local maximum in NPV occurrence in mid-latitudes is generally located equatorward of the September mid-latitude jet (dashed line, Fig. 3.1), as defined by the mean location of the 3.1 PVU isertel in the 330–350 K isentropic layer (Orr, 2024). This suggests that some NPV events are embedded in the sheared jet stream environment while others occur firmly in tropical air. Considering the well-known presence of inertially unstable outflow in tropical cyclones (Black and Anthes, 1971), and their preference for extra-tropical transition (ET) in the Northwest Atlantic (e.g. grey lines, Fig. 3.1), it is hypothesized that ETs are responsible for a portion of NPV events in this region.

For example, nine robust ETs were observed in the western North Atlantic during the month of September from 2018 to 2023: Hurricane Dorian, Humberto, Paulette, Teddy,

Larry, Earl, Fiona, Franklin and Lee (Fig. 3.1). Upper-level PV analyses reveal that each ET was associated with a plume of NPV air lying radially outward from the cyclone (Fig. 3.2), and similar structures were observed by Prince and Evans (2022) during the ET of Hurricane Irma in September 2017. Harvey et al. (2020) and Oertel et al. (2020) also demonstrate that near-synoptic scale strips of NPV are observed in the warm conveyor belt of strong mid-latitude cyclones. Their existence is attributed to sub-synoptic diabatic heating in the presence of strong baroclinicity, however, diagnosis of the associated PV tendency requires calculations of diabatic heating and a decomposition of vorticity into components oriented along and across isentropes (see their Section 4.1, Harvey et al., 2020). We offer a complementary perspective which considers the *moist* PV (MPV) of saturated updraft parcels. Chapter 3.2 details relevant MPV theory and provides a conceptual model for this perspective in the TC environment. Chapter 3.3 contains relevant methods, and Chapter 3.4 employs a simulation of Hurricane Fiona to demonstrate 1) the applicability of the proposed conceptual model and 2) that NPV parcels in the upper troposphere originated with negative MPV in the subtropical lower troposphere.

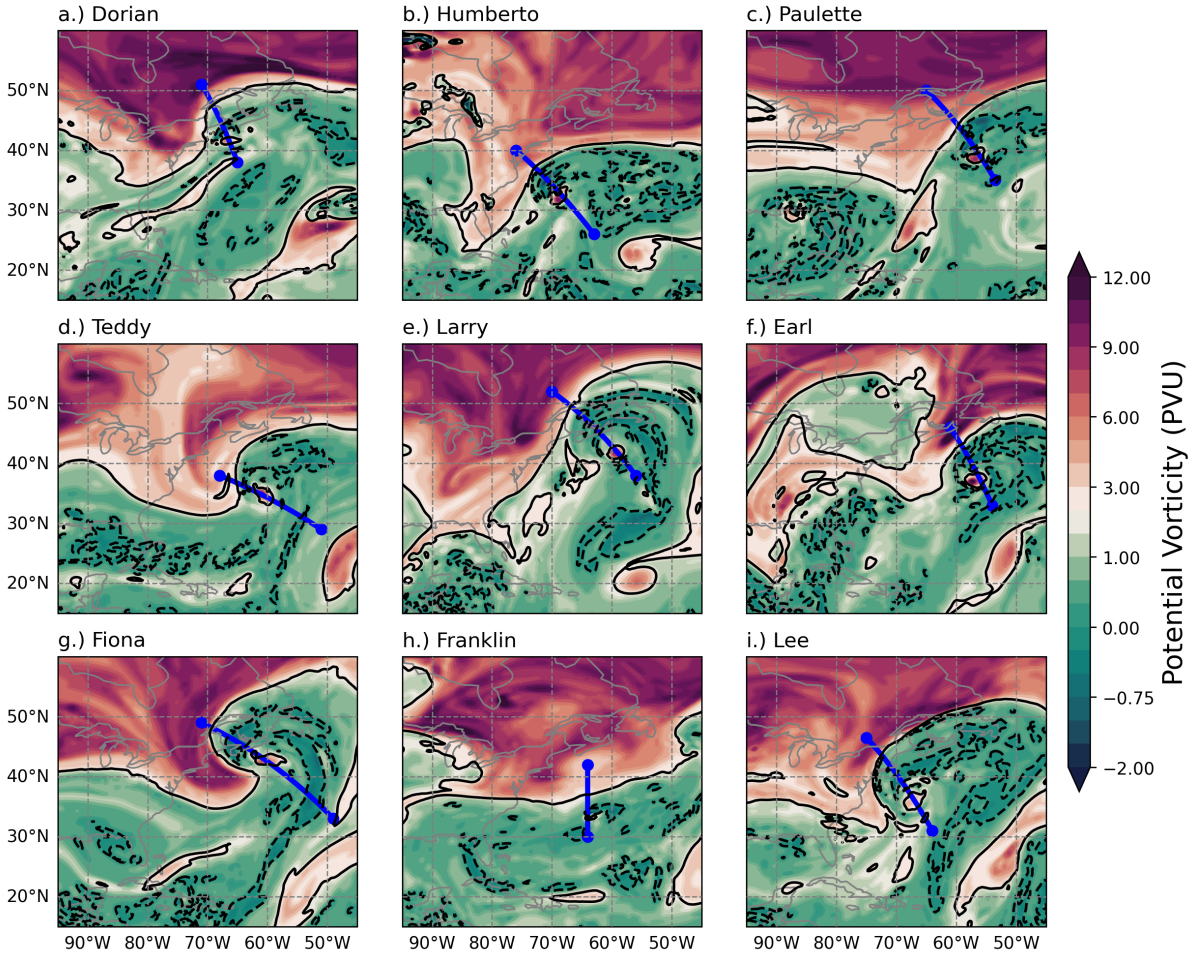

FIGURE 3.2: Potential vorticity (shaded), the 2 PVU isertel (solid black) and the 0 PVU isertel (dashed black) on the 350K isentropic surface during the extra-tropical transition of Hurricane a.) Dorian at 12Z 7 Sep 2019. b.) Humberto at 12Z 18 Sep 2019. c.) Paulette at 18Z 15 Sep 2020. d.) Teddy at 00Z 22 Sep 2020. e.) Larry at 18Z 10 Sep 2021. f.) Earl at 00Z 10 Sep 2022. g.) Fiona at 00Z 24 Sep 2022. h.) Franklin at 12Z 2 Sep 2023. i.) Lee at 12Z 15 Sep 2023.

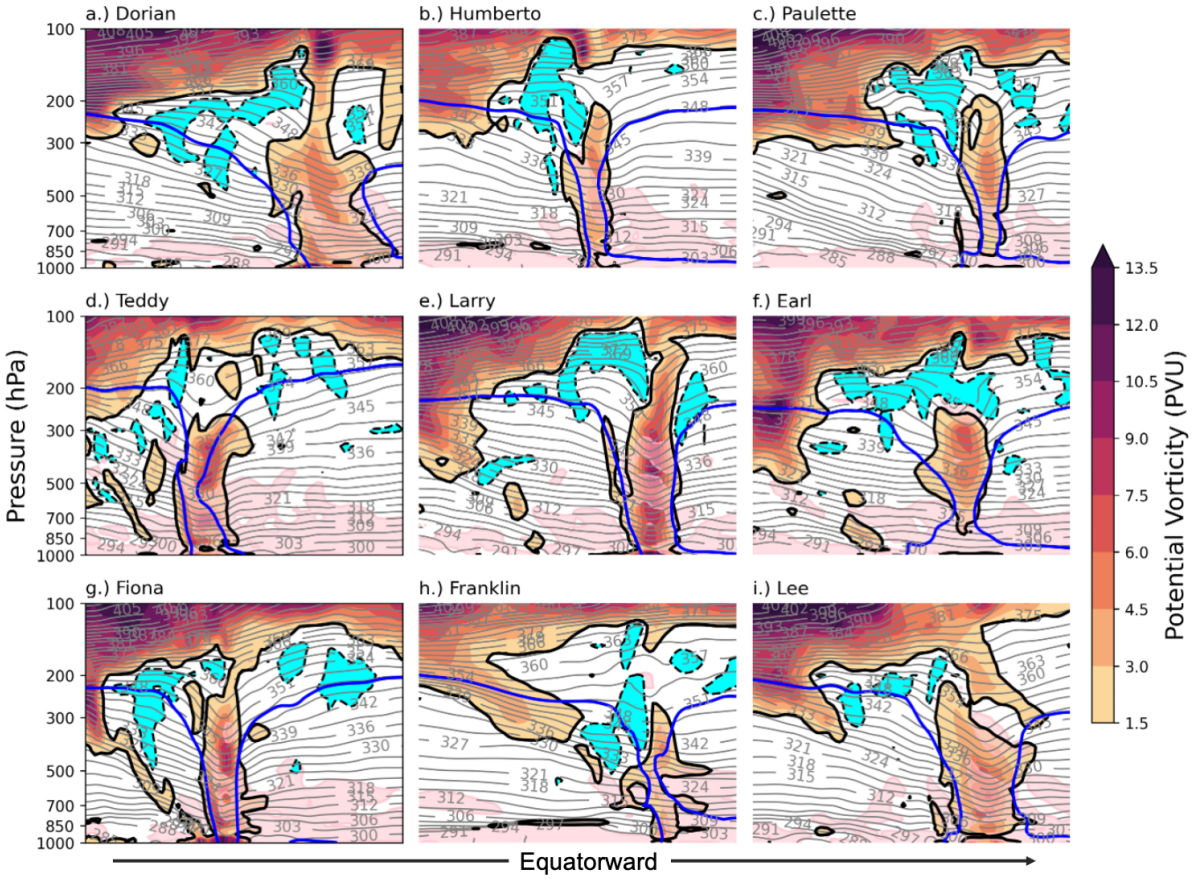

FIGURE 3.3: Potential vorticity greater than 2 PVU (orange shaded), the 2 PVU dynamic tropopause (solid black), the 0 PVU isertel (dashed black) and its attendant region of PV less than 0 (blue), isentropes (solid grey), the approximated moist entropy current (solid blue), and the region characterized by convective instability (pink) for the cross-sections indicated in Fig. 3.2 for Hurricane a.) Dorian at 12Z 7 Sep 2019. b.) Humberto at 12Z 18 Sep 2019. c.) Paulette at 18Z 15 Sep 2020. d.) Teddy at 00Z 22 Sep 2020. e.) Larry at 18Z 10 Sep 2021. f.) Earl at 00Z 10 Sep 2022. g.) Fiona at 00Z 24 Sep 2022. h.) Franklin at 12Z 2 Sep 2023. i.) Lee at 12Z 15 Sep 2023.

3.2 Theory

3.2.1 Moist potential vorticity

The MPV can be defined in Cartesian coordinates

$$P_e = \rho^{-1} \boldsymbol{\zeta}_a \cdot \nabla \theta_e, \tag{3.3}$$

where ρ is the density, $\boldsymbol{\zeta_a}$ is the three-dimensional absolute vorticity vector, ∇ the gradient operator, and θ_e the equivalent potential temperature. This form of MPV is sometimes referred to as the equivalent PV due to its choice of moist entropy variable. Its friction-less tendency equation is given

$$\frac{dP_e}{dt} = \rho^{-3} \nabla \theta_e \cdot (\nabla \rho \times \nabla p) + \rho^{-1} \boldsymbol{\zeta}_a \cdot \nabla \dot{\theta}_e \tag{3.4}$$

where $\frac{d}{dt}$ is the total derivative, p the pressure, and $\dot{\theta}_e$ the total equivalent potential temperature tendency (Marquet, 2014). Alternative forms of MPV which employ different moist entropy variables exist, however, we choose θ_e since 1) the resultant MPV has the same units as traditional dry Ertel's PV, 2) it collapses to the dry Ertel's PV when

there is no water vapor, and 3) this formulation directly contains information about the convective stability (i.e. the vertical gradient of θ_e).

While an ice-liquid entropy variable which respects the role of ice processes could be similarly employed (e.g. ice-liquid potential temperature, Tripoli and Cotton, 1981), the difference in latent heat release between fusion and vaporization is secondary and leads to moist entropy errors on the order of a few Kelvin (Simpson, 1978). This is also true of the increase in entropy associated with precipitation fallout (i.e. the difference between pseudo-adiabatic and reversible moist thermodynamic processes). While these neglected processes are undoubtedly important when considering the precise tendency of the chosen moist entropy variable (e.g. Kooloth et al., 2024), the additional complexity arising from their inclusion comes with little further physical insight in our intended use case. It will be shown using scaling arguments in Chapter 3.2.3 that these processes have relatively small effects on the MPV budget when the initial MPV is on the order of 1 PVU and the timescale is on the order of hours.

Schubert et al. (2001) identify several issues with the equivalent PV; the resultant MPV lacks both an invertibility principle and a non-zero solenoidal term. In this case, however, invertibility is not a desired attribute of our chosen MPV variable. More problematic is a non-zero solenoidal term since, even in the absence of $\dot{\theta}_e$, the right-hand side (rhs) of Eq. (3.4) can remain non-zero. The first term on the rhs of Eq. (3.4) does vanish, however, for saturated flows since θ_e becomes dependent only on temperature. So long as the flow is saturated and gradients in the $\dot{\theta}_e$ are weak, the zero-order MPV balance is

material conservation. This is a potential application of recent advances in MPV theory indicating that the MPV can sometimes be materially invariant when integrated over certain volumes, even in the presence of phase changes (Kooloth et al., 2024).

3.2.2 Application to the tropical cyclone environment

One region of particular interest where prolonged saturation occurs is within the eyewall updraft of TCs, sometimes identified by a continuous moist isentrope which links tropical boundary-layer air to the upper troposphere (Tripoli, 1992, see their Fig. 5g). We will refer to this as the moist entropy current (MEC) as it is the primary conduit of energy transfer between lower and upper troposphere in the TC environment (e.g. Rotunno and Emanuel, 1987). Since the mean-state MPV is negative in the tropical lower troposphere ($f > 0$ and $\frac{\partial \theta_e}{\partial z} < 0$, e.g. Jordan, 1958), the MEC is potentially a rare conduit upon which to transport boundary-layer air with negative MPV into the upper troposphere. Upon drying, this same air is characterized by negative dry Ertel's PV (NPV).

Examples of this phenomenon are provided for nine September tropical cyclones undergoing extra-tropical transition in the North Atlantic: Dorian, Humberto, Paulette, Teddy, Larry, Earl, Fiona, Franklin and Lee (Fig. 3.1). All nine cases featured upper-tropospheric synoptic or near-synoptic scale NPV features between the TC and the mid-latitude jet (Fig. 3.2a-i). Cross sections through these NPV features, the jet and the associated TC reveal they are often intersected by the MEC (Fig. 3.3a-i, blue lines) which links a lower-tropospheric region of convective instability (pink, identically negative MPV) to the upper tropospheric region of NPV (black dashed and blue shaded,

identically inertial instability).

This process is summarized in Fig. 3.4a and can be explained through the preservation of a negative MPV value during saturated ascent despite non-conservative processes (see Chapter 3.2.1 & 3.2.3). For simplicity, we will assume a dominant vertical component such that the MPV can be written

$$P_e \approx \rho^{-1} \frac{\partial \theta_e}{\partial z} \zeta_a. \tag{3.5}$$

In the boundary layer, θ_e decreases with height (i.e. convective instability, see pink) and the absolute vorticity is cyclonic, an arrangement consistent with negative MPV. Although TC inflow is sub-saturated (see dashed blue), these parcels eventually saturate (solid blue) and rise along the MEC, their outflow layer predetermined approximately by their equivalent potential temperature. Upon reaching the relatively dry upper troposphere, θ_e approaches θ and P_e approaches the dry Ertel's PV (P). Since the environment is very dry and strongly statically stable, preserved negative MPV (identically NPV at the dry limit) also manifests as a region of inertial instability ($\zeta_a f < 0$).

This simplistic perspective, however, only considers the stability conditions at lower and upper-tropospheric points along the saturated flow. A more complete understanding

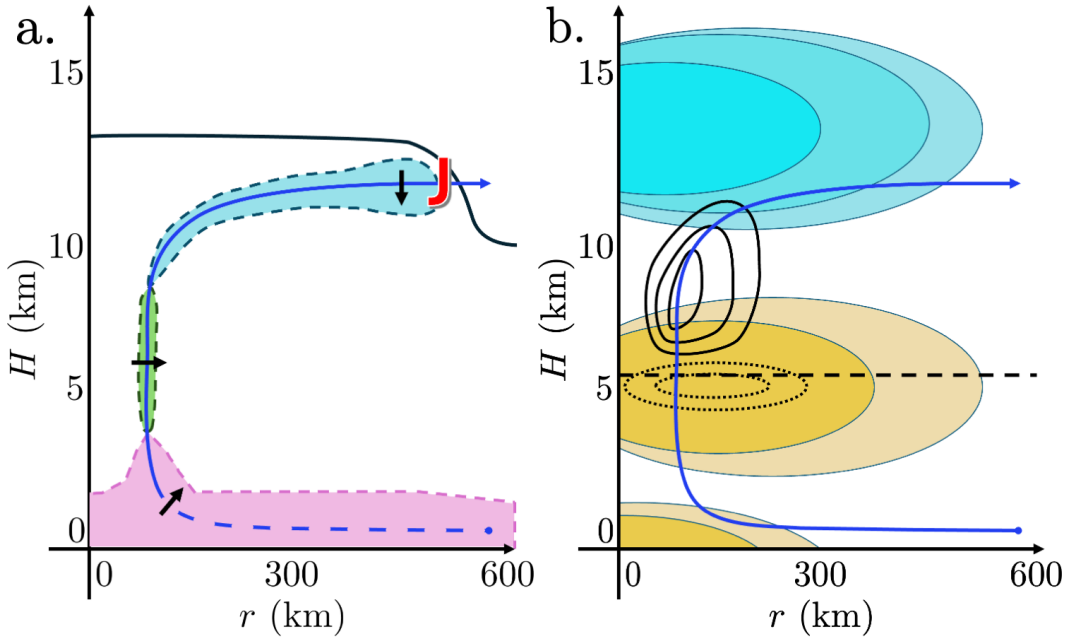

FIGURE 3.4: a.) The moist entropy current (dashed blue changing to solid upon saturation), the dynamic tropopause (solid black), the directionality of $\zeta_\perp$ (black arrow) and regions of convective, symmetric and inertial instability (pink, green and blue shaded, respectively) for an idealized tropical cyclone whose outflow interacts with the upper-level subtropical jet (J). b.) The moist entropy current (solid blue), the 0°C isotherm (heavy dashed black), diabatic heating associated with infrared radiation (oranges/blues, every 1 K d^{-1} and -1 K d^{-1} beginning at 1 K d^{-1} and -1 K d^{-1}, respectively) and the difference in diabatic heating between liquid and ice processes (solid black every 0.5 K h^{-1} and dotted black every -0.1 K h^{-1}) for an idealized tropical cyclone, as approximated from Ruppert et al. (2020) and Sawada and Iwasaki (2007), respectively.

arises upon returning to the full three-dimensional MPV. Partitioning the absolute vorticity vector into components oriented along ($\boldsymbol{\zeta}_\parallel$) and across ($\boldsymbol{\zeta}_\perp$) moist isentropic surfaces allows Eq. (3.3) to be written

$$P_e = \rho^{-1}(\boldsymbol{\zeta}_\parallel + \boldsymbol{\zeta}_\perp) \cdot \nabla\theta_e, \tag{3.6}$$

however, by definition, $\boldsymbol{\zeta}_{\parallel}$ does not project on $\nabla\theta_e$ and the MPV is identically

$$P_e = \rho^{-1}\boldsymbol{\zeta}_{\perp} \cdot \nabla\theta_e. \tag{3.7}$$

A negative value of MPV is observed when $\boldsymbol{\zeta}_{\perp}$ points towards lower values of θ_e. In the lower troposphere of a hypothetical TC, $\boldsymbol{\zeta}_{\perp}$ points radially upward and outward associated with a strong cyclonic circulation which decays with height (Fig. 3.4a). If negative MPV is preserved, $\boldsymbol{\zeta}_{\perp}$ must point radially outward in the middle troposphere, and downward in the upper troposphere as the flow exchanges instability states. Horizontal components of MPV dominate in the middle troposphere such that there is a horizontally thin region where symmetric instability may exist (i.e. the MPV is negative for a convectively and inertially stable, saturated flow). It is thought that the region of symmetric instability is horizontally narrow and therefore unlikely to be realized with appropriate fidelity in coarse resolution analyses. The upper-tropospheric unstable region is readily apparent since it represents amalgamations of TC outflow on horizontal scales much larger than the TC itself (Black and Anthes, 1971). There is no scarcity of negative MPV in the tropical boundary layer (Dey and O'Neill, 2022, see their Figs. 3 & 4 and our Fig. 3.3).

It should be noted that for axisymmetric, steady-state TCs the eyewall MPV is expected to be exactly zero due to the congruence of angular momentum and θ_e contours (i.e. slantwise moist neutrality, Emanuel, 1986). Under these assumptions, the solenoidal

term in Eq. (3.4) is eliminated regardless of sub-saturation since $\nabla\theta_e$ lies only in the height-radius plane and does not project onto the solenoidal vector. Further, the second term on the rhs of Eq. (3.4) is implied to be small, else gradients in $\dot{\theta}_e$ would force organized departures from slantwise moist neutrality. It is possible that the existence of NPV outflow in the TC environment is an indication of departures from slantwise moist neutrality, either by organized asymmetries (e.g. convective bursts, Steranka et al., 1986, Kelley and Halverson, 2011, Chen and Zhang, 2013) or an inhomogeneous θ_e tendency. The conceptual (Fig. 3.4a) and example TCs (Fig. 3.3) provided here are not assumed to be in steady-state and are strongly asymmetric due to the approaching upper-level trough.

3.2.3 Scaling of the MPV tendency for TC updraft parcels

While diabatic terms on the rhs of Eq. (3.4) are usually important (e.g. Schubert, 2004), consider the special case of frictionless, saturated flow such that the solenoidal tendency is annihilated and Eq. (3.4) becomes

$$\frac{dP_e}{dt} = \rho^{-1}\boldsymbol{\zeta}_a \cdot \nabla\dot{\theta}_e. \tag{3.8}$$

So long as the flow is saturated, along-flow latent heating is dominated by condensation

and $\dot{\theta}_e$ represents secondary diabatic heating effects such as radiation, the θ_e tendency associated with precipitation fallout, and the neglected portion of latent heating associated with ice processes. The MPV tendency, however, depends not on the magnitude of $\dot{\theta}_e$, but on its gradient. Assuming the vertical component of the MPV tendency dominates following the MEC, the change in MPV is given

$$\Delta P_e = \rho^{-1} \zeta_a \frac{\Delta \dot{\theta}_e}{\Delta z} \Delta t \tag{3.9}$$

where Δt represents the time that a parcel was subjected to a particular MPV tendency.

Idealized distributions of diabatic heating included in Fig. 3.4b are informed by Ruppert et al. (2020, see their Fig. 5a) and Sawada and Iwasaki (2007, see their Fig. 6), for radiation and the neglected latent heating from ice processes, respectively. Our figure represents an azimuthally averaged cross-section through the TC environment and, as in Fig. 3.3, the primary updraft region is identified using the MEC. Relevant scaling values are provided in Table 3.1, having calculated Δt assuming an updraft velocity of 0.25 m s^{-1} over 3 and 10 km for ice and radiation processes, respectively. Although this updraft velocity is likely conservative for ice processes (Smith and Montgomery, 2023, see their Fig. 10.17e), this assumption increases the amount of time a given MPV tendency is experienced, thereby increasing ΔP_e. This assumes that a parcel experiences the particular PV tendency for approximately 3 and 11 hours, respectively. Although

MPV tendencies will change signs at heating critical points, we assume no along-flow cancellation.

One can estimate the $\dot{\theta}_e$ associated with precipitation fallout by comparing the θ_e arising from reversible and irreversible (i.e. pseudo-adiabatic) saturated ascent over a specified period (e.g. Bolton, 1980, Bryan, 2008). If all condensate falls immediately from the rising parcel, the associated latent heat release is spread over a smaller mass, resulting in an approximately 4 K increase in θ_e from tropical boundary layer to upper troposphere. This tendency is relatively constant in the strongly precipitating region, but becomes an order of magnitude smaller in the dry upper troposphere. We estimate that this change occurs over about 5 km for an average updraft velocity of 0.25 m s^{-1}. Relevant scaling values are also included in Table 3.1.

Of these processes, the neglected latent heating associated with ice processes and precipitation fallout are most likely to produce a meaningful MPV tendency (Table 3.1). While the value of NPV/negative MPV in the upper tropospheric regions of interest (i.e. Fig. 3.3) is usually between -1 and -0.1 PVU in coarse-resolution reanalysis, the boundary-layer MPV in the tropical cyclone environment can approach strongly negative values from -1 PVU (Fig. 3.5) to, occasionally, -10 PVU (Dey and O'Neill, 2022, see their Fig. 4). Even if all the estimated tendencies conspired to increase the MPV, the anticipated increase is only about 0.3 PVU. Given that the directionality of the anticipated PV tendency must change at critical points in $\dot{\theta}_e$, it is likely that some along-flow cancellation

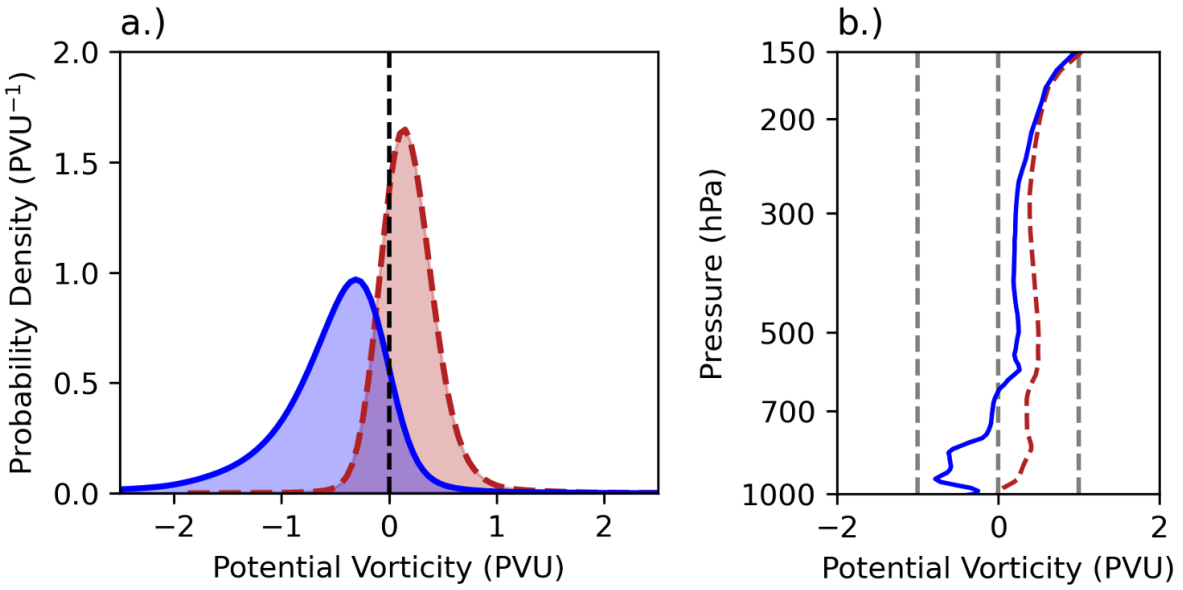

FIGURE 3.5: a.) Smoothed probability density functions for moist and dry PV (solid blue and dashed red, respectively) for the 1000–850 hPa layer for a region of the subtropical North Atlantic ocean (60–75°W, 20–34°N) from 00Z 21–25 September 2022 during the ET of Hurricane Fiona (MPAS simulation, see Chapter 3.3.2). b.) As in a.) except for the mean vertical profile of moist and dry PV (solid blue and dashed red, respectively).

TABLE 3.1: Approximate scaling values (columns) used to estimate the size of anticipated MPV tendencies and changes associated with the labeled process (rows). One can multiply the product of the first four columns by 1×10^6, the conversion factor to PVU, in order to produce the MPV tendency in the fifth column. The product of the fifth and sixth columns yields the anticipated change in MPV, having assumed the MPV tendency does not change signs following the flow.

Diabatic Process	ρ^{-1} (m^3 kg^{-1})	ζ_a (s^{-1})	$\Delta\dot{\theta}_e$ (K s^{-1})	$(\Delta z)^{-1}$ (m^{-1})	$\frac{dP_e}{dt}$ (PVU s^{-1})	Δt (s)	ΔP_e (PVU)
Ice Processes	1×10^0	1×10^{-4}	5×10^{-4}	3×10^{-4}	2×10^{-5}	1×10^4	0.2
Precipitation Fallout	1×10^0	1×10^{-4}	2×10^{-4}	2×10^{-4}	4×10^{-6}	2×10^4	0.1
Radiation	1×10^0	1×10^{-4}	4×10^{-5}	1×10^{-4}	4×10^{-7}	4×10^4	0.02

occurs both within and between processes. Although not a full interrogation of all processes which impact the MPV budget, these scalings indicate that updraft parcels whose MPV on the order of -1 PVU are likely to retain the negative value, albeit modified, into the upper troposphere.

3.3 Methods

3.3.1 Reanalysis, cyclone catalog, and satellite data

Analysis and calculations were performed in a meteorological python environment (May et al., 2016, 2022) using a variety of data. The climatological location of the September unimodal jet was defined as the mean location of the 3.1 PVU isertel in the 330–350 K isentropic layer using JRA3Q reanalysis from 1979–2022 (see Orr, 2024). These data were also used to calculate the anomalous time with NPV relative to the expectation at that latitude for the same isentropic layer (Fig. 3.1). Paths of ET events discussed in Chapters 3.1 and 3.2 were retrieved from the international Best Track Archive v4 (Knapp et al., 2018, Kenneth et al., 2019).

September hurricanes which transitioned into robust extra-tropical cyclones from 2018–2023 were first identified using composite visible satellite imagery available from the NASA Worldview tool (https://worldview.earthdata.nasa.gov/). The development of these systems into extra-tropical cyclones is diagnosed via application of the Sutcliffe-Trenberth form of the quasi-geostrophic ω-equation (Sutcliffe, 1947, Trenberth, 1978) using standard synoptic charts which include 500 hPa geostrophic relative vorticity, 1000–500 hPa thickness, 850 hPa geopotential height, and precipitable water from the 1.25° isobaric JRA3Q. The burgeoning presence of cyclonic vorticity advection by the thermal wind is physically consistent with the phase transition from symmetric warm-core to asymmetric cold-core structure (Hart, 2003). This specific methodology was employed

since it allows for simple evaluation of the post-tropical cyclone strength. Thus, our nine-storm catalog is effectively a "strong ET" subset of the 37 total ETs present from 2018–2023 in the International Best Track Archive. While the full evolution of each ET event is not shown, it is clear that each event is poised for robust development due to its phasing relative to the upstream trough (see our Fig. 3.2, e.g. Harr et al., 2000).

Given uncertainty regarding the ability of relatively coarse-resolution JRA3Q to adequately resolve NPV features on synoptic scales, it was supplanted by hourly 0.25° European Center for Medium-Range Weather Forecasts (ECMWF) Reanalysis v5 data (ERA5, Hersbach et al., 2020) in synoptic PV analyses and their associated cross-sections (e.g. Fig. 3.2 & 3.3). PV fields were interpolated to the 350K isentropic surface. No smoothing was performed on ERA5 isobaric or isentropic PV fields since arbitrary spatial smoothing can dramatically influence the representation of linear features with sub-synoptic widths. Derived variables equivalent potential temperature (θ_e), potential temperature (θ), and convective stability ($-\frac{\partial \theta_e}{\partial p}$) were subject to a light, 5-degree Gaussian smoother to improve visualizations.

3.3.2 MPAS simulation

An hourly, 4-day simulation of Hurricane Fiona was performed using the Model for Prediction Across Scales (MPAS, Skamarock et al., 2012) using a global 60–10 km variable mesh with an approximately 80° lat/lon refinement region centered over the western North Atlantic. This global simulation was initialized using the 0.25°, final operational global analysis at 00Z 21 Sep 2022 available from the National Center for Environmental

Prediction (i.e. NCEP GDAS/FNL) without sea-surface temperature updates. Output from the 60–10 km mesh simulation with 55 vertical levels was converted to a 0.1° latitude-longitude grid and interpolated to isobaric (39 levels every 25 hPa) and isentropic levels (at 350 K) as needed. Although comparable simulations were performed using the Weather Research and Forecasting (WRF, Skamarock et al., 2008) model, NPV features and inflow parcels were frequently outside the limited domain and/or were influenced by boundary conditions. This was also true for some limited domain MPAS meshes. While a 60–3 km global mesh is available for MPAS, its computational expense was beyond our allotted resources.

3.3.3 Lagrangian parcel trajectories

Parcel back trajectories were performed using a version of the Lagrangian analysis tool (i.e. Lagranto, Sprenger and Wernli, 2015) adapted for use with latitude-longitude MPAS output in its native vertical coordinate. Several meteorological variables non-native to the MPAS output described in Chapter 3.3.2 were calculated in a meteorological python environment prior to this analysis: temperature from potential temperature, dewpoint temperature from relative humidity, equivalent potential temperature from dewpoint temperature, absolute vorticity, and the vertical derivative of equivalent potential temperature (a proxy for convective stability). 2000 parcels were initialized every 50 m from 7 to 14.5 km along the geodesic denoted in Figs. 3.7f & 3.8c-d at 00Z on 24 Sep ($N = 3 \times 10^5$ equally spaced parcels between 77.5°W, 47°N $\rightarrow$ 66.5°W, 20.5°N). Parcel velocities were updated every 5 minutes, their positions and environmental conditions output hourly over

a three day period. These parcels were grouped based on their final PV and origin: positive PV which originated above 3.5 km (≈55%), positive PV which originated below 3.5 km (≈36%), NPV from 0 to -0.4 PVU which originated in the lower troposphere (≈7.5%), and NPV less than -0.4 PVU which originated in the lower troposphere (≈1.8%).

The tracing of meteorological variables allows calculation of the along-trajectory equivalent potential temperature tendency ($\dot{\theta}_e$) at hourly resolution. Assuming saturation and that horizontal gradients in $\dot{\theta}_e$ are small, the parcel group-average MPV pseudo-tendency is approximated

$$\frac{dP_e}{dt} \approx \rho^{-1}\zeta_a \frac{\Delta\dot{\theta}_e}{\Delta z} \tag{3.10}$$

where ρ and ζ are averaged across the parcel group and Δ is the 3-point centered difference of group-average variable over time. This was only calculated for the period in which the average sNPV parcel was ascending (i.e. from 0 to -42 hours) since Eq. (3.10) is sensitive to small δz during the inflow period (-42 to -70 hours). Eq. (3.10) was similarly evaluated for the dry PV pseudo-tendency by replacing $\dot{\theta}_e$ with $\dot{\theta}$ and P_e with P in Eq. (3.10). Both pseudo-tendencies are comparable to independent calculations of the along-trajectory MPV and PV tendencies (see Appendix C.1).

This analysis can be understood conceptually using Fig. 3.4b by tracing a parcel along

the MEC through the middle-tropospheric region of strong ice processes. We denote Eq. (3.10) the MPV *pseudo*-tendency since 1) it neglects contributions from horizontal gradients in $\dot{\theta}_e$, 2) assumes saturation despite the presence of sub-saturated parcels and 3) should be interpreted only as an approximation of the sign and magnitude of the true MPV tendency. The MPV pseudo-tendency is used to evaluate the scale analysis presented in Chapter 3.2.3. Limitations associated with this methodology are discussed in Chapter 3.5.2.

3.4 Hurricane Fiona

3.4.1 Synoptic overview

From 00Z 21 Sep to 00Z 23 Sep 2022, Fiona was near 70°W moving northeastward as a strong TC in a region of weak vertical shear and high precipitable water (Fig. 3.6a-d). Fiona was embedded within the western side of an upper-level subtropical ridge, the body of which was partially comprised of NPV air on the 350 K isentropic surface (Fig. 3.7a-d). Cold air advection associated with a developing trough over the Great Lakes region reached the mid-Atlantic at 00Z on 23 Sep 2022, nearing still-tropical Fiona (Fig. 3.6d). Over the subsequent 24 hours, Fiona's cyclonic wind field expanded dramatically and, at 00Z 24 Sep, the surface cyclone was located in a region of strong cyclonic vorticity advection by the thermal wind (Fig. 3.6f). Fiona then re-intensified as a mid-latitude cyclone along the Canadian Maritime from 00Z–12Z 24 Sep (Fig. 3.6f-g). By 12Z 24 Sep, Fiona showed signs of maturity; warm and cold frontal regions divorced from the

storm center and vertical stacking between lower and upper-level troughs (Fig. 3.6g). This coincided with a cyclonic Rossby wave break (i.e. overturning of the 2 PVU isertel on the 350 K isentropic surface) and a rapid deterioration in the amount of near-storm NPV at 350 K (Fig. 3.7g). This wave-breaking process continued over several more 12 hr analysis periods (not shown), however, by 00Z 25 Sep the near-storm NPV feature had dissipated (Fig. 3.7h).

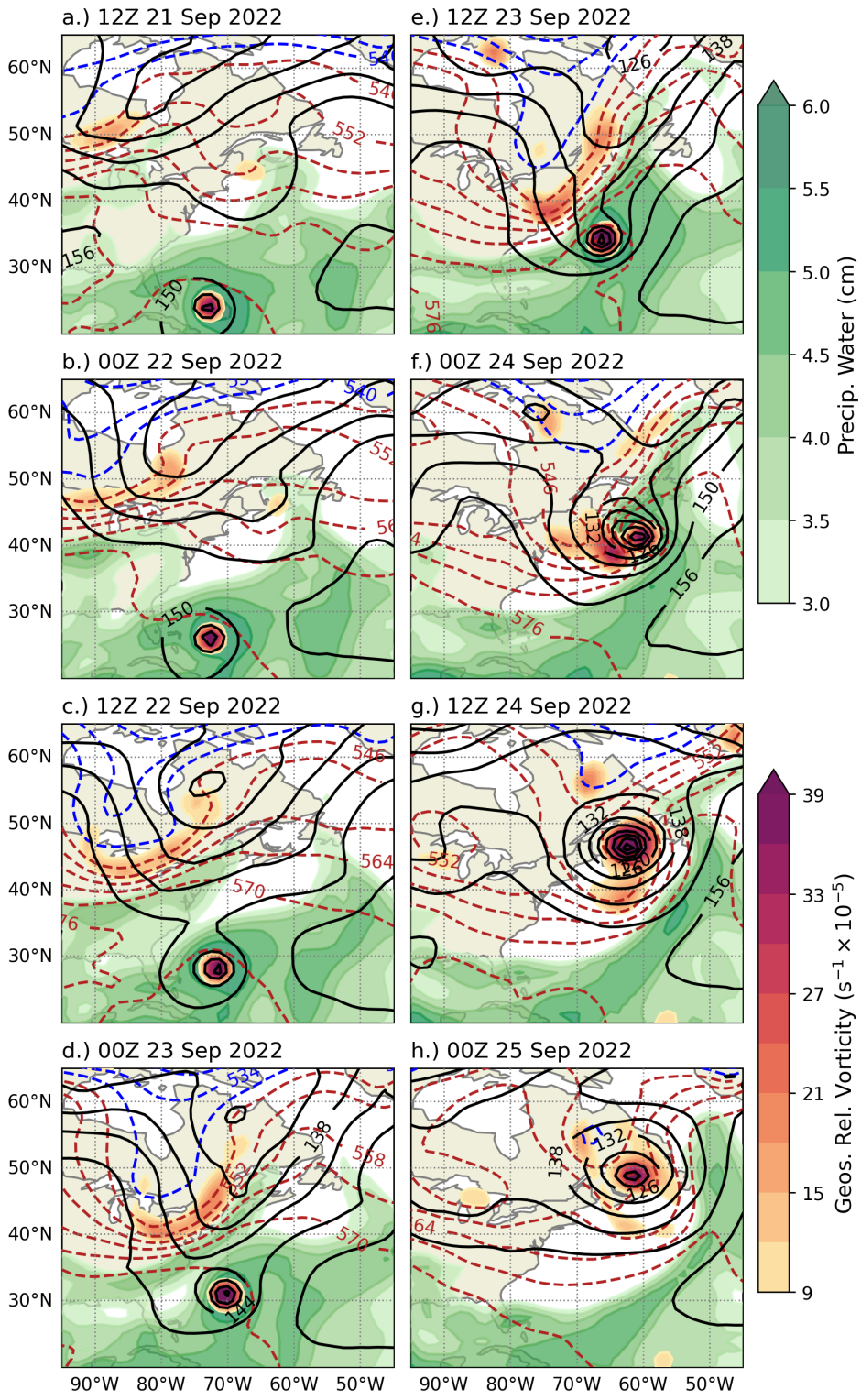

FIGURE 3.6: a.) Smoothed, JRA3Q representation of 850 hPa geopotential height (solid black every 60 dam), 1000–500 hPa thickness (dashed blue every 60 dam changing to red above 540 dam), geostrophic relative vorticity (shaded oranges) and precipitable water (shaded greens) at 12Z 21 Sep 2022. b-h.) as for a.) except at the printed time.

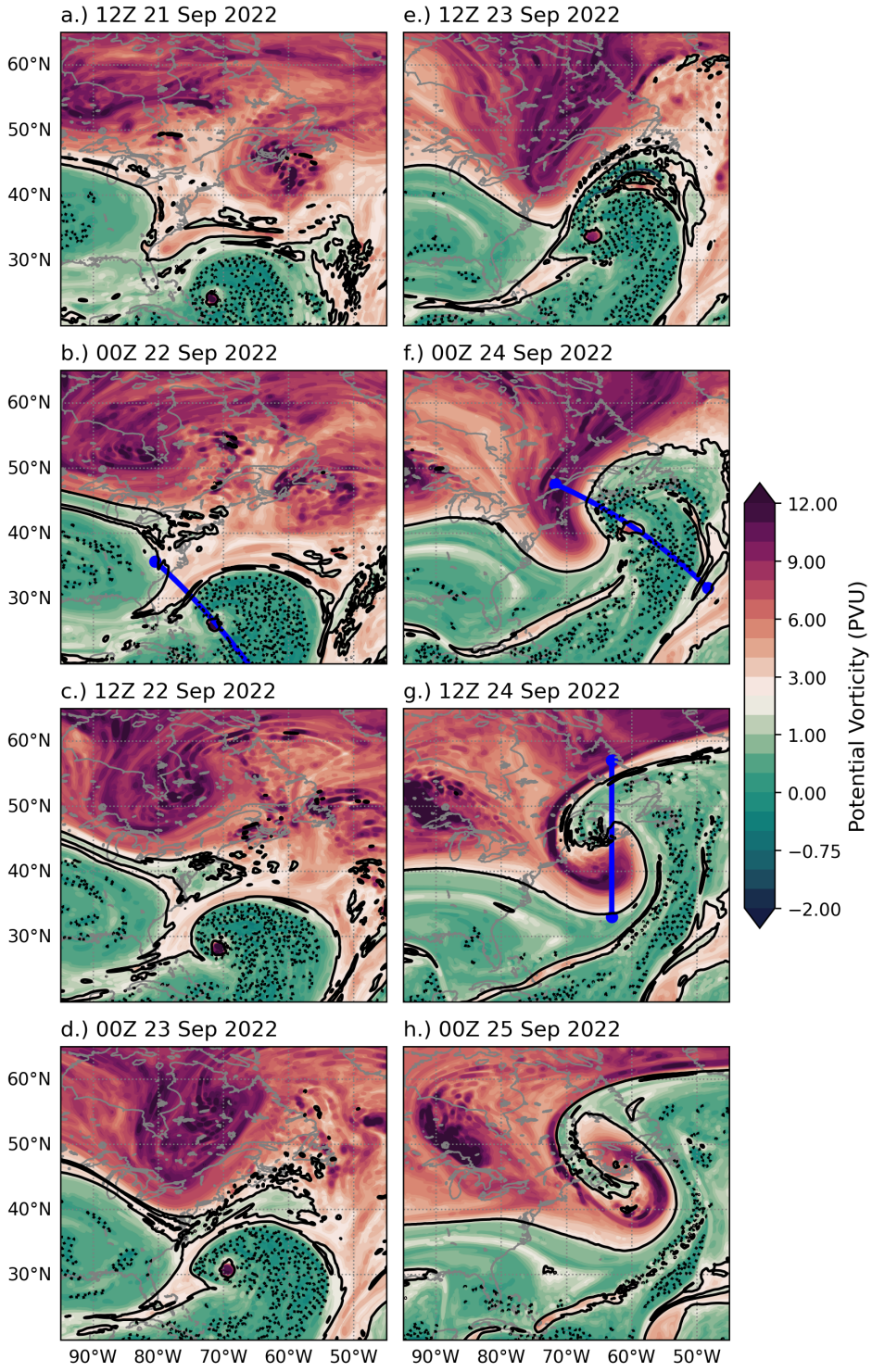

FIGURE 3.7: a.) Unsmoothed, MPAS representation of potential vorticity (shaded greens/blues), the 2 PVU dynamic tropopause (solid black) and the zero PVU isertel (dotted black) on the 350 K isentropic surface at 12Z 21 Sep 2022. b-h.) as in a.) except at the printed time.

3.4.2 Vertical cross sections

Despite the presence of a nearby jet-front feature, Fiona was still distinctly tropical in nature at 00Z 22 Sep (Fig. 3.6b & Fig. 3.7b). A cross-section through the TC at this time reveals a vertically-stacked tower of high PV extending through Fiona's warm core from surface to upper troposphere (Fig. 3.8a). At distance from Fiona, the subtropical upper troposphere is characterized by a relatively deep layer of low and negative PV air at potential temperatures greater than 350 K. Simultaneously, the lower troposphere is characterized by an abundance of convectively unstable air with negative MPV. These two regions of upper and lower level instability lie along a range of moist isentropic surfaces from roughly 348 to 354 K. The presence of potential symmetric instability along these moist isentropes indicates there may be transition from convective to symmetric to inertial instability during saturated ascent (see Chapter 3.2.2).

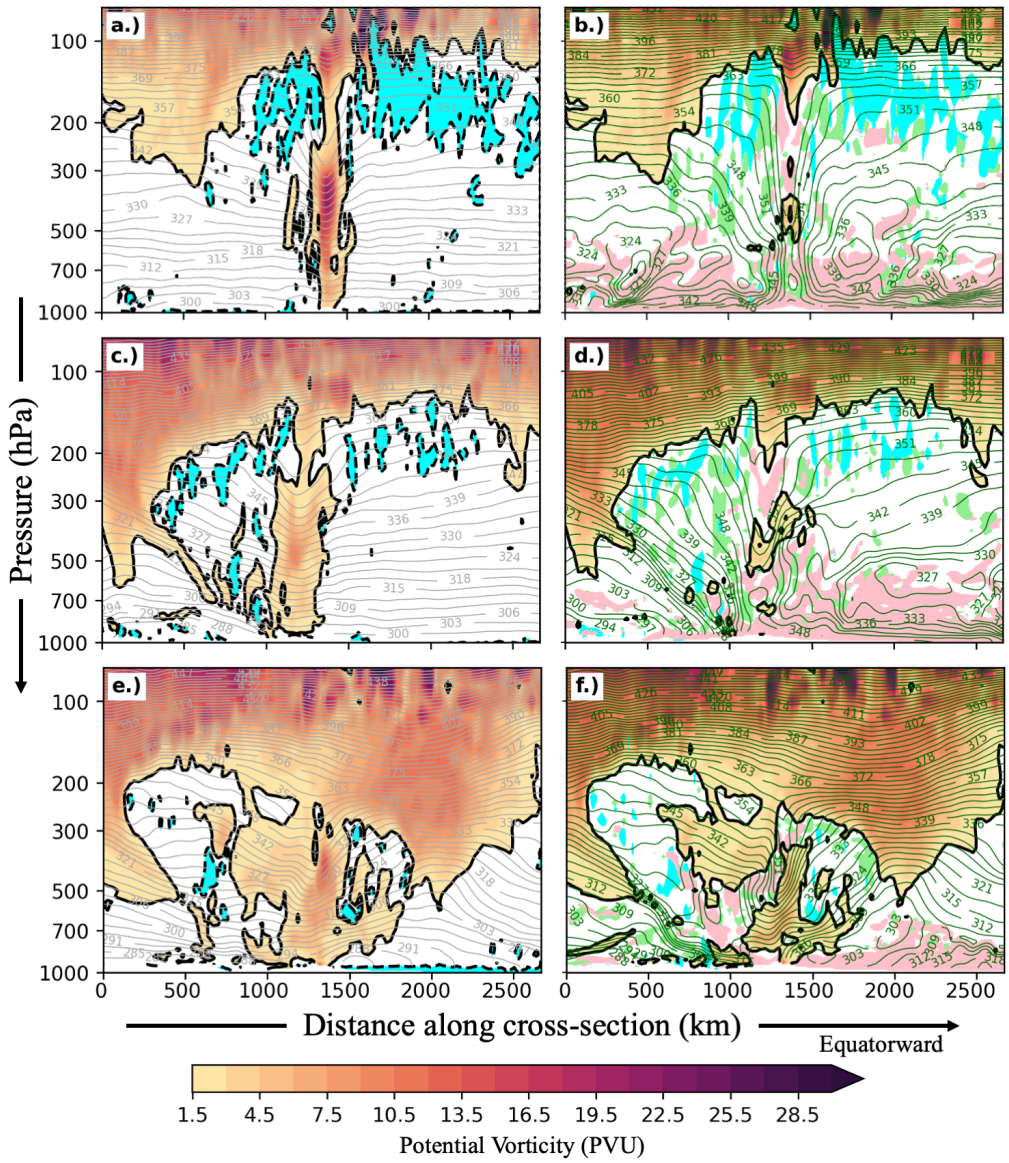

FIGURE 3.8: a.) PV greater than 1.5 PVU, the 1.5 PVU dynamic tropopause (solid black), lightly smoothed isentropes (solid grey) and NPV (dashed black and shaded teal) for Hurricane Fiona at 00Z 22 Sep 2022 along the cross-section indicated in Fig. 3.7b (80.45°W, 35.65°N → 63.71°W, 16.65°N). b.) MPV greater than 1.5 PVU (orange shaded), the 1.5 PVU *moist* isertel (solid black), lightly smoothed equivalent potential temperature (solid green), and convectively, potentially symmetrically, and inertially unstable air (shaded pink, green and teal, respectively) for the same cross-section as in a.). c.) & d.). As in a.) & b.) except along the cross-section indicated in Fig. 3.7f (71.72°W, 47.54°N → 48.29°W, 31.59°N). e.) & f.) As in a.) & b.) except along the cross-section indicated in Fig. 3.7g (63°W, 57°N → 63°W, 33°N).

These unstable regions are all characterized by negative MPV, but only in the dry upper troposphere are negative moist and dry PV highly correlated. Comparing MPV and PV in lower, middle and upper-tropospheric isobaric layers through the cross section at 00Z on 22 Sep 2022 (Fig. 3.9a-c) reveals that, upon reaching the upper troposphere, dry PV is effectively described by the MPV. In addition, while negative MPV describes convective instability in the lower troposphere (pink triangles, Fig. 3.9a), it tends to describe potential symmetric instability (green stars) and inertial instability (teal squares) in the middle and upper troposphere, respectively (Fig. 3.9a-c). While there are regions of potential symmetric instability in the regions outlying the MEC (Fig. 3.8b), saturation must be achieved for them to represent the presence of instability.

At 00Z 24 Sep, Fiona was in the midst of extra-tropical transition with distinct frontal features and strong quasi-geostrophic forcing for ascent (Fig. 3.6f). A vertical cross-section through the cyclone and its nearby trough-ridge couplet reveals a warm core structure and vertically stacked PV tower (Fig. 3.8c). A vigorous jet in the 500–200 hPa layer was associated with a deep-tropospheric frontal region on the poleward/westward side of the cyclone. The anticyclonic shear side of this jet feature (i.e. equatorward of the dynamic tropopause) was characterized by a deep layer of NPV air (negative MPV and inertially unstable, Fig. 3.8d). The substantial depth of NPV on the equatorward side of the jet feature is consistent with the range of outcropping moist isentropes on the poleward side of the surface cyclone. Although cold, dry mid-latitude air was encroaching on the surface cyclone, a substantial reservoir of convectively unstable (negative MPV) air still existed in the subtropical lower troposphere (Fig. 3.8d).

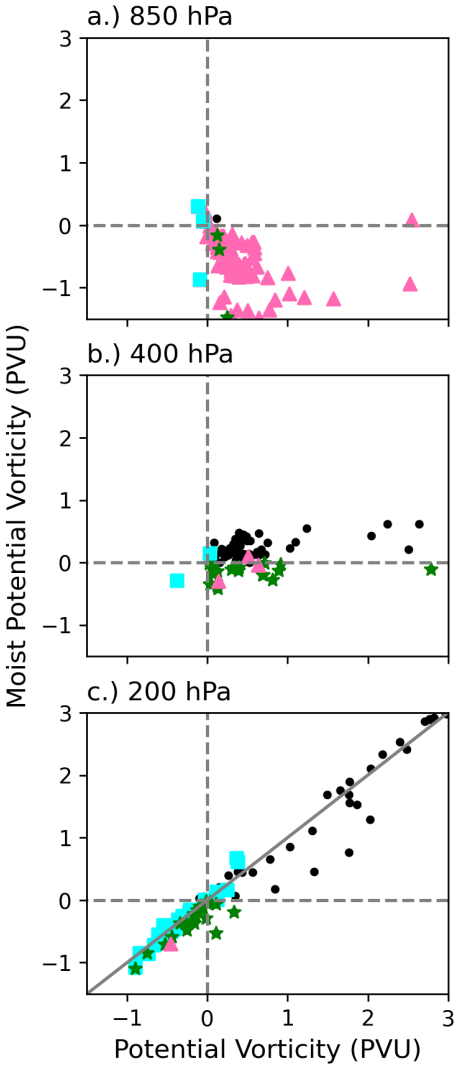

FIGURE 3.9: a.) Moist versus dry PV for points characterized by positive MPV (black dots) and convective (pink triangles), potential symmetric (green stars) and inertial instability (teal squares) at 850 hPa along the cross-section taken at 00Z on 22 Sep 2022 (Fig. 3.8a). b.) as in a.) except at 400 hPa. c.) as in a.) except at 200 hPa and including a line intersecting the origin with a slope of 1 (solid grey).

By 12Z on 24 Sep, Fiona had reached maturity as an extra-tropical cyclone (Fig. 3.6g) and a robust cyclonic Rossby wave break was ongoing along the dynamic tropopause (Fig. 3.7g). A cross-section through the wave break and lower-tropospheric cyclone reveals,

however, that a weak warm core persisted in middle-levels (Fig. 3.8e). A lack of lower-tropospheric moisture content led to a dramatic decrease in the depth of the convectively unstable layer in the lower troposphere (Fig. 3.6g & Fig. 3.8f). Outcropping moist isentropes still existed along the cold-frontal region towards the pole, however, this region was strongly convectively stable and is no longer representative of organized convective updrafts. Some remnant regions of NPV persisted on the anticyclonic side of the upper-level jet, however, these were located in the trough of warm air aloft characteristic of mid-latitude occlusion and were becoming disconnected from the subtropical reservoir of negative MPV air. The production mechanism for upper-tropospheric NPV air was no longer ongoing, and remnant NPV features would mix out over the subsequent few analysis periods (Fig. 3.7h). The rapid loss of inertially unstable air between 24 and 25 Sep is consistent with the e-folding time associated with inertially unstable perturbations (approximately 12 hours for $\zeta_a \approx -1 \times 10^{-5}$ s^{-2}). Overturning and discontinuities along the dynamic tropopause also indicate the loss of inertially unstable air occurred during a period of robust mixing along the dynamic tropopause (Fig. 3.7g & h).

3.4.3 Lagrangian parcel trajectories

In order to better evaluate the origin of NPV parcels in the upper-troposphere, Lagrangian back trajectories were calculated every 50 meters in the 7–14.5 km isohypsic layer at 2×10^3 locations along the cross-section taken at 00Z 24 Sep 2022 (Fig. 3.8c & d). Approximately 45% of these parcels originated in the lower troposphere beneath 3.5 km before rising into the upper troposphere. Of parcels which originated in the lower troposphere, 26%

reached the upper troposphere with NPV ($N_{\mathrm{NPV}} = 22619$). A subset of parcels which had strongly negative PV at initialization ($P < -0.4$ PVU) were retained for further analysis ($N_{\mathrm{sNPV}} = 5323$). The group-average environmental conditions are relatively robust to choice of NPV threshold, even to the extent of including all NPV parcels. This subset is chosen, however, so as to isolate the subsequent analysis from along-flow entrainment of high PV air in the hours before initialization.

A random selection of trajectory paths representative of each sample size is presented in Fig. 3.10. Not all outflow parcels reach the upper troposphere with NPV, however, the vast majority of NPV parcels travel through the TC circulation. These trajectory subselections are seeded for reproducibility, however, this conclusion appears robust to seed choice. These NPV parcels incur strongly positive PV as members of the TC primary circulation, and, therefore, must undergo substantial diabatic heating before entering the upper troposphere. Not all parcels which originated in the lower troposphere enter the TC circulation, therefore, we estimate that about a quarter of sampled outflow parcels reach the upper troposphere with NPV. It is unclear whether this ratio is true of the broader outflow region, however, it is certain that the sampled NPV structures are linked directly to the subtropical lower troposphere via the TC secondary circulation and, therefore, the MEC.

Given the relatively large sample size of NPV parcels, we attempt to shield calculation of Eq. (3.10) from mixing processes by isolating only those parcels with PV $< -.04$ PVU ($N_{\mathrm{sNPV}} = 5323$). The average parcel in this subgroup 1) originates in the subtropical

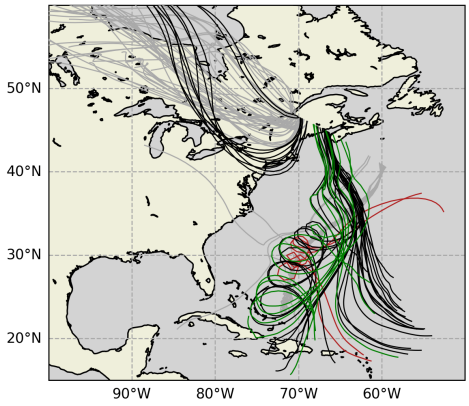

FIGURE 3.10: Example parcel trajectories from different parcel subgroups: parcels which originated above 3.5 km (grey, 32% of total), parcels which originated below 3.5 km but had positive PV at initialization (black, 45% of total), parcels which had PV between 0 and -0.4 PVU (green, 7.5% of total), and parcels which had PV less than -0.4 PVU (red, 1.8% of total). The number of parcel paths for each group is approximately consistent with their respective sample size, however, those which originated above 3.5 km are substantially under-represented since some originated outside the domain (omitted, 23%).

lower troposphere before ascending into the upper troposphere (Fig. 3.11a), 2) nears saturation while heating is strong (Fig. 3.11b-c) and 3) has a coincident maximum in $\dot{\theta}$ & $\dot{\theta}_e$ during ascent (Fig. 3.11c & d). These are all indications that these parcels have ascended through the TC secondary circulation, item 3) in particular suggesting that ice and precipitation processes dominate the θ_e budget. The average change in θ_e from lower to upper troposphere was 5 K.

Prior to 06Z 22 Sep (-42 hours), the MPV pseudo-tendency is highly sensitive to small height changes and, as discussed in Chapter 3.3, values are damped to zero (Fig. 3.11e). The full MPV tendency is known to be non-negligible during this period due to strong fluxes of θ_e which occur along the TC inflow. At 12Z 22 Sep (-36 hours), the average sNPV parcel reaches a relative humidity near 85% and begins to rise within the TC secondary

circulation (Fig. 3.11a & b). The diabatic heating increases quasi-linearly by about 1 K d^{-1} per hour between 12Z 22 Sep and 12Z 23 Sep (-12 hours) before increasing rapidly from 25 K d^{-1} to nearly 90 K d^{-1} (Fig. 3.11d). This is coincident with an increase in $\dot{\theta}_e$ from 1–3 K d^{-1} to around 20 K d^{-1} at 18Z 23 Sep (-6 hours, Fig. 3.11c). This occurs near freezing level when parcels are rising most rapidly, further supporting the conclusion that the maximum in $\dot{\theta}_e$ is associated with ice and precipitation processes occurring along the MEC.

Prior to rapid ascent at 18Z 23 Sep (-6 hours), the MPV pseudo-tendency is on the order of $1-2\times10^{-5}$) with frequent sign changes (i.e. the tendency is not dominated by precipitation fallout or radiation). When the parcel is beneath the heating maximum associated with ice processes at 18Z 23 Sep (-6 hrs), however, the MPV pseudo-tendency maximizes around 5×10^{-5} PVU s^{-1}. As the parcel passes through this heating maximum, the MPV pseudo-tendency changes sign and minimizes around -3 $\times10^{-5}$ PVU s^{-1}. Inconsistent magnitudes between these two critical points in MPV pseudo-tendency is potentially due to sublimation beneath the freezing layer and/or the along-flow decreases in absolute vorticity and density. Although the MPV pseudo-tendency briefly reaches values greater than that of our scaling, the time-integrated effect of these tendencies during the period of ascent (from 12Z 22 Sep to 00Z 24 Sep) is for a change in MPV of -0.07 PVU. This is for a group of inflow parcels whose initial MPV scales like -1 PVU, thus meeting the criteria for approximate MPV conservation described in Chapters 3.2.2 & 3.2.3. When calculated for the full group of NPV parcels (N_{NPV}), the anticipated MPV change is -0.08

PVU, thus, the difference between the N_{NPV} and N_{sNPV} is related to their MPV initial value.

While the average sNPV parcel originates in a convectively unstable lower troposphere, convective stability is achieved 15 hours before inertial instability occurs (Fig. 3.11g & h). If MPV conservation is assumed to first order, symmetric instability must be present within the updraft. This was anticipated in Chapter 3.2.2 due to the required geometry of $\nabla\theta_e$ and $\boldsymbol{\zeta}_{\perp}$ for an idealized NPV parcel (Fig. 3.4a). This conceptual model is further supported by cross sections revealing potential symmetric instability in the middle troposphere throughout Fiona's ET (Fig. 3.8 & 3.9).

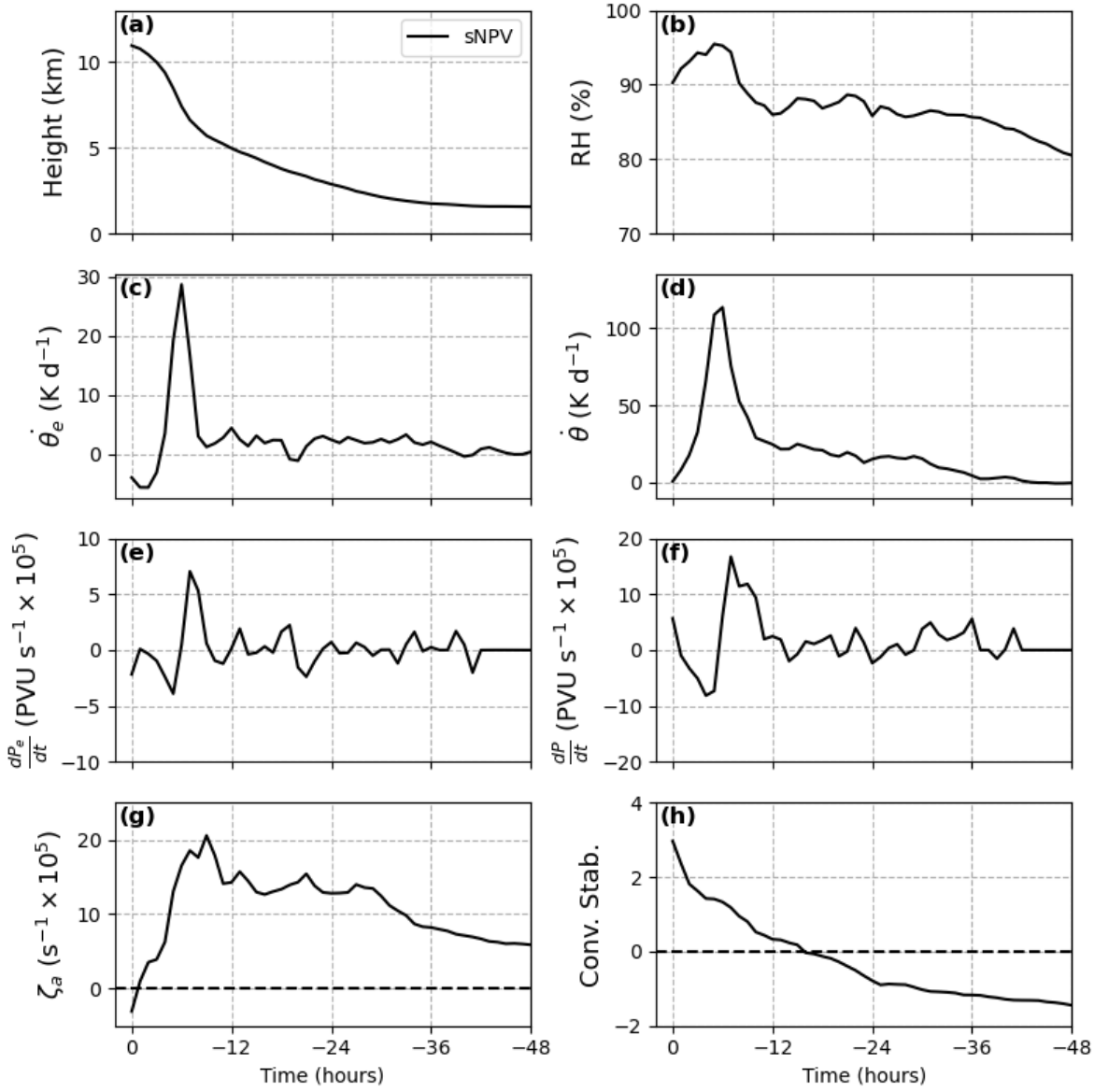

FIGURE 3.11: a.) Height of the average parcel with NPV < -0.4 PVU over the trajectory period ($N_{\text{sNPV}} = 5323$). b-h.) as in a.) except for b.) relative humidity. c.) the along-trajectory equivalent potential temperature tendency. d.) the along-trajectory potential temperature tendency. e.) the MPV pseudo-tendency. f.) the dry Ertel's PV pseudo-tendency. g.) absolute vorticity. h.) the convective stability proxy.

3.5 Discussion

3.5.1 Summary and conclusions

We argue that the appearance of upper-level NPV, especially on the equatorward side of the mid-latitude jet streams, can be understood intuitively using an MPV perspective. This is illustrated using an idealized TC conceptual model and several exemplary ET cases. Put simply, convectively unstable parcels in the subtropical lower troposphere have negative values of MPV. During saturated ascent, the initial value of negative MPV is often preserved into the upper troposphere where, due to low moisture content, it manifests equivalently as negative dry Ertel's PV. This potentially explains the seeming ubiquity of quasi-linear NPV amalgamations on the anticyclonic flank of the mid-latitude jet during ET events (e.g. Grams and Archambault, 2016, Prince and Evans, 2022). Although it is thought that this perspective has applications beyond ET (e.g. warm conveyor belts, Oertel et al., 2020), the cases provided here are beautifully illustrative.

Our analysis does indicate that the aforementioned simplification ignores requisite potential symmetric instability in the middle troposphere (i.e. inertial and convective stability with negative MPV). Since the component of absolute vorticity which contributes to the MPV is that which projects onto the moist entropy gradient, retention of negative values in the TC updraft demands an across-moist isentrope portion of vorticity which points radially upward, outward and downward in the lower, middle and upper troposphere, respectively. This is consistent with an exchange from convective to symmetric to inertial

instability following the saturated flow. This is introduced conceptually via Fig. 3.4a and is consistent with our analysis of Hurricane Fiona, which featured a deep layer of potential symmetric instability in the middle troposphere.

Although it is true that MPV is rarely, if ever, conserved in nature, the MPV tendencies which occur during saturated ascent are thought to be small for saturated parcels traveling through TC updrafts (e.g. along the MEC, see Chapter 3.2.3). MPV budget scale analysis for these parcels tends to agree with calculations of an MPV pseudo-tendency for a large sample of NPV parcels in Hurricane Fiona's outflow layer. In that case, MPV tendencies on the order of $1-5\times10^{-5}$ PVU s^{-1} were observed in association with a shallow region of strong heating attributed to ice processes. The time-integrated effect of these tendencies indicate non-negligible cancellation such that the average NPV parcel experienced an MPV change on the order of -0.1 PVU from lower to upper troposphere.

Since the majority of boundary-layer parcels in the large-scale vicinity of Hurricane Fiona had MPV values from -1.3 to 0.3 PVU (Fig. 3.5), non-conservation processes are potentially responsible for limiting the number of outflow parcels which retain negative MPV throughout ascent to *only* those on the lower quartile of the MPV distribution. Parcels with weakly negative MPV in the lower troposphere are likely to achieve inertial neutrality before reaching the upper troposphere with positive, albeit low PV. This perspective is in agreement with the long-standing notion that TC outflow is comprised of a mix of inertially unstable, neutral and stable air (e.g. Black and Anthes, 1971, Wang et al., 2021, Rowe and Hitchman, 2026).

3.5.2 Limitations and implications

There are several limitations to the present study which beckon further consideration. Principally, MPAS does not natively calculate moist PV without substantial modification. This complicates MPV budget analysis since calculations will accrue error due to finite differencing over model output (e.g. Morris et al., 2025). We present the MPV pseudo-tendency as described in Chapter 3.3.3 1) to avoid non-native finite differencing of the calculated θ_e field to produce $\dot{\theta}_e$ and its gradient, and 2) because both MPV and PV pseudo-tendencies compare well against noisier calculations of the along-trajectory tendencies (see Appendix C.1).

Both the approximate scalings outlined in Chapter 3.2.3 and our MPV pseudo-tendency ignore the effect of along-flow mixing, friction, sub-grid processes, and, notably, horizontal heating gradients. It is likely that these processes can produce PV tendencies on the same order as those associated with precipitation fallout and ice processes. These neglected processes may further explain why only a quarter of sampled outflow parcels featured NPV in our simulation of Hurricane Fiona; inflow parcels with weakly negative MPV values can experience a meaningful relative change.

One concern common to a variety of forecast models is that convective parameterization schemes potentially misrepresent low and negative PV structures (e.g. Clarke et al., 2019). It is possible that similar issues are present in our simulation of Fiona since the MPAS mesh refinement only reaches 10 km. The authors are currently investigating how

MPAS might be harnessed to calculate a robust, model-native MPV budget at higher spatial and temporal resolution. This could potentially side-step issues with convective parameterizations, while also providing a robust tool with which to interrogate the full, three-dimensional MPV budget in a variety of weather phenomena.

It is unclear if this MPV perspective applies in axisymmetric, steady-state TCs whose circulations are well-approximated by moist neutrality (i.e. $P_e = 0$ along the MEC, Emanuel, 1986). This environment guarantees elimination of the solenoidal term in the MPV budget, even under subsaturation, since the gradient of moist entropy lies in the height-radius plane and does not project onto the solenoidal vector. Thus, a first order MPV conservation principle is tacitly assumed by Emanuel (1986, see their Appendix II) in their TC conceptual model's eyewall region (their Region II). It is likely that incongruence between θ_e and angular momentum contours (i.e. departures from slantwise neutrality) during convective bursts or in spiral rain bands may account for NPV outflow even in mature TCs.

It is important to note the likely agreement between our results and those concerning the role of warm conveyor-belt convection in producing low and negative PV in extra-tropical cyclone outflow (Martínez-Alvarado et al., 2016, Harvey et al., 2020, Oertel et al., 2020, 2021). In the dry PV perspective outlined by Harvey et al. (2020), mesoscale convection embedded within the warm conveyor belt yields PV erosion capable of producing NPV. They and Oertel et al. (2021) note the importance of ambient vertical wind shear such that the resulting NPV manifests principally along the jet's anticyclonic flank. This

behavior is noted on the poleward side of all nine of our ETs, however, NPV also exists in the weakly sheared regions towards the equator (Fig. 3.2 & 3.3). The authors are actively applying the dry PV framework outlined by Harvey et al. (2020) to investigate whether the warm core of mature TCs demands vertical shear sufficient for the production of NPV far from the jet environment.

Chapter 4

Axisymmetric negative potential vorticity production in Hurricane Melissa

4.1 Introduction

The presence of inertial instability in tropical cyclone (TC) outflow has been considered since at least the mid-20th century (Kleinschmidt, 1951, Yanai, 1964, Ooyama, 1969). These regions fulfill the criterion

$$\eta_a f < 0, \tag{4.1}$$

a statement of gradient wind imbalance, where the absolute vorticity (η_a) is the sum of relative (η) and planetary (f) vorticities (for a simple treatment, see Cushman-Roisin and Beckers, 2011). Perturbed parcels accelerate from their initial locations (radially outward in TCs, Ooyama, 1987), and can manifest as distinct, high-velocity outflow corridors (Black and Anthes, 1971, Anthes, 1972). These regions are characterized by anomalously weak η_a such that the rotational tendency associated with divergent outflow is small, the deformation radius is large, and mass is easily evacuated from convective regions. These are important controls on overturning circulations (Emanuel, 1979), and the role of inertial stability (or lack thereof) is thought to feed back onto TC development (e.g. Rappin et al., 2011, Li et al., 2023, Jiang and Wang, 2025).

Recently, there has been renewed interest regarding interactions between inertially unstable outflow and the mid-latitude jet streams (e.g. Rowe and Hitchman, 2016, Prince and Evans, 2022), with particular concern regarding degradation of predictive skill in the downstream environment (Lojko et al., 2022). Much of this broader conversation occurs through the potential vorticity (PV) framework, the PV being defined in Cartesian coordinates

$$P = \rho^{-1} \boldsymbol{\eta}_a \cdot \nabla\theta, \tag{4.2}$$

where ρ is the density, $\boldsymbol{\eta}_a$ is the absolute vorticity vector, and $\nabla\theta$ the potential temperature gradient. Given the relative weakness of tropical temperature gradients (Sobel et al., 2001), Eq. (4.2) is well approximated by only its vertical component,

$$P \simeq \rho^{-1} \eta_a \frac{\partial\theta}{\partial z}. \tag{4.3}$$

In the statically stable upper-troposphere, Eq. (4.1) can be rewritten

$$Pf < 0, \tag{4.4}$$

such that regions of negative PV (NPV) are typically inertially unstable in the Northern Hemisphere.

It can be shown that both Eq. (4.3) & (4.4) also hold in higher latitudes where the deformation radius is substantially smaller (Holton and Hakim, 2013, see their pg. 106).

Thus, the PV perspective is also used in a growing body of literature regarding upper-level inertial instability arising due to diabatic heating in the warm conveyor-belt airstream (WCB) of extra-tropical cyclones (e.g. Oertel et al., 2020). Harvey et al. (2020) isolated the production mechanism for upper-level NPV in WCBs, with Prince and Evans (2022) extending similar methodology to the extra-tropical transition (ET) of Hurricane Irma (a WCB develops during robust ET). These analyses indicate that filamentary, near-synoptic-scale NPV features can form along the anticyclonic flank of the upper-level jet stream; an organized result arising from diabatic heating in the presence of vertical shear and, via thermal wind balance, baroclinicity.

It is possible that the introduction of ambient vertical shear during a TC-trough interaction is responsible for the apparent organization of NPV production in ET events (e.g. Prince and Evans, 2022, see their Fig. 9). Indeed, these amalgamated features are remarkably disparate from the high-amplitude, convective-scale NPV anomalies observed in high-resolution TC forecasts by (Rowe and Hitchman, 2026, see their Fig. 3). Their observations indicate that small-scale deviations from moist neutrality in strong TCs may be responsible for the observed upper-level NPV features (i.e. incongruity between angular momentum and moist entropy surfaces, Emanuel, 1986). While acknowledging this possibility, we hypothesize that the ambient shear associated with the TC primary circulation is sufficient such that organized, TC-scale NPV production can occur without trough interaction *or* violations of axisymmetry (e.g. convective bursts). This hypothesis is evaluated in high-resolution simulations of Hurricane Melissa (October 2025) at both tropical storm and cyclone development stages. The remainder of this article is

organized as follows. Chapter 4.2 introduces the contemporary PV perspective on NPV development and briefly reviews application to the WCB airstream. Chapter 4.3 applies this PV perspective to an idealized TC development. Chapter 4.4 describes our analysis of axisymmetric NPV production in high-resolution simulations of Hurricane Melissa at two strongly disparate development stages. A discussion of conclusions, implications, limitations, and recommendations for future work is contained in a final Chapter 4.5.

4.2 Contemporary PV perspectives on NPV development

4.2.1 PV and its tendency equation

A diabatic process responsible for the production of upper-tropospheric NPV structures has been identified in association with the warm-conveyor belt (WCB) airstream characteristic of extra-tropical cyclones (Harvey et al., 2020). This corridor of warm, moist air ascends from the cyclone's warm sector into the upper troposphere where, upon turning anticyclonically, it joins the upper-level jet stream (Carlson, 1980). Some of this ascent is simply quasi-Lagrangian, isentropic upglide, though along-flow diabatic heating produces cross-isentropic ascent such that outflow reaches high values of potential temperature (θ) found on the anticyclonic side of the upper-level jet. Harvey et al. (2020) and Oertel et al. (2021) demonstrate that sub-synoptic heating can be responsible for observed NPV structures embedded within the WCB so long as there is sufficient ambient shear. Let us consider their discovery using a breakdown of the PV tendency equation described by

Haynes and McIntyre (1987), which was later applied to WCBs and the NPV problem by Martínez-Alvarado et al. (2016) and Harvey et al. (2020), respectively.

The Lagrangian PV tendency is given

$$\rho \frac{dP}{dt} = \boldsymbol{\eta}_a \cdot \nabla \dot{\theta} - \nabla \times \boldsymbol{F} \cdot \nabla \theta \tag{4.5}$$

where $\boldsymbol{F}$ is friction and $\dot{\theta}$ is the flow-following potential temperature tendency (i.e. diabatic heating). Since we are concerned with processes that produce sign changes in P, recall that friction only acts to retard motion and can not produce inertially unstable conditions. Further, since much of the subsequent application will occur in the free troposphere, this term is assumed to be small. We can re-write the frictionless Eq. (4.5) in flux form,

$$\rho \frac{dP}{dt} = \nabla \cdot (\boldsymbol{\eta}_a \dot{\theta}), \tag{4.6}$$

since $\boldsymbol{\eta}_a$ is non-divergent. From Eq. (4.6) we conclude that 1) the PV is conserved following frictionless, adiabatic flows and 2) the diabatic PV tendency is associated with

gradients of heating in the presence of vorticity. In flux form, the tendency is appropriately described by the divergence of a flux oriented along vortex lines.

Another important property of PV is that of the quantity's invertibility. In other words, given the distribution of PV, boundary conditions and a suitable balance constraint (e.g. geostrophy or gradient balance), the balanced motion and thermal fields are known (e.g. Hoskins et al., 1985). Many quantitative applications of this technique exist in the literature, but for the purposes of developing conceptual models it is sufficient to qualitatively invert the PV distribution to gain insight. For example, consider a statically stable flow wherein the absolute vorticity vector is dominated by its vertical component, η_a. This implies that the horizontal vorticity is relatively weak, Eq. (4.3) holds, and Eq. (4.6) reduces to

$$\frac{dP}{dt} \simeq \rho^{-1}\eta_a \frac{\partial \dot{\theta}}{\partial z}, \tag{4.7}$$

such that the PV tendency is directly related to P via η_a. When Eq. (4.7) holds, as $P \to 0$ so must η_a and the diabatic PV tendency vanishes. In order to diagnose the production of inertial instability, we must consider the role of horizontal PV redistribution in the three-dimensional diabatic PV tendency [Eq. (4.6)].

4.2.2 Partitioning $\boldsymbol{\eta}$ along and across local isentropes

In order to rigorously isolate the process responsible for sign changes in PV, we first partition the absolute vorticity into components oriented along and across local isentropes,

$$\boldsymbol{\eta}_{\parallel} = \hat{n} \times (\boldsymbol{\eta_a} \times \hat{n}) \tag{4.8}$$

$$\boldsymbol{\eta}_{\perp} = (\boldsymbol{\eta_a} \cdot \hat{n})\hat{n}, \tag{4.9}$$

respectively, where $\hat{n} = \nabla\theta/|\nabla\theta|$. Their sum is the full, three-dimensional absolute vorticity and the PV may be re-written, in its entirety,

$$P = \rho^{-1}\boldsymbol{\eta}_{\perp} \cdot \nabla\theta \tag{4.10}$$

since $\boldsymbol{\eta}_{\parallel}$ does not project onto $\nabla\theta$ by definition. By substituting Eqs. (4.8) & (4.9) for $\boldsymbol{\eta}_a$, Eq. (4.6) can also be re-written as

$$\rho\frac{dP}{dt} = \nabla \cdot (\boldsymbol{\eta}_{\perp}\dot{\theta}) + \nabla \cdot (\boldsymbol{\eta}_{\parallel}\dot{\theta}). \tag{4.11}$$

Since the PV is directly related to $\boldsymbol{\eta}_\perp$ [see Eq. (4.10)], as $P \to 0$, so must the first term on the rhs of Eq. (4.11). This limitation is not extended to the second term; the PV is only indirectly related to $\boldsymbol{\eta}_\parallel$ when thermal wind balance applies. Convergence of $\boldsymbol{\eta}_\parallel \dot{\theta}$ is the sole diabatic mechanism capable of producing inertially unstable conditions.

In an environment with no horizontal temperature gradient, $\boldsymbol{\eta}_\parallel$ and $\boldsymbol{\eta}_\perp$ lie in the horizontal and vertical planes, respectively (i.e. this partitioning is unnecessary). As the slope of isentropes increase, however, each partition begins to acquire both vertical and horizontal components. That said, for a potential temperature gradient lying only in the x and z directions, its angle relative to the z-axis is given by

$$\phi = \arctan\left(\frac{\partial\theta}{\partial x}/\frac{\partial\theta}{\partial z}\right). \tag{4.12}$$

Assuming a vertical potential temperature gradient of 4 K km^{-1}, even if the horizontal temperature contrast approaches 1 K km^{-1}, $\boldsymbol{\eta}_\perp$ will only depart from η_a by about 15 degrees. A horizontal temperature gradient of that size is unreasonable for typical mid-latitude frontal regions, and the contrast associated with a TC warm core is more appropriately scaled at 0.04 K km^{-1}. This would be associated with a departure of only about 1 degree, an indication that isentropes rarely, if ever, slope such that $\boldsymbol{\eta}_\parallel$ acquires a meaningful amount of η_a. Thus, while the first and second terms are sometimes referred to as the "advective" and "non-advective" PV fluxes [a reference to the impermeability

theorem of Haynes and McIntyre (1987)], they can be thought of as terms describing vertical and horizontal diabatic PV redistribution without much loss of insight. In other words, the first and second rhs terms in Eq. (4.11) are similar to their counterparts in the formulation

$$\frac{dP}{dt} = \rho^{-1} \left[\eta_a \frac{\partial \dot{\theta}}{\partial z} + \nabla_h \cdot (\boldsymbol{\eta}_h \dot{\theta}) \right], \tag{4.13}$$

where the subscript h indicates only horizontal components are retained.

4.2.3 Application to the WCB environment

Consider the case of an idealized WCB where strong diabatic heating occurs in the sheared region equatorward of, and immediately beneath, the mid-latitude jet stream (Fig. 4.1). Vertical shear associated with the overlying jet is scaled by latent heating for a non-zero $\boldsymbol{\eta}_{\parallel} \dot{\theta}$ which points up the isentropic slope (Fig. 4.1b). Flux convergence occurs immediately equatorward of the jet core, a region already characterized by low PV and anticyclonic relative vorticity. Provided time and sufficiently weak values of initial PV, this is a likely region for the appearance of NPV, anticyclonic absolute vorticity, and, thus, inertial instability. This action increases the horizontal PV gradient and balanced wind speed near the jet core, thus reinforcing along-isentrope PV re-arrangement via its dependence on vertical shear. This conceptual model closely follows that of Harvey et al. (2020, see

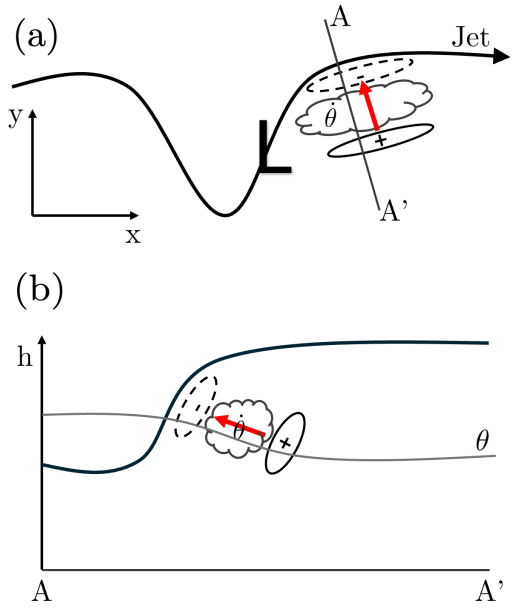

FIGURE 4.1: (a) An upper-level isohypse representative of the jet stream (thick black, denoted "Jet", and with an arrow-head indicating the flow direction), the location of a low-level extra-tropical cyclone (L), a region of WCB diabatic heating (squiggly grey denoted "$\dot{\theta}$"), the corresponding flux $\boldsymbol{\eta}_{\parallel}\dot{\theta}$ (red arrow), and its convergence/divergence (thin black dashed/solid, respectively). (b) The dynamic tropopause (thick black), an exemplary isentrope (solid grey denoted "θ"), and, as in (a), a region of WCB diabatic heating, the flux $\boldsymbol{\eta}_{\parallel}\dot{\theta}$ and its convergence for the cross section A-A'. This conceptual model closely follows that of Harvey et al. (2020, see their Fig. 5) and Oertel et al. (2020, see their Fig. 13).

their Fig. 5) and Oertel et al. (2020, see their Fig. 13), and is thought to explain the seeming ubiquity of NPV-jet interactions observed downstream of extra-tropical cyclones (Lojko et al., 2024).

4.3 NPV production by the sheared primary circulation in developing TCs

4.3.1 Why not consider all convectively-coupled tropical disturbances?

Given the weakness of tropical temperature gradients, horizontal advective terms can be discarded in the thermodynamic equation [i.e. the weak temperature gradient (WTG)], and a first-order balance arises between diabatic heating and adiabatic cooling (Sobel et al., 2001). This remains a good approximation within many transient, convectively-coupled disturbances as residual heating (cooling) from, for example, convection (radiation) is spread to the surrounding environment in the form of gravity waves (Adames, 2022). Thus, despite diabatic processes, isentropes tend to remain relatively flat in the horizontal (i.e. the environment is not baroclinic).

When lacking large-scale baroclinicity, we anticipate 1) weak vertical shear, 2) flat isentropes such that the $\boldsymbol{\eta_a}$ is effectively described only by the cross-isentrope component ($\boldsymbol{\eta}_\perp$), and 3) that $\boldsymbol{\eta}_\parallel$ arises principally due to convective-scale gradients in vertical motion. Thus, while any number of convectively-coupled waves potentially produce small-scale NPV features associated with differential vertical motion (in the presence of inhomogeneous heating, Conzemius and Montgomery, 2009), NPV production associated with vertical shear is thought to be unique to phenomena which specifically violate WTG. One

which does so spectacularly is the TC, whose rotational primary circulation traps gravity wave energy in a developing warm core. Although the TC circulation is in gradient, rather than geostrophic balance, a warm core still demands vertical shear following the thermal wind equation for an axisymmetric flow in hydrostatic and gradient wind balance,

$$\left(f + \frac{2v}{r}\right)\frac{\partial v}{\partial z} = R\left(\frac{\partial \ln p}{\partial r}\frac{\partial T}{\partial z} - \frac{\partial \ln p}{\partial z}\frac{\partial T}{\partial r}\right), \tag{4.14}$$

where v is the tangential wind, T the temperature, R the ideal gas constant, and r the radius (Yanai, 1964).

Similar to how the Rossby number is used to determine whether a given flow is governed by the QG approximation, the WTG criterion for eddy systems is given

$$N_w = v^2/c^2, \tag{4.15}$$

where v is the tangential wind and c is the gravity wave phase speed (Adames, 2022). This measures the importance of inertial to gravitational forces and is the squared Froude number. For tropical depressions whose horizontal winds and warm cores remain relatively weak, $N_w \sim 0.1$ and their dynamics/thermodynamics are governed principally through

the basic equations under the WTG approximation (isentropes remain "flat"). For TCs, where v can reach well over 50 m s^{-1}, N_w approaches unity and the WTG approximation becomes poor (isentropes slope non-negligibly). This breakdown is intimately linked to the production of a warm core, and is an indication that the role of vertical shear (through $\boldsymbol{\eta}_{\parallel}$) should be considered in Eq. (4.11).

TABLE 4.1: Approximate scaling values (columns) used to estimate the size of anticipated vertical and horizontal PV tendencies and changes associated with tropical depressions and cyclones. One can multiply the product of the first three columns by 1×10^6, the conversion factor to PVU, in order to produce the PV tendency in the fourth column. We have implied a value of $\rho = 1$ kg m^{-3}.

Phenomenon	$\boldsymbol{\eta}$ (s^{-1})	$\Delta\dot{\theta}$ (K s^{-1})	∇^{-1} (m^{-1})	$\frac{dP}{dt}$ (PVU s^{-1})
Depression (vertical)	1×10^{-4}	1×10^{-3}	2×10^{-4}	2×10^{-5}
Depression (horizontal)	1×10^{-3}	1×10^{-3}	5×10^{-6}	5×10^{-6}
Cyclone (vertical)	1×10^{-3}	3×10^{-3}	2×10^{-4}	6×10^{-4}
Cyclone (horizontal)	3×10^{-3}	3×10^{-3}	4×10^{-5}	4×10^{-4}
Conv. Burst (horizontal)	1×10^{-3}	1×10^{-3}	2×10^{-4}	2×10^{-4}

4.3.2 PV budget scaling for tropical depressions and cyclones

To further illustrate the hypothesis that organized, cyclone-scale NPV production can not occur until after TC development, we provide approximate scaling values for diabatic PV tendencies in a developing TC. Recall that, even after the development of a TC warm core, isentropes rarely slope so strongly that $\boldsymbol{\eta}_{\perp}$ departs substantially from η_a [see Eq. (4.12) and the surrounding discussion]. The rhs PV tendency terms in Eq. (4.11) & (4.13) thus scale like

$$\zeta_a \frac{\Delta\dot{\theta}}{\Delta z} : \frac{\Delta u}{\Delta z}\frac{\Delta\dot{\theta}}{\Delta r} \tag{4.16}$$

for an axisymmetric TC (with radius r) and represent vertical and horizontal diabatic PV redistribution, respectively. We will incorporate horizontal gradients in vertical motion later in this section.

Approximate scaling values are provided in Table 4.1 for both an idealized tropical depression (TD) and TC. Prior to the development of a TD, the basic state vertical shear is weak such that horizontal redistribution can not become a leading order term (not shown). Once the lower (upper) tropospheric positive (negative) PV anomaly associated with a TD-type wave forms, weak shear develops and the horizontal redistribution term becomes non-negligible, though second order. As these PV anomalies grow in size, the vertical shear increases and horizontal and vertical redistribution become almost comparable. That said, we anticipate that horizontal redistribution will remain weaker than its counterpart, especially near the lifting condensation level where η_a and $\partial\dot{\theta}/\partial z$ are both very large.

Thus far, it has been assumed that convection and the resulting circulation is axisymmetric. If this were not the case, for example, due to convective bursts within the TC eyewall, it is possible that the horizontal PV redistribution term will acquire an important component associated with horizontal gradients in vertical motion which scales like

$$\frac{\Delta\omega}{\Delta\mathcal{L}}\frac{\Delta\dot{\theta}}{\Delta\mathcal{L}}, \tag{4.17}$$

where $\mathcal{L}$ is the horizontal scale of the convective burst and $\Delta\dot{\theta}$ is the difference between the latent heat release in the burst and the outlying convection. We have included an approximate scaling for this possibility in Table 4.1, the size of which strongly indicates that convective bursts, spiral rainbands, and other sources of asymmetry are important features in determining the redistribution of PV in both TDs and TCs. This term, however, does not clearly dwarf its counterparts in TCs such that there is a distinct possibility that NPV production occurs both in the organized, axisymmetric eyewall updraft *and* in asymmetric features. The resultant PV distributions will be markedly different, the former associated with a persistent annulus structure surrounding the TC, the latter associated with sporadic, high-amplitude PV dipoles like those described by Rowe and Hitchman (2026).

4.3.3 Diabatic PV tendencies in an idealized, developing TC

In order to clearly illustrate how the along-flow diabatic PV tendency changes during TC development, we have included a conceptual model of PV structure and diabatic PV tendency for both a TD and TC (Fig. 4.2). For the TD-like cyclone, we assume that WTG holds such that the vertical motion distribution is given by the diabatic heating (solid black lines in Fig. 4.2a) and isentropes remain flat in the horizontal (solid grey lines

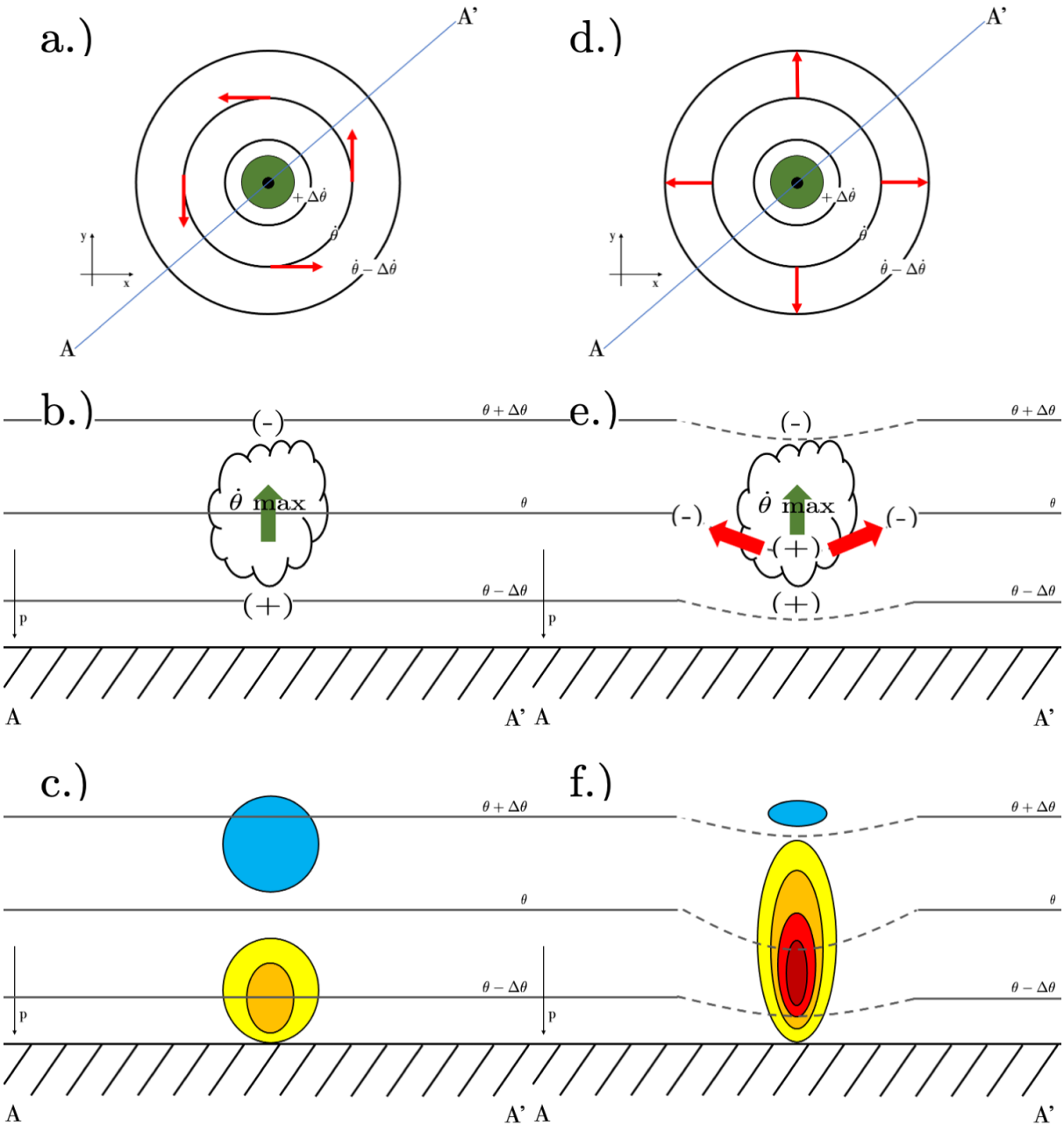

FIGURE 4.2: (a) Diabatic heating (solid black) and the fluxes $\boldsymbol{\eta}_{\perp}\dot{\theta}$ (green arrowhead) and $\boldsymbol{\eta}_{\parallel}\dot{\theta}$ (red arrows) for an idealized, axisymmetric tropical depression in quasi-steady state. A steady-state assumption implies that WTG holds and the distribution of vertical motion is given by the heating. (b) As in (a) except with isentropes (solid grey) and the diabatic heating maximum (cloud outline) and PV tendencies associated with convergence/divergence of $\boldsymbol{\eta_a}\dot{\theta}$ (plus/minus) along the cross section from A-A'. (c) As in (b) except with low and high PV (blues, yellows/reds, respectively). (d) As in (a) except for a TC. (e) as in (b) except for a warm core has developed (dashed grey isentropes). (f) As in (c) except for a TC with a warm core.

in Fig. 4.2b). While a non-zero $\boldsymbol{\eta}_{\parallel}$ exists due to the radial gradient in vertical motion (red arrows in Fig. 4.2a), note that these vectors are purely rotational and the dominant PV tendency is clearly vertical redistribution associated with a mid-tropospheric diabatic heating maximum (green arrows in Fig. 4.2a & b). In time, this is associated with the generation of lower and upper-level positive and negative PV anomalies, respectively, and the development of commensurate shear (Fig. 4.2c).

As the low-level primary circulation develops, WTG breaks down and diabatic heating is no longer entirely balanced by adiabatic cooling. A warm core develops (dashed grey contours in Fig. 4.2e), and $\boldsymbol{\eta}_{\parallel}\dot{\theta}$ acquires a divergent component due to vertical shear (red arrows in Fig. 4.2d). Divergence of this flux radially inward of the eyewall is associated with a positive PV tendency which, in addition to vertical advection of positive PV, contributes to the development of the PV "tower" or "cigar" characteristic of strong TCs (Fig. 4.2f). While there is still robust upper-level PV erosion due to vertical diabatic PV re-arrangement, this is thought to be partially offset by vertical PV advection such that the upper-level anticyclone attributed to TC outflow is found in the broader, large-scale outflow environment (not shown).

The transition from TD to TC is non-linear, both because of non-linearity in the first term on the rhs of Eq. (4.6), and because the second term on the rhs of Eq. (4.6) is emergent and acts to strengthen the radial PV gradient over a deep layer (Fig. 4.2e). This is also the only term capable of producing NPV in this axisymmetric framework, and it should be clear that $\boldsymbol{\eta}_{\parallel}\dot{\theta}$ is convergent (divergent) only on the radially-outward (inward)

fringe of the heating maximum (Fig. 4.2e). While the notion that this narrow portion of TC updraft can consistently produce NPV outflow is potentially at odds with the slantwise moist neutral assumption of (Emanuel, 1986, outflow PV should be essentially zero everywhere), it is consistent with observations of TC outflow consisting of a mix of both positive and negative PV air (Black and Anthes, 1971). The subsequent analysis focuses on illustrating this perspective in the composite structure of Hurricane Melissa at different development stages.

4.4 Analysis of Hurricane Melissa

4.4.1 MPAS simulations → composite cross sections

For this analysis, we have chosen Hurricane Melissa (October 2025, hereafter Melissa), a strong TC which reached maturity while nearly quasi-stationary immediately south of Jamaica (Fig. 4.3). Two 12-hour simulations were performed using the Model for Prediction Across Scales (MPAS, Skamarock et al., 2012) beginning at 12Z 21 Oct and 00Z 27 Oct 2025 when Melissa was a tropical storm and category 4 hurricane, respectively (Fig. 4.3). These simulations were performed using a global 60-3 km mesh with 55 vertical levels and 30-minute output. The mesh refinement region was centered over the low-level cyclone at each initialization such that the horizontal resolution is approximately 3 km everywhere within 8° of the storm center. The refinement reduces to 9 km resolution at a 16° radius such that the vast majority of the TC and its broader outflow region is captured at resolutions < 10 km. The simulation was initialized using the 0.25° final operational

global analysis available from the National Center for Environmental Prediction (i.e. NCEP GDAS/FNL) data without sea-surface temperature updates.

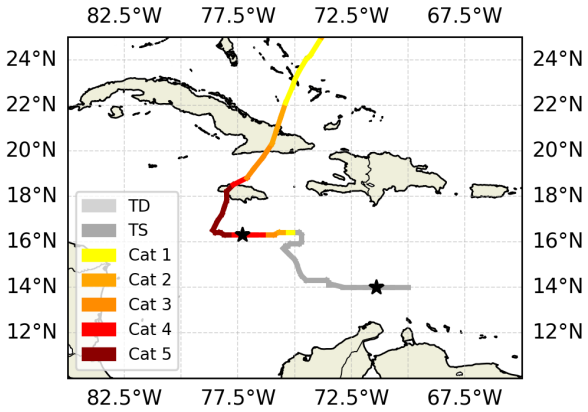

FIGURE 4.3: Hurricane Melissa's track starting 00Z 21 Oct 2025 (IBTrACS). Black stars refer to Melissa's location at 12Z 21 Oct and 00Z 27 Oct, the latter being further north.

The resulting MPAS output was converted to a 0.1° latitude-longitude grid and interpolated to height surfaces. A simple cyclone tracking algorithm was developed to identify the cyclone center as the local maximum in PV at 3 km. Provided the broader cyclonic circulation has several embedded PV maxima at the native and interpolated resolutions, a 9-point spatial smoother was applied 20 times. By subsetting data over the broader storm system, the tracking algorithm simply records the position of the domain-maximum PV in the smoothed data at each 30-minute forecast period. This algorithm is relatively robust to choice of spatial smoothing and vertical layer (when employed in the lower troposphere), and was validated manually using 3 km PV analyses (not shown). The resulting cyclone locations were used to systematically create 36 radial cross sections extending 600 km from the storm center at each forecast period. Tangential (v) and radial

winds (u) were calculated as components of meridional and zonal winds which project onto each cross section's tangential and normal directions.

An azimuthally- and time-averaged radial cross section was subsequently created for each MPAS simulation (i.e. a composite cross section). This data was mirrored across $r = 0$ to produce visualizations whose perspective is consistent with Fig. 4.2b, c, e & f. A single pass of a 1-dimensional Gaussian-bell smoother with a 12 km kernel was applied to potential temperature (MPAS variable *theta*) and latent heating output from the MPAS microphysics scheme (MPAS variable *dtheta_dt_mp*). This helps reduce downstream errors introduced by a slight discontinuity in potential temperature and heating fields at $r = 0$ km, while minding the sensitivity of narrow features to horizontal smoothing. The effect of asymmetrical environmental conditions in the storm environment was tested by sub-selecting portions of the cyclone (e.g. only compositing cross sections which extend to the NW). Despite clear indications of convective asymmetry in the storm environment (not shown), the subsequent discussion remains unchanged regardless of choice, thus we choose to analyze the full cyclone environment rather than an arbitrary sub-selection.

4.4.2 Choice of PV tendency

For each composite, the PV tendency arising from latent heating can be written

$$\rho \frac{dP}{dt} \simeq \nabla \cdot \left(\boldsymbol{\eta}_{\perp} \dot{\theta}_{\mathrm{mp}} + \boldsymbol{\eta}_{\parallel} \dot{\theta}_{\mathrm{mp}} \right) \tag{4.18}$$

$$\simeq \eta_a \frac{\partial \dot{\theta}_{\mathrm{mp}}}{\partial z} + \frac{\partial v}{\partial z} \frac{\partial \dot{\theta}_{\mathrm{mp}}}{\partial r}, \tag{4.19}$$

where $\dot{\theta}_{\mathrm{mp}}$ is the latent heating from the MPAS microphysics scheme, z is the height, r is the radius, and v is the tangential wind. We write Eq. (4.18) and (4.19) as approximate equivalencies since each rhs neglects the diabatic PV tendency associated with radiation, friction and other diabatic processes. Specifically, we have dropped the component of diabatic PV re-arrangement associated with horizontal gradients in vertical motion in Eq. (4.19), as it cannot be assessed using this methodology.

$\boldsymbol{\eta}_{\parallel}$ and $\boldsymbol{\eta}_{\perp}$ were calculated following Eqs. (4.8) & (4.9), with η_a calculated from composited model-output vorticity and $\partial v/\partial z$ calculated from the vertical gradient of the composite tangential wind. It was hypothesized earlier that an individual equivalence assumption between rhs terms in Eqs. (4.18) & (4.19) is relatively strong for most geophysical applications. As further evidence regarding the strength of that assumption, note that the angle between $\nabla\theta$ and the vertical axis [see Eq. (4.12)] maximizes at 2° along the flank of the upper-tropospheric warm core in the 27 Oct composite (Fig. 4.4). The difference between the across-isentrope and absolute vorticities maximizes on the order of 1 $\times 10^{-4}$ s^{-1} and is typically on the order of 1 $\times 10^{-5}$ s^{-1}. This difference is small compared to the large-scale vertical shear and low-level relative vorticity on 27 Oct

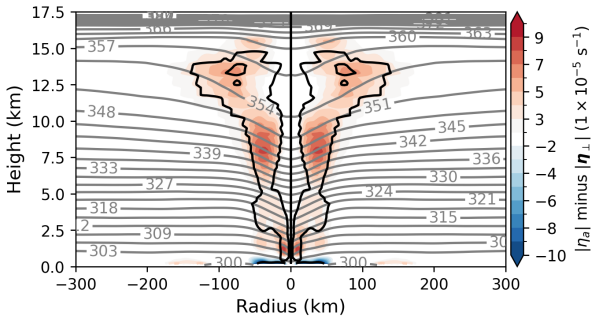

FIGURE 4.4: Isentropes (solid grey), the angle between $\nabla\theta$ and the vertical axis [i.e. Eq. (4.12), solid black every 1° beginning at 1°], and the difference between $|\boldsymbol{\eta}_\perp|$ and $|\eta_a|$ (shaded blues/reds every 1 $\times 10^{-5}$ s^{-1} beginning -2 and 2 $\times 10^{-5}$ s^{-1}, respectively.)

(Fig. 4.5c & d), though it is not entirely negligible in the middle-upper troposphere. It is for this reason that we consider the two terms in Eq. (4.18); they are easily calculable and rigorously isolate the mechanism responsible for NPV. For qualitative or operational analysis, however, one can consider Eq. (4.19) without loss of much insight.

4.4.3 Distribution of PV and its tendency

Between 21 and 27 Oct, there was a distinct transition from a small-scale, lower-tropospheric positive PV feature similar to our TD conceptual model (Fig. 4.2c) to a deep-tropospheric tower of high PV consistent with a robust TC (Fig. 4.6). In addition, the average location of the 2-PVU dynamic tropopause in the near-TC outflow region moved from approximately 366 K to 370 K, while the PV between 12.5–15 km lowered on average (Fig. 4.6). Of particular interest is an upper-tropospheric PV minimum appearing near 15 km height, 175 km radius in the 27 Oct composite (see yellow stars, Fig. 4.6b). This region is linked to the TC boundary layer via a narrow range of angular momentum contours from 1.6–2.1×10^{-6} m^2 s^{-1}. For an axisymmetric, steady-state TC this angular-momentum "slab"

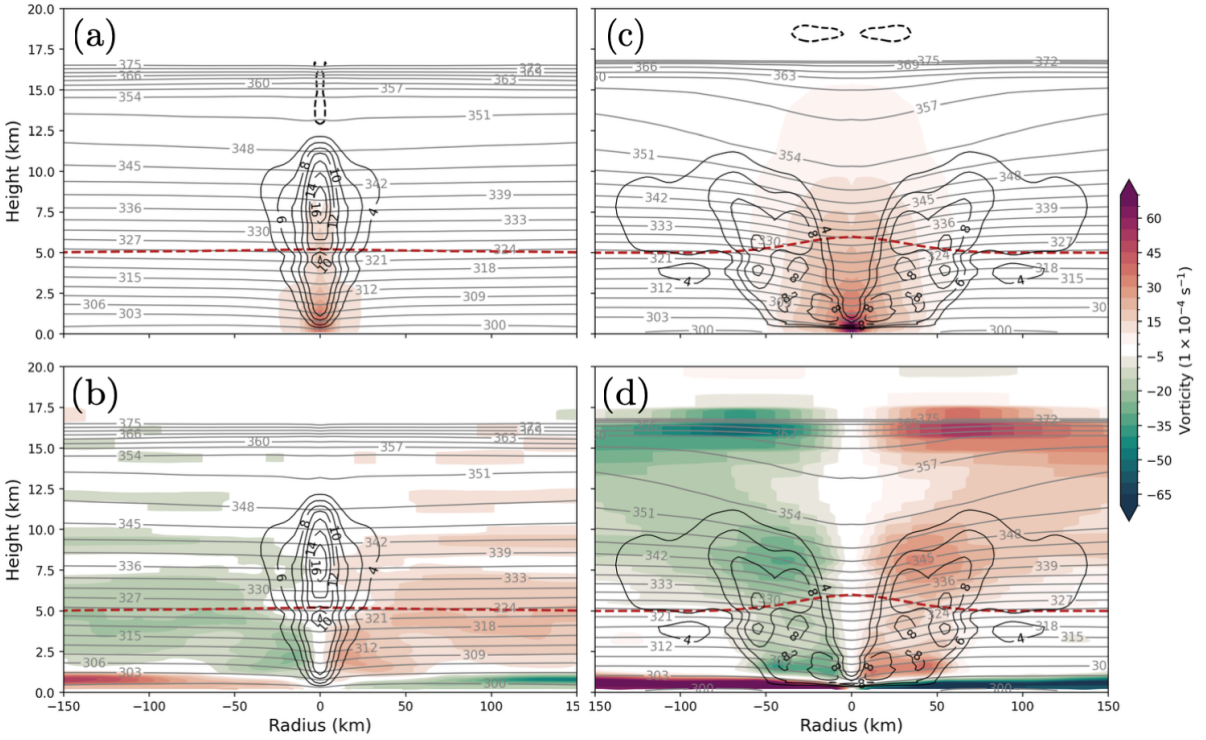

FIGURE 4.5: (a) Potential temperature (solid grey every 3 K until 375 K), latent heating from MPAS microphysics (solid black every 2 K hr^{-1} beginning at 4 K hr^{-1}, the 0° C isotherm (dashed red), absolute vorticity (shaded greens and reds every 5×10^{-4} s^{-1} extending from -5 and 5×10^{-4} s^{-1}, respectively), and the -1×10^{-5} s^{-1} absolute vorticity contour (dashed black) for the composite cross section of Melissa on 21 Oct 2025. (b) As in (a) except for the horizontal vorticity arising from the vertical shear of the tangential winds (shaded). (c) & (d) As in (a) and (b) except for the 27 Oct composite.

is almost equivalently the 360 K moist isentrope characteristic of eyewall convection (e.g. Emanuel, 1986). Assuming parcels take this approximate path from lower to upper troposphere (i.e. they conserve angular momentum and moist entropy), the along-flow PV tendency in this slab must be negative.

In addition to changes in the composite PV structure, there is a clear transition from a cyclone-centered diabatic heating maximum (again similar to our TD conceptual model, Fig. 4.2a) to a radially-outward-sloping eyewall structure (Fig. 4.5a & c). Strong vertical

vorticity occurs in the presence of vertically inhomogeneous heating such that vertical PV re-arrangement is dominant (order 1×10^{-4}–1×10^{-3} PVU s^{-1}) at both 21 and 27 Oct (see Fig. 4.5a & c). On 27 Oct, however, the cyclone center is characterized by a strong warm core (see Fig. 4.5d), with isentropes bowing downward consistent with vertical shear of the tangential wind via Eq. (4.14). This results in an important PV tendency associated with vertical shear in the presence of horizontally inhomogeneous heating (Fig. 4.7e). While this portion of PV tendency is also non-negligible on 21 Oct (Fig. 4.7b), a region of NPV production arises on 27 Oct confined within the same angular-momentum slab identified in Fig. 4.6b.

Although only sizing between -2 & -6×10^{-4} PVU s^{-1} (small compared to its counterpart), we can isolate the effect of the negative PV tendency pictured in Fig. 4.7e by calculating its cumulative effect on updraft parcels in this portion of the eyewall. For this analysis we begin by interpolating our composite cross section into coordinates oriented along and across a range of angular momentum contours from 1.6–2.1 $\times 10^{-6}$ m^2 s^{-1} (i.e. angular momentum - arc length coordinates). Thus, the slab-average PV tendency is known from lower to upper troposphere (i.e. at each arc-length interval). The along-updraft cumulative PV change is thus

$$\Delta P = \int_a^b \text{tendency} \times \Delta t \, \partial s \tag{4.20}$$

where a and b are positions along the slab arc-length, s, and

$$\Delta t = \frac{\Delta h}{w(s)} \tag{4.21}$$

where Δh is the along-arc-length height change and $w(s)$ is the slab-averaged vertical motion.

The outflow PV of angular-momentum-conserving updraft parcels can be approximated by summing an evaluation of Eq. (4.20) from 1.5–14 km arc-length, with initial values of PV found in this angular-momentum slab from 1–1.5 km. The average initial PV value is 3.21 PVU (see Fig. 4.8b for the full distribution), and, although the PV change is positive in the lower troposphere, the full cumulative change is negative (Fig. 4.8a). Any parcel with initial PV $<$ 2.94 PVU (approximately 39.5% of initial parcels) can acquire NPV (Fig. 4.8b). Since the PV gradient is oriented radially inward, these parcels are systematically found further radially outward than those which retain positive values of PV (Fig. 4.6b). The same technique applied to parcels initialized at higher levels (i.e. 2–2.5 km) is such that nearly 100% of them reach the outflow layer with NPV (not shown). This indicates a strong sensitivity to lower-tropospheric PV generation, and, thus, we attempt this analysis only on those parcels immediately above the boundary layer (a region where angular momentum conservation should not be assumed).

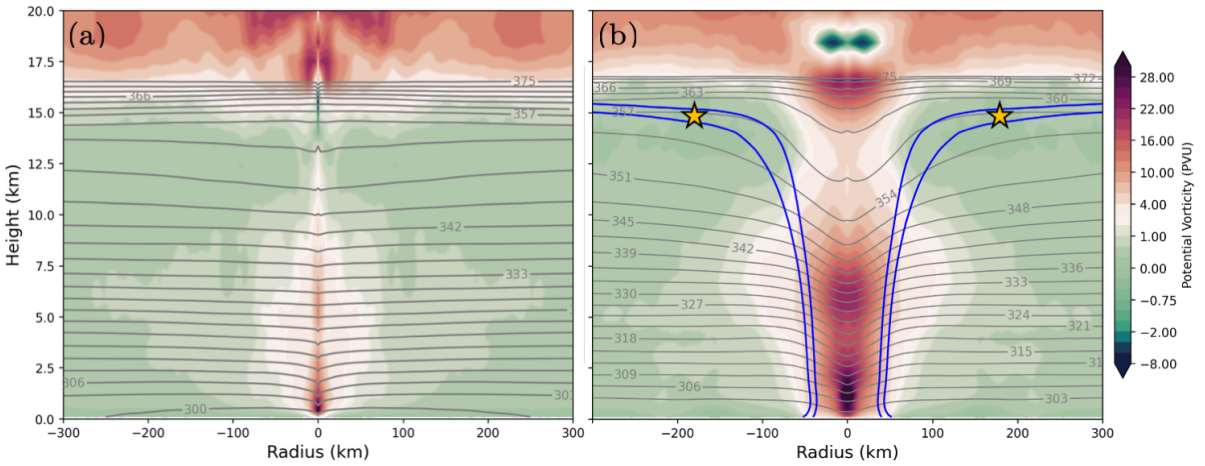

FIGURE 4.6: (a) Potential temperature (solid grey every 3 K until 375 K), and PV (shaded) for the 21 Oct composite cross section. (b) As in (a) except for the 27 Oct composite cross section and including the 1.6 & 2.1 $m^2\ s^{-1}$ angular momentum contours and the upper-tropospheric PV minimum (gold stars).

The negative PV tendency in this specific portion of eyewall is driven primarily by $\boldsymbol{\eta}_{\|}\dot{\theta}$ convergence (dash-dotted red line, Fig. 4.8a). The cumulative change associated with the full rhs of Eq. (4.18) is remarkably consistent with the composite PV along this angular momentum slab (comparing black vs. grey lines in Fig. 4.8a). Evaluation of Eq. (4.18) in this manner has effectively captured the along-flow PV tendency and its aggregate effect. We summarize this analysis by extending the azimuthal dimension and vertically-averaging composite conditions on 27 Oct from 3–9 km height (see Fig. 4.9) for a plan-view diagram similar to that in Fig. 4.2d. On the azimuth-radius plane, it is clear that $\boldsymbol{\eta}_{\|}\dot{\theta}$ (black vectors) point radially outward and maximize near the eyewall heating maximum (solid black). This flux is convergent (divergent) radially outward (inward) of the eyewall such that parcels rising through the outer fringes of the eyewall updraft can acquire NPV.

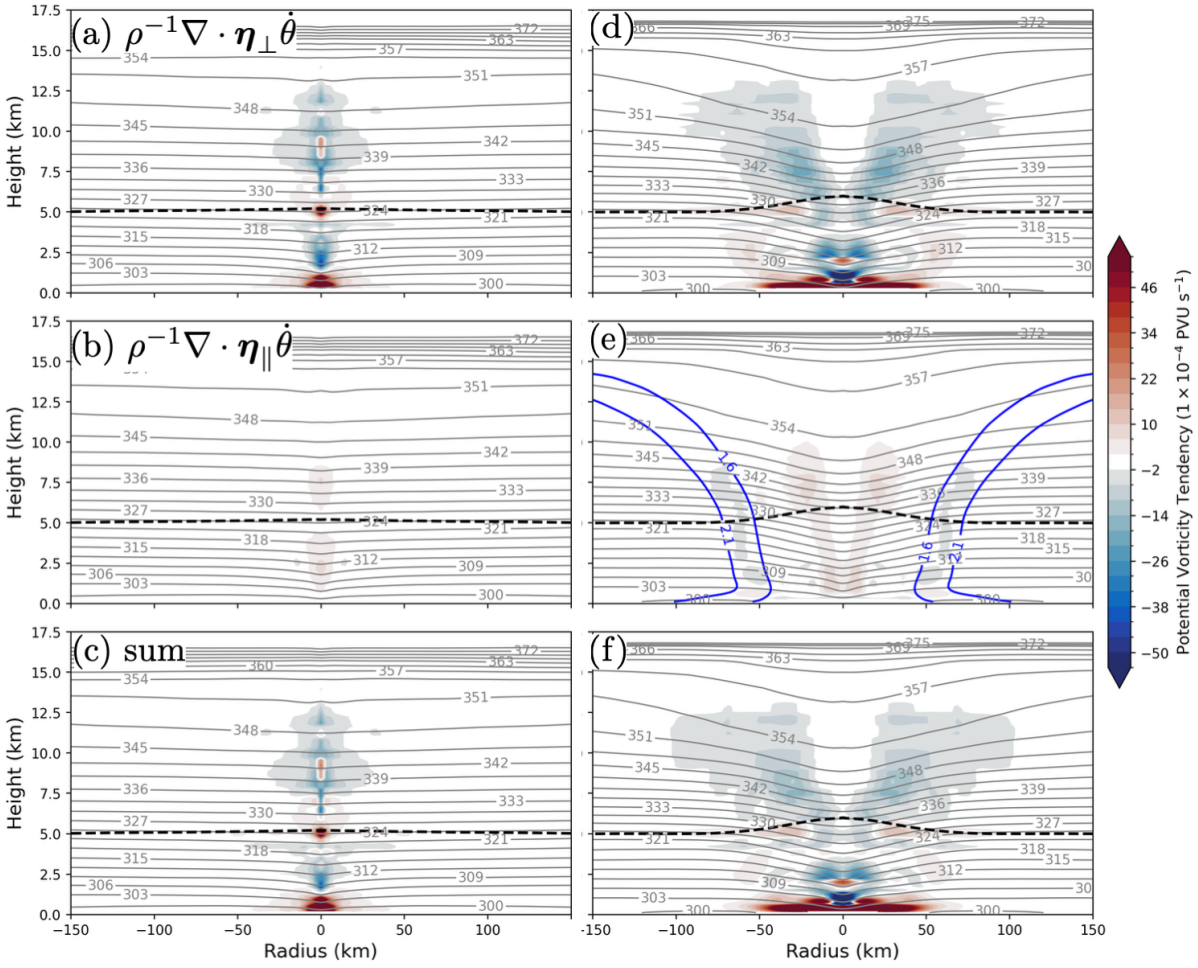

FIGURE 4.7: (a) Isentropes (solid grey every 3 K until 375 K), the PV tendency associated with $\boldsymbol{\eta}_\perp \dot{\theta}$ (shaded every 4×10^{-4} PVU s^{-1} from -2 and 2 PVU s^{-1}), the 0°-C isotherm (dashed black) for the 21 Oct composite. (b) As in (a) except for the PV tendency associated with $\boldsymbol{\eta}_\parallel \dot{\theta}$. (c) As in (a) except for the sum of the PV tendencies in (a) and (b). (d) as in (a) except for the 27 Oct composite. (e) As in (b) except for the 27 Oct composite and with the 1.6 and 2.1×10^{-6} m^2 s^{-1} angular momentum contours. (f) As in (c) except for the 27 Oct composite.

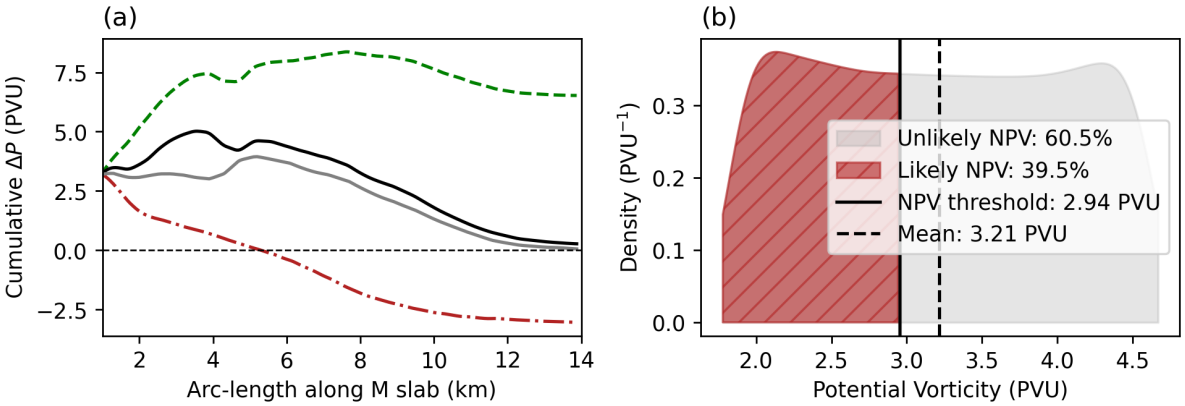

FIGURE 4.8: (a) The cumulative change in PV at each point along the 1.6–2.1$\times 10^{-6}$ m^2 s^{-1} angular momentum slab. That associated with the first, second and summed terms on the rhs of Eq. (4.18) are given by dashed green, dash-dotted red, and black lines, respectively. The angular-momentum-layer average PV is plotted in solid grey. (b) The frequency distribution of PV from 1–1.5 km arc-length for the angular momentum slab described in (a). The mean value of 3.21 PVU is given in dashed black, while the threshold initial value for a parcel to acquire NPV, 2.94 PVU is given in solid black. The 39.5 % (60.5%) of initial parcels lying to the left (right) of this threshold value are likely (unlikely) to acquire NPV.

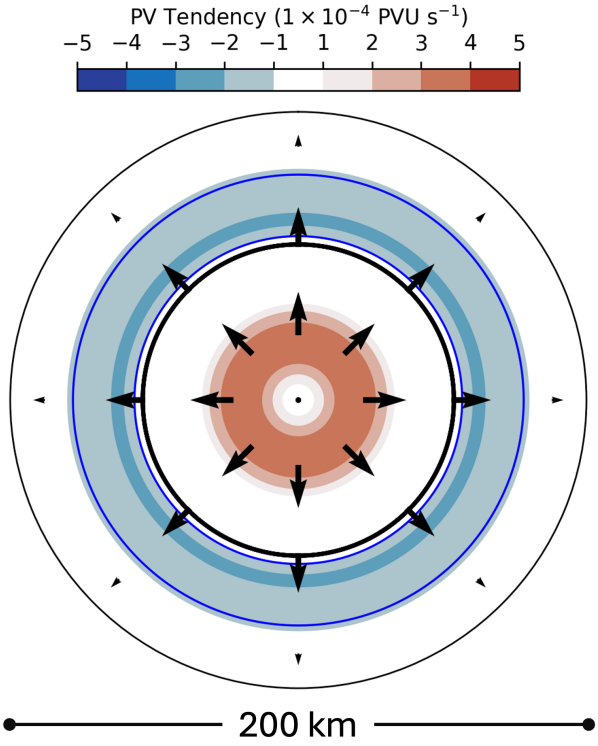

FIGURE 4.9: (a) The latent heating maximum (heavy solid black), the 1.6 & 2.1 $\times 10^{-6}$ m^2 s^{-1} angular momentum contours (solid blue), the flux $\boldsymbol{\eta}_{\|}\dot{\theta}$ (black arrows), and its divergence (shaded) averaged from 3–9 km and plotted on the azimuth-radius plane.

4.5 Discussion

4.5.1 Conclusions

While we entertain the notion that horizontal gradients in vertical motion can produce NPV features at the scale of an individual convective plume, a mechanism for NPV generation associated with the vertically-sheared TC primary circulation has been identified in axisymmetric composites of Hurricane Melissa. This mechanism can be thought of as horizontal PV re-arrangement arising from vertical shear in the presence of horizontally inhomogeneous heating, however, it is rigorously isolated as that associated with the flux $\boldsymbol{\eta}_{\parallel}\dot{\theta}$, where $\boldsymbol{\eta}_{\parallel}$ is the portion of vorticity that lies along isentropic surfaces. This flux maximizes near the eyewall heating maximum and converges (diverges) in a deep-tropospheric annulus radially outward (inward) of the eyewall heating maximum. Updraft parcels which ascend through the region of flux convergence can acquire NPV, especially those on the radially-outward fringes which begin ascent with lower initial PV. This leads to the conclusion, best summarized via Fig. 4.9, that organized, TC-scale NPV generation in Hurricane Melissa occurred in a very narrow region on the radially-outward fringes of the eyewall. This is in addition to NPV generation that is assumed to occur in association with asymmetries and convective bursts not captured by our methodology.

This specific production mechanism is thought to occur in all TCs due to its close relationship to the vertically sheared primary circulation (i.e. anticyclonic thermal vorticity). This shear is linked to a TC's warm core via gradient thermal wind balance [Eq. (4.14)],

thus, tropical disturbances without strong horizontal temperature gradients (i.e. those governed by the WTG approximation) are unlikely to feature this mechanism. Scale analysis (see Table 4.1) confirms the strength of our proposed conceptual model (see Fig. 4.2), which is exemplary of Hurricane Melissa at tropical storm and cyclone stages. That said, we emphasize that this analysis only isolates the portion of diabatic PV re-arrangement linked to vertical shear. It is likely that convective-scale PV re-arrangement occurs in individual convective complexes inherent to a variety of convectively-coupled tropical disturbances regardless of whether WTG applies. Such features were observed in the TC environment by Rowe and Hitchman (2026), thus we conclude that NPV production associated with along-isentrope heating gradients can occur both due to vertical shear and horizontal gradients in vertical motion. Whether or not these two mechanisms are fully separable is an important question (i.e. the eyewall is a convective structure prone to its own asymmetries). It is clear, however, that their relative importance changes upon the development of the TC warm core and its attendant shear (see Table 4.1).

4.5.2 Limitations and recommendations for future work

The principal limitation of the present study is its use of a single event at only two different development stages. It is possible that the distribution of PV tendencies may differ substantially between cases, and that two development "snapshots" are insufficient to fully garner insight. That said, the methodology presented here could be expanded to additional cases or development stages. To do so, however, one would need to consider alternate radial coordinates (e.g. one normalized by the radii of maximum tangential

winds) to ensure that the compositing processes did not smear the sought-after signal. This, in addition to the non-negligible computational cost of such high resolution MPAS simulations, motivated the chosen methodology. It is recommended that these steps are taken, however, to further confirm our deductions.

Another limitation of the present study is the use of relatively coarse vertical resolution (55 vertical levels) and prescribed horizontal and temporal resolutions. It is unclear how choice of temporal, horizontal or vertical resolution may impact our results. By using high-cost, high-spatial-resolution simulations, our intent was to reduce the role of convective parameterization in determining the PV tendency, even at the expense of a robust case catalog. In future work, however, it is worth considering the optimal vertical resolution which minimizes the role of convective parameterization in determining latent heating. Nonetheless, the resultant PV tendencies and distributions agree well with expectations (see Table 4.1 and Fig. 4.2). The analysis method chosen here does lose some of its explanatory power in that our chosen methodology can not evaluate the importance of TC asymmetries (i.e. convective bursts, spiral rainbands, etc) or deviations from steady state (i.e. rapid intensification, eyewall replacement, etc) in NPV production. Our scale analysis and model simulations indicate that these features are likely very important to both the distribution and size of PV tendencies, though our compositing technique disregards them by design.

One distinct utility of this PV framework is that, by extending the along and across-isentrope partitioning of the diabatic PV tendency to the TC environment, we are even

closer to a unified perspective which can be applied across a variety of weather phenomena. The need for unified perspectives has long been considered by the tropical cyclone community (Wayne et al., 1987, Reboita et al., 2026), with the PV perspective potentially bridging understanding across cyclone types (e.g. Emanuel et al., 2025). Anecdotally, the transition from cyclonic thermal vorticity (extra-tropical cyclone) to anticyclonic thermal vorticity (TC) has a direct effect on the distribution of $\boldsymbol{\eta}_{\parallel}$ such that the nature of NPV generation must change during tropical transition. The influence of ambient shear from an impending upper-level trough in extra-tropical transition events should also be considered. While the scope of this article is intended to remain narrow, it is clear that the employed PV perspective has robust applicability across a spectrum of weather phenomena with broad interest in the community. MPAS is a valuable tool at this intersection; it has robust, native support for PV budget analysis.

4.6 Concluding remarks

This manuscript represents an effort to explain production mechanisms for inertial instability events commonly observed in the subtropical and mid-latitude upper troposphere. Although the document begins with a modern, upper-tropospheric jet-following approach to a global inertial instability climatology, novelty is primarily offered through the identification of three mechanisms for inertial instability production. In chapter 2, we argue that tilting is the only *adiabatic* mechanisms capable of producing anticyclonic absolute vorticity. This mechanism manifests during strong upper-level jet developments when

northwesterly flow upstream of a developing trough axis is characterized by cold-air advection. This arrangement of isotherms and isohypses is such that strong descent occurs within the jet core. An anticyclonic vorticity tendency associated with tilting of the large-scale horizontal vorticity occurs on the equatorward side of the developing jet streak, a region already characterized by ambient anticyclonic shear vorticity. While this tilting mechanism is ubiquitous in adiabatically forced jet developments, instability should only be anticipated when the ambient shear vorticity is already relatively strong and the tilting mechanism is prolonged.

In addition to the aforementioned adiabatic mechanism, a *diabatic* mechanism for inertial instability production has been recently identified by Harvey et al. (2020). This phenomenon is favored in the region of large-scale ascent downstream of the trough axis and is described in section 4.2.3 via a decomposition of the full three-dimensional diabatic PV tendency. While this perspective is quite robust, we argue in chapter 3 that a relatively intuitive, complementary perspective arises by leveraging the approximate conservation of MPV for saturated flows in deep convection. In this framework, convective updrafts tap into convectively unstable air characterized by negative MPV. Saturated parcels retain a negative MPV value into the upper troposphere where, due to the lack of moisture, negative MPV manifests equivalently as negative dry PV. Since the upper troposphere is statically and convectively stable, both negative moist and dry PV represent inertial instability. While this MPV perspective is applied to TCs which interact with the mid-latitude westerly jets, it is thought that it has robust applicability in a number of weather phenomena like mesoscale convective systems and super-cell thunderstorms.

In our effort to describe inertial instability production during the extra-tropical transition of tropical cyclones (chapter 3), it became clear that TCs are often observed in association with large-scale regions of inertial instability even without interaction with the mid-latitude jet. As discussed in section 4.1, these inertially unstable regions have generally been attributed to deep convection, though without detailed mechanistic interrogation. One possible explanation is a natural extension of our proposed MPV theory to the axisymmetric TC environment. Interestingly, the MPV is thought to be conserved under the axisymmetric assumption even under sub-saturation since the moist entropy gradient does not project onto solenoids. This can be thought of as a momentary (on rapid intensification timescales) departure from the slantwise moist neutral assumption of Emanuel (1986). During rapid intensification, convective bursts, and other violations of the steady-state assumption, one should expect incongruities between moist isentropes and lines of constant angular momentum. These incongruities manifest as MPV anomalies (some of which have a negative sign) which convect into the upper troposphere as the TC returns to steady state.

In chapter 4, however, we take the dry Ertel's PV perspective outlined in Harvey et al. (2020) and apply it to the TC environment. In the early stages of TC genesis (i.e. tropical storm/depression stage) the primary sink/source of anomalous PV is vertical redistribution associated with mid-tropospheric diabatic heating. As the lower-tropospheric cyclonic circulations develops, however, the deformation radius shrinks and latent heating is no longer efficiently spread to the outlying environment via gravity waves. A warm core develops and, via thermal wind balance, so does vertical shear. This manifests in

an oft-neglected diabatic PV flux which is convergent/divergent in the along-isentrope (quasi-horizontal) plane. Anticyclonic thermal vorticity consistent with a cyclonic primary circulation which decays with height demands that PV is concentrated within the high-PV "tower" characteristic of a robust TC. PV erosion occurs on the radially-outward fringe of the eyewall heating maxima over a substantial depth in the middle troposphere. Since the PV gradient points radially inward, low-PV parcels on the outward fringes of the NPV tendency are those most likely to acquire NPV in their approach to the upper troposphere.

Provided the described horizontal PV redistribution serves primarily to strengthen the radial PV gradient in the TC, it is possible that NPV generation is directly linked to rapid intensification. Here, there is clear agreement between MPV and dry PV frameworks; the incongruence between moist isentropes and lines of constant angular momentum during rapid intensification is associated with NPV generation in the MPV perspective. That said, more work is required to fully describe agreement between these two perspectives. For example, the dry Ertel's PV perspective makes explicit the need for ambient vertical shear, whereas the MPV perspective does not. This would be a natural avenue in which to continue this work.

Appendix A

Supporting information for Ch. 1

A.1 A simple application: on the rarity of short-wave ridges

A quick look at the mid-latitude upper-level flow pattern typically reveals a planetary wavenumber of approximately 5–7 (i.e. six troughs and six ridges) in the cold-season hemisphere. An alternative evaluation is to count the number of mid-latitude storm systems in, say, a hemispheric visible or infrared satellite image. This is approximately consistent with the wavenumber of maximum growth in both Eady (1949) and Charney (1947) models for baroclinic instability. Embedded within this flow regime are short-wave length features which, due to their relatively intense vertical motion distributions, are of interest in the forecasting of sub-synoptic precipitation events (e.g. Beckley et al., 2025).

Despite the fact that vertical motion couplets accompany both short-wave troughs and ridges, the latter receive far less attention from the research and operational forecasting communities. It is possible that this is, in part, because short-wave ridge features are actually quite rare.

Consider a simple geostrophic flow for which the relative vorticity is

$$\zeta_g \approx \frac{1}{f}\nabla^2\Phi, \tag{A.1}$$

where Φ is the geopotential defined $\Phi = \Phi_0 \cos(kx)$ where k is the zonal wavenumber and x is a zonal distance. The second derivative of Φ with respect to x is $-k^2\Phi$ such that

$$\zeta_g = -\frac{k^2\Phi}{f}. \tag{A.2}$$

Assuming upper-level height perturbations are on the order of 100 meters, we can approximate the absolute vorticity as a function of planetary wavenumber (Fig. A.1).

This simple analysis reveals that shortwave ridge features become inertially unstable near wavenumber 15, or a wavelength of about 2000 km, approximately the zonal scale of the Laurentian Great Lakes region. While this simple analysis is only an approximation (we made a somewhat arbitrary choice of Φ), anticyclones are anticipated to exist across a

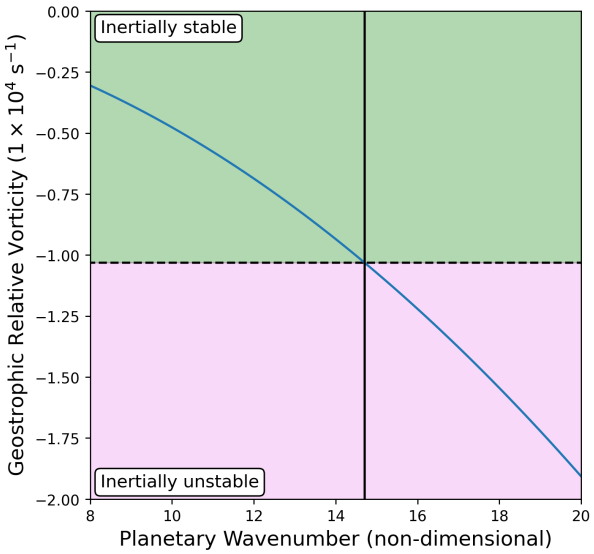

FIGURE A.1: Geostrophic relative vorticity as a function of planetary wavenumber (solid blue). The size of the Coriolis parameter (dashed black, estimated for 45°N) delineates inertial stability (colored green) and instability (colored pink). The wavenumber at which shortwave ridges become inertially unstable is identified with the vertical black line.

smaller range of wavenumbers than their cyclonic counterparts. Indeed, inertial instability can be thought of as a governor which limits the growth of anticyclonic disturbances.

A.2 Feature persistence in the tropics

Since basic inertial instability criteria are derived under geostrophic assumptions, their meteorological significance at low latitudes are not always clear. While there are instances where balanced, cross-equatorial flow leads to large-scale regions of inertial instability (Dunkerton, 1981, Thompson et al., 2018), it is worth exploring the e-folding time for tropical inertial instability,

$$\tau_i = \frac{1}{\sqrt{(f\eta)}} \tag{A.3}$$

using the full absolute vorticity (η) for a flow in gradient balance. Assuming the absolute vorticity is a small residual arising from the sum of relative vorticity and f, at 10°N τ_i scales like

$$\tau_i = \frac{1}{\sqrt{(1 \times 10^{-6}\ \mathrm{s}^{-1})(2.5 \times 10^{-5}\ \mathrm{s}^{-1})}}, \tag{A.4}$$

an e-folding time of approximately 2 days. As seen in Fig. 2.3, this e-folding time increases rapidly with decreasing latitude, especially so in the deep tropics.

There is compelling evidence that the far-western, subtropical North Pacific features upper-level inertial instability nearly 30% of the wintertime (Sato and Dunkerton, 2002, Thompson et al., 2018). This is a hemispheric maximum in event occurrence at those

latitudes and is attributed to the northward branch of the Hadley circulation. In their analysis, Sato and Dunkerton (2002) considered parcel trajectories within this unstable region, all of which could be traced back to the equatorial lower troposphere south of Japan within a few days. Many were eventually involved in layered disturbances in the upper-troposphere attributed to the release of inertial instability. Their results are generally consistent with the notion that unstable perturbations develop very slowly in the deep tropics.

Appendix B

Supporting information for Ch. 2

B.1 Comparison of tilting terms

In Eq. (2.14), the vorticity tendency associated with tilting (the third term on the rhs) was calculated as

$$\text{tilting} = \hat{k} \cdot \left(\frac{\partial \mathbf{V_g}}{\partial p} \times \nabla \omega_{\text{qg}} \right), \tag{B.1}$$

where $\frac{\partial \mathbf{V_g}}{\partial p}$ is the vertical shear of the geostrophic wind (i.e. the thermal wind). This is representative of the large-scale horizontal vorticity for QG phenomena such as straight jet streaks, and could be calculated identically using the thermal wind relation. Since

there is non-negligible ageostrophy in the jet entrance and trough regions, it is illustrative to also calculate the tilting term using the full vertical shear ($\frac{\partial \mathbf{V}}{\partial p}$). Further, since $\omega_{\rm qg}$ is only a portion of the full ω field, it is also illustrative to calculate the tilting term using the full vertical shear and the full vertical motion. We have performed these calculations using JRA3Q data for 12Z on 8 April 2013 and provide them in an analysis similar to Fig. 2.6.

Fig. B.1a & d are as in Fig. 2.6c & f and feature the full geostrophic relative vorticity, horizontal vortex tubes associated with the geostrophic shear, and the tilting term as described in Eq. (B.1). Fig. B.1b & e include the full relative vorticity, horizontal vortex tubes associated with the full vertical shear, and the tilting term calculated as the action of differential $\omega_{\rm qg}$ on those vortex tubes. Although the strength of this tilting process is weaker, the distribution is remarkably similar in that the 732–714 dam isohypses experience an anticyclonic absolute vorticity tendency on the order of 1–2 $\times$ 10^{-9} s^{-2} upstream of the unstable region. This indicates that while ageostrophy is non-negligible, the large-scale process which conspires to produce anticyclonic absolute vorticity is well diagnosed using a QG perspective.

Finally, Fig. B.1c & f contain the full relative vorticity, horizontal vortex tubes associated with the full shear, and the tilting term calculated as the action of differential JRA3Q model ω on the full horizontal vorticity. There is a substantial disparity between JRA3Q model vertical motion and that arising from the Sutcliffe-Trenberth form of $\omega_{\rm qg}$. Given substantially weaker subsidence, the resulting tilting term is only on the order of $.5 \times 10^{-9}$

s^{-2}, though some similarities in the broader distribution remain upstream of the trough axis. A full vorticity budget using JRA3Q model ω in this scenario yields disquieting results; the anticyclonic absolute vorticity feature goes unexplained.

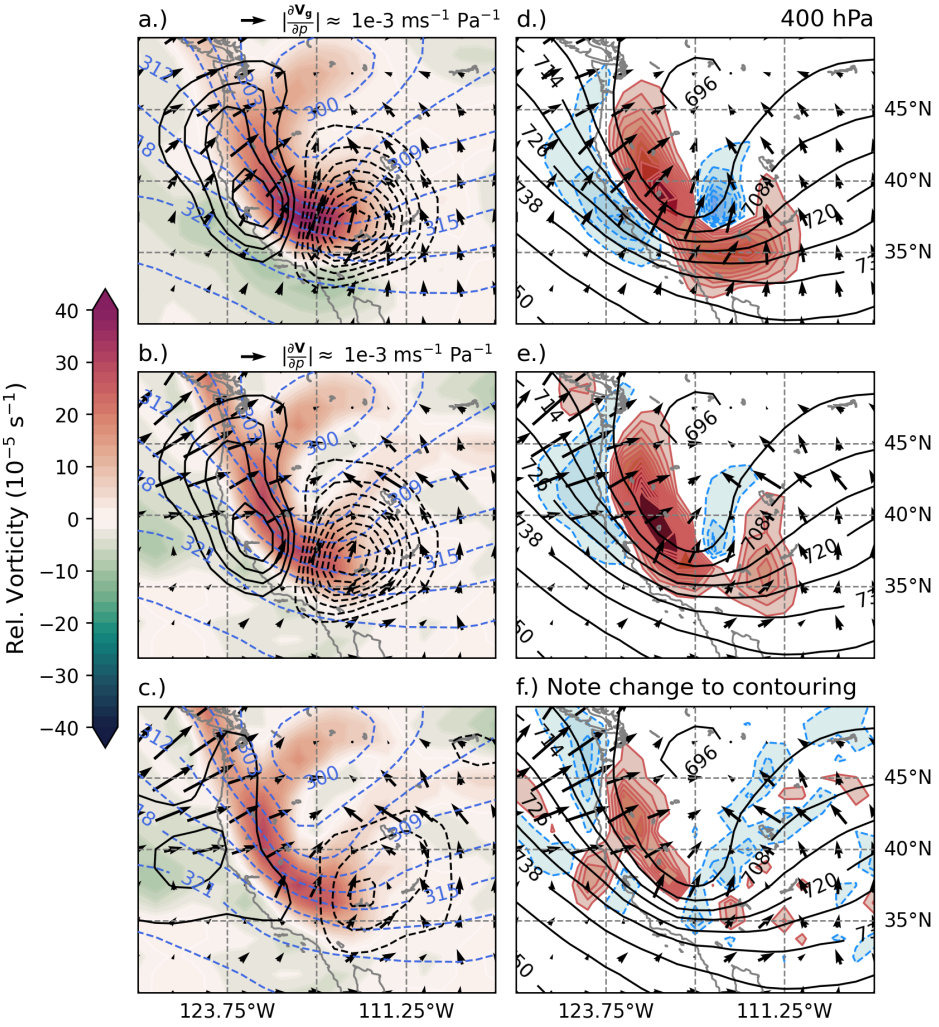

FIGURE B.1: a.) 400 hPa isentropes (dashed blue every 3 K), geostrophic relative vorticity (shaded), horizontal vortex tubes arising from the geostrophic vertical shear (black arrows) and QG vertical motion (black contours every 2 dPa s^{-1} from 2 and -2 dPa s^{-1}) at 12Z on 8 April 2013. b.) as in a.) except with the full relative vorticity and horizontal vortex tubes arising from the full vertical shear. c.) as in b.) except with the full JRA3Q vertical motion. d.) 400 hPa isohypses (solid black every 6 dam), horizontal vortex tubes arising from the geostrophic vertical shear (black arrows), and the vorticity tendency (shaded blues and reds every 1 $\times 10^{-9}$ s^{-2} from -1 and 1 $\times 10^{-9}$ s^{-2}, respectively) associated with tilting of the geostrophic vertical shear by the QG vertical motion. e.) as in d.) except for the vorticity tendency associated with tilting of the full vertical shear by the QG vertical motion. f.) as in d.) except for the vorticity tendency associated with tilting of the full vertical shear by JRA3Q model vertical motion (shaded blues and reds every 1 $\times 10^{-9}$ s^{-2} from -0.5 and 0.5 $\times 10^{-9}$ s^{-2}, respectively).

B.2 Comparison of vertical motion fields for the idealized simulation

The adiabatic vertical motion was calculated for the idealized case using the adiabatic thermodynamic energy equation (Martin, 2006a, their Eq. 4.10) re-written as,

$$\omega_{\mathrm{a}} = \sigma_p^{-1} \left[\frac{\partial T}{\partial p} + \mathbf{V}_h \cdot \nabla_h T \right] \tag{B.2}$$

where ω_{a} is the adiabatic vertical motion, T is the temperature, $\mathbf{V}_h$ is the horizontal wind, ∇_h is the two-dimensional gradient operator, and $\sigma_p = \left(\frac{\rho^{-1}}{C_p} - \frac{\partial T}{\partial p} \right)$, where C_p is the specific heat of dry air at constant pressure. ω_{a} was substituted for ω_{qg} in Eqs. (2.14) & (2.15) to produce an analysis similar to Fig. 2.10. While the ω_{a} maximum is smaller by about 1 dPa s^{-1} compared to that associated with ω_{qg} between F42 and F54, the distribution is very similar (Fig. B.2 and 2.10). This results in a strong likeness between the anticyclonic tilting tendency associated with each vertical motion field. Regardless of which vertical motion field is used, tilting explains the majority of the vorticity tendency upstream of the unstable regions.

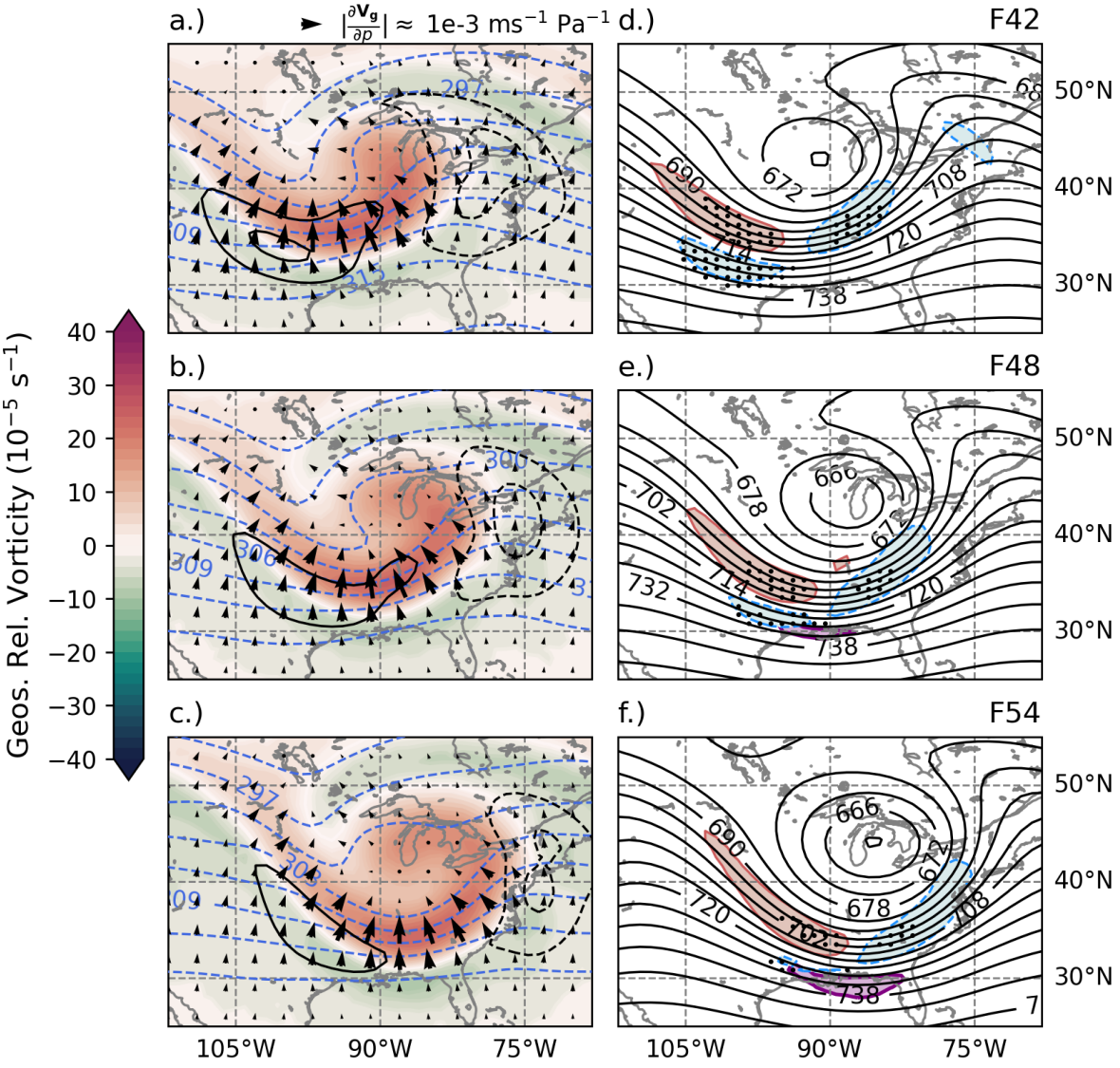

FIGURE B.2: a.) As in Fig. 2.6c except with ω_a instead of ω_{qg}, and averaged over the 450–350 hPa layer at F42, the 6-hr forecast period immediately before anticyclonic geostrophic absolute vorticity arises in the idealized UW-NMS simulation (see Fig. 2.9f). b-c.) as in a.) except for F48 and F54, respectively. d.) as in Fig. 2.6f except for tilting associated with ω_a and averaged over the 450–350 hPa layer at F42. Grid points wherein $\text{Proj}_t > 0.66$ (see Eq. 2.15, except calculated using ω_a) are stippled (black dots) only where the vorticity tendency associated with tilting processes is $> |0.25 \times 10^{-9}|$ s^{-2}. e-f.) as in d.) except for F48 and F54, respectively.

B.3 Comparison of absolute vorticity using geostrophic and full winds

Subgeostrophy in the trough region is such that critical points in geostrophic absolute vorticity (η_g) are of greater magnitude than those associated with the full absolute vorticity (η). While we have chosen a traditional instability criterion dependent on the geostrophic absolute vorticity, it is worth indicating that instability occurred during the April 2013 case regardless of which vorticity is employed. Fig. B.3 contains analyses of absolute vorticity for several 6-hr analysis periods immediately after a strong anticyclonic absolute vorticity tendency was diagnosed at 12Z 8 April 2013. Since this mechanism can be qualitatively diagnosed from maps of isentropes and upper-level geostrophic absolute vorticity (see Section 2.6.1), this anticyclonic tendency continued through 06Z on 9 April 2013 (Fig. B.3b-d) and resulted in inertially unstable regions in both the JRA3Q and ERA5 analyses.

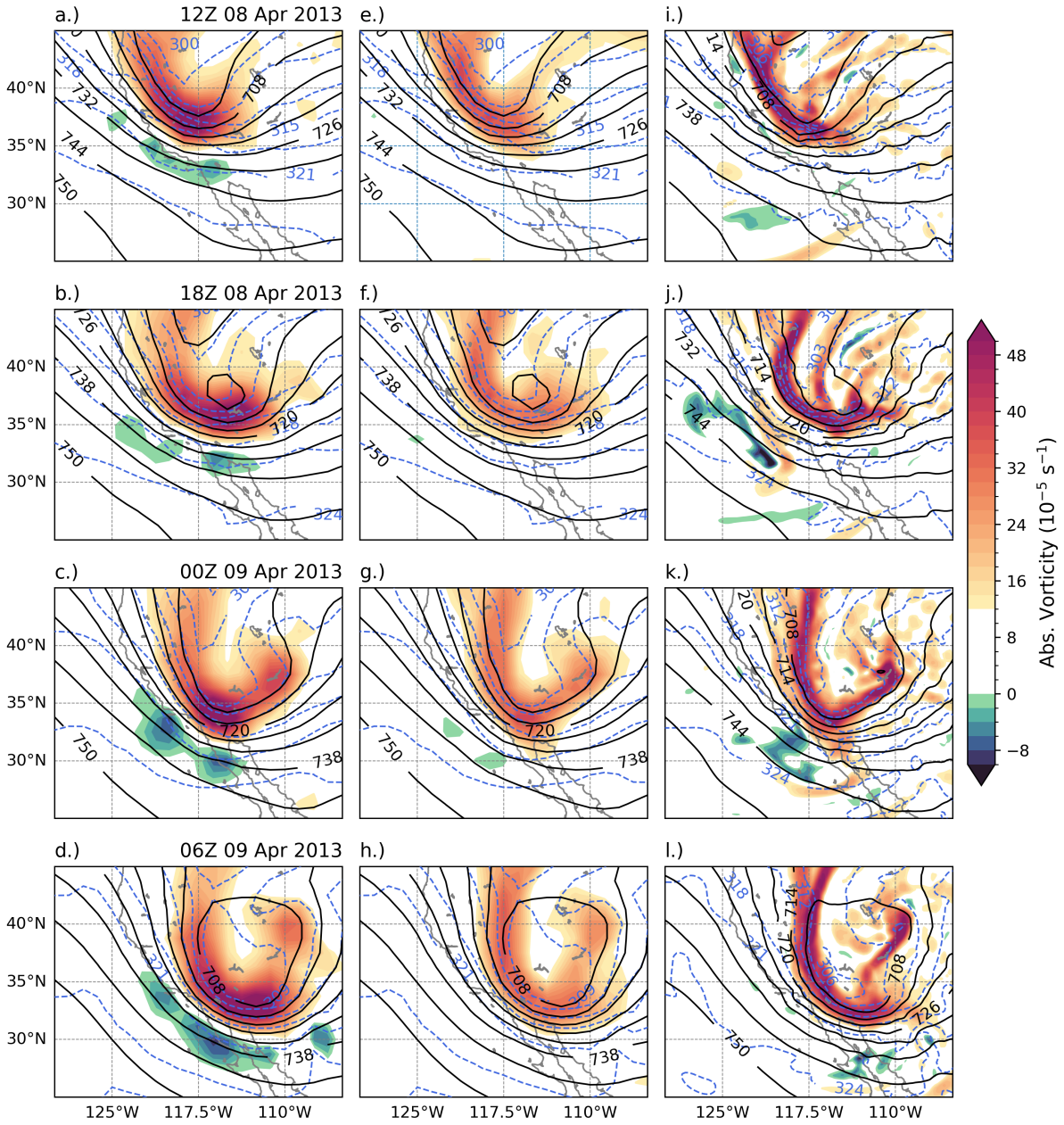

FIGURE B.3: a-d.) as in Fig. 2.2 except for a sub-region surrounding the upper-level jet/trough couplet and at the posted time using JRA3Q data. e-h.) as in a-d.) except for the absolute vorticity associated with the full wind using JRA3Q data. i-l.) as in e-h.) except for the potential temperature, geopotential height, and full absolute vorticity in the ERA5.

Appendix C

Supporting information for Ch. 3

C.1 Alternate calculations for the MPV and PV tendency

In order to support our calculation of the MPV and PV pseudo-tendencies [see Eq. (3.10)], these were compared to independent tendency calculations. Since MPAS natively calculates Ertel's PV and its diabatic tendency, the latter can be acquired directly from the model output or calculated as

$$\frac{dP}{dt} = \frac{\Delta P}{\Delta t} \tag{C.1}$$

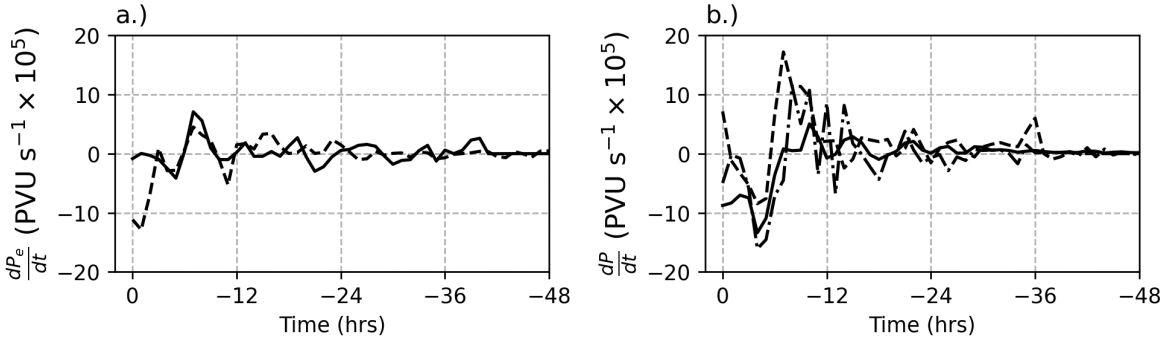

FIGURE C.1: a.) The MPV pseudo-tendency (solid) and the along-trajectory MPV tendency (dashed) for the average parcel with NPV < -0.4 PVU over the trajectory period ($N_{\text{sNPV}} = 1286$). b.) as in a.) except for the PV pseudo-tendency (solid), the along-trajectory PV tendency (dashed) and the model-output PV tendency (dash-dotted).

where ΔP is the 3-hour centered difference in PV and Δt is the hourly timestep. These were averaged over all sNPV parcels and denoted the "model-output" and "along-trajectory" PV tendencies, respectively. An along-trajectory MPV tendency can be calculated by substituting P_e for the P in Eq. C.1, having calculated that quantity in MPAS' native vertical coordinate using the chain rule.

Given the relatively substantial computational expense of initializing Lagranto and tracing variables along 3×10^5 trajectories (see Chapter 3.3.3), these calculations were performed on Lagranto trajectory output for 1000 equally-spaced parcels initialized every 100 m from 7 to 14.5 km for the same geodesic and period described in Chapter 3.2.3. The close agreement between pseudo-tendencies included in Fig. 3.11e-f & Fig. C.1a-b indicate that both analyses are relatively robust to choice of sample size at such large N.

The PV pseudo-tendency may underestimate the size of the positive PV tendency when

the parcel is beneath the diabatic heating maximum associated with latent heat release at 15Z 23 Sep (-9 hours, Fig. C.1b), potentially indicating the importance of horizontal components of the PV tendency in that region. This analysis also indicates that the MPV pseudo-tendency may underestimate the true MPV tendency from 21Z 23 Sep to 00Z 24 Sep (0 to -3 hours, Fig. C.1a).

Given strong agreement between the two MPV tendencies from -12 to -9 hours, and stronger disagreement from -3 to 0 hours, we rely on the MPV pseudo-tendency when forming conclusions as its size agrees more closely with scalings introduced in Chapter 3.2.3. This, in turn, leads to the more conservative conclusion that MPV outflow exists because of strongly negative initial values rather than strong MPV "erosion" above a region of heating associated with ice/precipitation processes. That said, there is clearly some uncertainty which reinforces the need for future work as discussed in Chapter 3.5.2. Regardless, the strongly negative MPV tendency is short-lived, the time-integrated effect remains small and conclusions discussed in Chapters 3.4 & 3.5 remain unchanged.

Bibliography

Adames, Á. F., 2017: Precipitation Budget of the Madden–Julian Oscillation. *Journal of the Atmospheric Sciences*, **74**, 1799–1817, doi:10.1175/JAS-D-16-0242.1.

— 2022: The Basic Equations under Weak Temperature Gradient Balance: Formulation, Scaling, and Types of Convectively Coupled Motions. *Journal of the Atmospheric Sciences*, **79**, 2087–2108, doi:10.1175/JAS-D-21-0215.1.

Adames, Á. F., R. M. V. Martes, H. Luo, and R. B. Rood, 2022: Moist Static Potential Vorticity Budget in Tropical Motion Systems. *Journal of the Atmospheric Sciences*, **79**, 763–779, doi:10.1175/JAS-D-21-0161.1.

Andersen, J. A. and Z. Kuang, 2012: Moist Static Energy Budget of MJO-like Disturbances in the Atmosphere of a Zonally Symmetric Aquaplanet. *Journal of Climate*, **25**, 2782–2804, doi:10.1175/JCLI-D-11-00168.1.

Anthes, R. A., 1972: Development of Asymmetries in a Three-Dimensional Numerical Model of the Tropical Cyclone[1]. *Mon. Wea. Rev.*, **100**, 461–476, doi:10.1175/1520-0493(1972)100¡0461:DOAIAT¿2.3.CO;2.

Arnold, N. P., M. Branson, Z. Kuang, D. A. Randall, and E. Tziperman, 2015: MJO Intensification with Warming in the Superparameterized CESM. *Journal of Climate*, **28**, 2706–2724, doi:10.1175/JCLI-D-14-00494.1.

Beckley, I. C. and Á. F. A. Corraliza, 2026: Persistence and adiabatic generation of inertial instability on the equatorward side of upper-level jet streaks. *Journal of the Atmospheric Sciences*, **83**, 517–534, doi:10.1175/JAS-D-25-0129.1.

Beckley, I. C., N. D. Metz, J. R. Klein, G. A. Linscott, S. A. Callahan, and E. P. Morrill, 2025: Interactions between Short-Wave Troughs and Shore-Parallel Lake-Effect Bands over Lake Ontario. *Weather and Forecasting*, **40**, 2079–2087, doi:10.1175/WAF-D-24-0247.1.

Bell, G. D. and D. Keyser, 1993: Shear and Curvature vorticity and Potential-Vorticity Interchanges: Interpretation and Application to a Cutoff Cyclone Event. *Mon. Wea. Rev.*, **121**, 76–102, doi:10.1175/1520-0493(1993)121¡0076:SACVAP¿2.0.CO;2.

Black, P. G. and R. A. Anthes, 1971: On the Asymmetric Structure of the Tropical Cyclone Outflow Layer. *J. Atmos. Sci.*, **28**, 1348–1366, doi:10.1175/1520-0469(1971)028¡1348:OTASOT¿2.0.CO;2.

Blanchard, D. O., W. R. Cotton, and J. M. Brown, 1998: Mesoscale Circulation Growth under Conditions of Weak Inertial Instability. *Mon. Wea. Rev.*, **126**, 118–140, doi:10.1175/1520-0493(1998)126¡0118:MCGUCO¿2.0.CO;2.

Bolton, D., 1980: The Computation of Equivalent Potential Temperature. *Mon. Wea. Rev.*, **108**, 1046–1053, doi:10.1175/1520-0493(1980)108¡1046:TCOEPT¿2.0.CO;2.

Bryan, G. H., 2008: On the Computation of Pseudoadiabatic Entropy and Equivalent Potential Temperature. *Monthly Weather Review*, **136**, 5239–5245, doi:10.1175/2008MWR2593.1.

Carlson, T. N., 1980: Airflow Through Midlatitude Cyclones and the Comma Cloud Pattern. *Mon. Wea. Rev.*, **108**, 1498–1509, doi:10.1175/1520-0493(1980)108¡1498:ATMCAT¿2.0.CO;2.

Charney, J. G., 1947: THE DYNAMICS OF LONG WAVES IN A BARO-CLINIC WESTERLY CURRENT. *J. Meteor.*, **4**, 136–162, doi:10.1175/1520-0469(1947)004¡0136:TDOLWI¿2.0.CO;2.

Chen, H. and D.-L. Zhang, 2013: On the Rapid Intensification of Hurricane Wilma (2005). Part II: Convective Bursts and the Upper-Level Warm Core. *Journal of the Atmospheric Sciences*, **70**, 146–162, doi:10.1175/JAS-D-12-062.1.

Ciesielski, P. E., D. E. Stevens, R. H. Johnson, and K. R. Dean, 1989: Observational Evidence for Asymmetric Inertial Instability. *J. Atmos. Sci.*, **46**, 817–831, doi:10.1175/1520-0469(1989)046¡0817:OEFAII¿2.0.CO;2.

Clarke, S. J., S. L. Gray, and N. M. Roberts, 2019: Downstream influence of mesoscale convective systems. Part 1: Influence on forecast evolution. *Quart J Royal Meteoro Soc*, **145**, 2933–2952, doi:10.1002/qj.3593.

Conzemius, R. J. and M. T. Montgomery, 2009: Clarification on the generation of absolute and potential vorticity in mesoscale convective vortices. *Atmos. Chem. Phys.*, **9**, 7591–7605, doi:10.5194/acp-9-7591-2009.

Cushman-Roisin, B. and J.-M. Beckers, 2011: *Introduction to Geophysical Fluid Dynamics: Physical and Numerical Aspects*. Academic Press, Waltham, MA, 2nd ed edition.

Dey, I. and M. O'Neill, 2022: Moist Potential Vorticity Diagnosis of the Tropical Cyclone Boundary Layer: Influence of Roll Vortices.

Dunkerton, T. J., 1981: On the Inertial Stability of the Equatorial Middle Atmosphere. *J. Atmos. Sci.*, **38**, 2354–2364, doi:10.1175/1520-0469(1981)038¡2354:OTISFT¿2.0.CO;2.

Eady, E. T., 1949: Long Waves and Cyclone Waves. *Tellus*, **1**, 33–52, doi:10.3402/tellusa.v1i3.8507.

Emanuel, K., T. Alberti, S. Bourdin, S. J. Camargo, D. Faranda, E. Flaounas, J. J. Gonzalez-Aleman, C.-Y. Lee, M. M. Miglietta, C. Pasquero, A. Portal, H. Ramsay, M. Reale, and R. Romero, 2025: CYCLOPs: A Unified Framework for Surface Flux-Driven Cyclones Outside the Tropics. *Weather Clim. Dynam.*, **6**, 901–926, doi:10.5194/wcd-6-901-2025.

Emanuel, K. A., 1979: Inertial Instability and Mesoscale Convective Systems. Part I: Linear Theory of Inertial Instability in Rotating Viscous Fluids. *J. Atmos. Sci.*, **36**, 2425–2449, doi:10.1175/1520-0469(1979)036¡2425:IIAMCS¿2.0.CO;2.

— 1986: An Air-Sea Interaction Theory for Tropical Cyclones. Part I: Steady-State Maintenance. *J. Atmos. Sci.*, **43**, 585–605, doi:10.1175/1520-0469(1986)043¡0585:AASITF¿2.0.CO;2.

Fleming, E. L., G.-H. Lim, and J. M. Wallace, 1987: Differences between the Spring and Autumn Circulation of the Northern Hemisphere. *J. Atmos. Sci.*, **44**, 1266–1286, doi:10.1175/1520-0469(1987)044¡1266:DBTSAA¿2.0.CO;2.

Grams, C. M. and H. M. Archambault, 2016: The Key Role of Diabatic Outflow in Amplifying the Midlatitude Flow: A Representative Case Study of Weather Systems Surrounding Western North Pacific Extratropical Transition. *Monthly Weather Review*, **144**, 3847–3869, doi:10.1175/MWR-D-15-0419.1.

Hakim, G. J., 2000: Climatology of Coherent Structures on the Extratropical Tropopause. *Monthly Weather Rev*, **128**, 385, doi:10.1175/1520-0493(2000)128¡0385:COCSOT¿2.0.CO;2.

Harr, P. A., R. L. Elsberry, and T. F. Hogan, 2000: Extratropical Transition of Tropical Cyclones over the Western North Pacific. Part II: The Impact of Midlatitude Circulation Characteristics. *Mon. Wea. Rev.*, **128**, 2634–2653, doi:10.1175/1520-0493(2000)128¡2634:ETOTCO¿2.0.CO;2.

Hart, R. E., 2003: A Cyclone Phase Space Derived from Thermal Wind and Thermal Asymmetry. *Mon. Wea. Rev.*, **131**, 585–616, doi:10.1175/1520-0493(2003)131¡0585:ACPSDF¿2.0.CO;2.

Harvey, B., J. Methven, C. Sanchez, and A. Schäfler, 2020: Diabatic generation of negative potential vorticity and its impact on the North Atlantic jet stream. *Quart J Royal Meteoro Soc*, **146**, 1477–1497, doi:10.1002/qj.3747.

Haynes, P. H. and M. E. McIntyre, 1987: On the Evolution of Vorticity and Potential Vorticity in the Presence of Diabatic Heating and Frictional or Other Forces. *J. Atmos. Sci.*, **44**, 828–841, doi:10.1175/1520-0469(1987)044¡0828:OTEOVA¿2.0.CO;2.

Hersbach, H., B. Bell, P. Berrisford, S. Hirahara, A. Horányi, J. Muñoz-Sabater, J. Nicolas, C. Peubey, R. Radu, D. Schepers, A. Simmons, C. Soci, S. Abdalla, X. Abellan, G. Balsamo, P. Bechtold, G. Biavati, J. Bidlot, M. Bonavita, G. De Chiara, P. Dahlgren, D. Dee, M. Diamantakis, R. Dragani, J. Flemming, R. Forbes, M. Fuentes, A. Geer, L. Haimberger, S. Healy, R. J. Hogan, E. Hólm, M. Janisková, S. Keeley, P. Laloyaux, P. Lopez, C. Lupu, G. Radnoti, P. de Rosnay, I. Rozum, F. Vamborg, S. Villaume, and J.-N. Thépaut, 2020: The ERA5 global reanalysis. *Quart J Royal Meteoro Soc*, **146**, 1999–2049, doi:10.1002/qj.3803.

Holton, J. R., 1979: *An Introduction to Dynamic Meteorology*. Number 23 in International Geophysics Series, Acad. Press, New York, 2. ed edition.

Holton, J. R. and G. Hakim, 2013: *An Introduction to Dynamic Meteorology*. Academic Press, Amsterdam, 5. ed edition.

Hoskins, B. J. and K. I. Hodges, 2005: A New Perspective on Southern Hemisphere Storm Tracks. *Journal of Climate*, **18**, 4108–4129, doi:10.1175/JCLI3570.1.

Hoskins, B. J., M. E. McIntyre, and A. W. Robertson, 1985: On the use and significance of isentropic potential vorticity maps. *Quart J Royal Meteoro Soc*, **111**, 877–946, doi:10.1002/qj.49711147002.

Hoskins, B. J. and P. J. Valdes, 1990: On the Existence of Storm-Tracks. *J. Atmos. Sci.*, **47**, 1854–1864, doi:10.1175/1520-0469(1990)047¡1854:OTEOST¿2.0.CO;2.

Jiang, J. and Y. Wang, 2025: The Role of Outflow-Layer Inertial Stability in Governing the Radial Location of Secondary Eyewall Formation in Tropical Cyclones. *JGR Atmospheres*, **130**, e2025JD043708, doi:10.1029/2025JD043708.

Jordan, C. L., 1958: Mean Soudings for the West Indies Area. *J. Meteor.*, **15**, 91–97, doi:10.1175/1520-0469(1958)015¡0091:MSFTWI¿2.0.CO;2.

Kelley, O. A. and J. B. Halverson, 2011: How much tropical cyclone intensification can result from the energy released inside of a convective burst? *J. Geophys. Res.*, **116**, D20118, doi:10.1029/2011JD015954.

Kenneth, R., J. Howard, P. James, C. Michael, and J. Carl, 2019: International Best Track Archive for Climate Stewardship (IBTrACS) Project, Version 4.

Kleinschmidt, E., 1951: Grundlagen einer Theorie der tropischen Zyklonen. *Arch. Met. Geoph. Biokl. A.*, **4**, 53–72, doi:10.1007/BF02246793.

Knapp, K. R., H. J. Diamond, J. P. Kossin, M. C. Kruk, and C. J. Schreck, 2018: International Best Track Archive for Climate Stewardship (IBTrACS) Project, Version 4.

Knox, J. A., 1997: Possible Mechanisms of Clear-Air Turbulence in Strongly Anticyclonic Flows. *Mon. Wea. Rev.*, **125**, 1251–1259, doi:10.1175/1520-0493(1997)125¡1251:PMOCAT¿2.0.CO;2.

Knox, J. A. and V. L. Harvey, 2005: Global climatology of inertial instability and Rossby wave breaking in the stratosphere. *J. Geophys. Res.*, **110**, 2004JD005068, doi:10.1029/2004JD005068.

Kobayashi, S., Y. Ota, Y. Harada, A. Ebita, M. Moriya, H. Onoda, K. Onogi, H. Kamahori, C. Kobayashi, H. Endo, K. Miyaoka, and K. Takahashi, 2015: The JRA-55 Reanalysis: General Specifications and Basic Characteristics. *Journal of the Meteorological Society of Japan*, **93**, 5–48, doi:10.2151/jmsj.2015-001.

Kooloth, P., L. M. Smith, and S. N. Stechmann, 2024: Non-conservation and conservation for different formulations of moist potential vorticity. *Atmospheric Science Letters*, e1237, doi:10.1002/asl.1237.

Kosaka, Y., S. Kobayashi, Y. Harada, C. Kobayashi, H. Naoe, K. Yoshimoto, M. Harada, N. Goto, J. Chiba, K. Miyaoka, R. Sekiguchi, M. Deushi, H. Kamahori, T. Nakaegawa, T. Y. Tanaka, T. Tokuhiro, Y. Sato, Y. Matsushita, and K. Onogi, 2024: The JRA-3Q Reanalysis. *Journal of the Meteorological Society of Japan*, **102**, 49–109, doi:10.2151/jmsj.2024-004.

Li, Y., Y. Wang, and Z.-M. Tan, 2023: Is the Outflow-Layer Inertial Stability Crucial to the Energy Cycle and Development of Tropical Cyclones? *Journal of the Atmospheric Sciences*, **80**, 1605–1620, doi:10.1175/JAS-D-22-0186.1.

Lojko, A., A. Payne, and C. Jablonowski, 2022: The Remote Role of North-American Mesoscale Convective Systems on the Forecast of a Rossby Wave Packet: A Multi-Model Ensemble Case-Study. *JGR Atmospheres*, **127**, e2022JD037171, doi:10.1029/2022JD037171.

Lojko, A., A. C. Winters, A. Oertel, C. Jablonowski, and A. E. Payne, 2024: An ERA5 Climatology of Synoptic-Scale Negative Potential Vorticity-Jet Interactions over the Western North Atlantic. Preprint, Dynamical processes in midlatitudes.

Manney, G. L. and M. I. Hegglin, 2018: Seasonal and Regional Variations of Long-Term Changes in Upper-Tropospheric Jets from Reanalyses. *Journal of Climate*, **31**, 423–448, doi:10.1175/JCLI-D-17-0303.1.

Marquet, P., 2014: On the definition of a moist-air potential vorticity. *Quart J Royal Meteoro Soc*, **140**, 917–929, doi:10.1002/qj.2182.

Martin, J. E., 2006a: *Mid-Latitude Atmospheric Dynamics: A First Course*. J. Wiley & sons, Chichester.

— 2006b: The Role of Shearwise and Transverse Quasigeostrophic Vertical Motions in the Midlatitude Cyclone Life Cycle. *Monthly Weather Review*, **134**, 1174–1193, doi:10.1175/MWR3114.1.

— 2014: Quasi-geostrophic Diagnosis of the Influence of Vorticity Advection on the Development of Upper Level Jet-front Systems: Vorticity Advection and Upper Level Jet-Front Systems. *Q.J.R. Meteorol. Soc.*, **140**, 2658–2671, doi:10.1002/qj.2333.

— 2021: Recent Trends in the Waviness of the Northern Hemisphere Wintertime Polar and Subtropical Jets. *JGR Atmospheres*, **126**, e2020JD033668, doi:10.1029/2020JD033668.

Martin, J. E. and T. Norton, 2023: Waviness of the Southern Hemisphere wintertime polar and subtropical jets. *Weather Clim. Dynam.*, **4**, 875–886, doi:10.5194/wcd-4-875-2023.

Martínez-Alvarado, O., S. L. Gray, and J. Methven, 2016: Diabatic Processes and the Evolution of Two Contrasting Summer Extratropical Cyclones. *Mon. Wea. Rev.*, **144**, 3251–3276, doi:10.1175/MWR-D-15-0395.1.

May, R., S. Arms, P. Marsh, E. Bruning, J. Leeman, Z. Bruick, and M. D. Camron, 2016: MetPy: A Python Package for Meteorological Data. [object Object].

May, R. M., K. H. Goebbert, J. E. Thielen, J. R. Leeman, M. D. Camron, Z. Bruick, E. C. Bruning, R. P. Manser, S. C. Arms, and P. T. Marsh, 2022: MetPy: A Meteorological Python Library for Data Analysis and Visualization. *Bulletin of the American Meteorological Society*, **103**, E2273–E2284, doi:10.1175/BAMS-D-21-0125.1.

Mayta, V. C. and Á. F. Adames, 2023: Moist Thermodynamics of Convectively Coupled Waves over the Western Hemisphere. *Journal of Climate*, **36**, 2765–2780, doi:10.1175/JCLI-D-22-0435.1.

Mogil, M. and R. L. Holle, 1972: Anomalous Gradient Winds: Existence and Implications. *Mon. Wea. Rev.*, **100**, 709–716, doi:10.1175/1520-0493(1972)100¡0709:AGWEAI¿2.3.CO;2.

Morris, F., C. M. Robinson, M. Reeder, J. Schwendike, D. J. Parker, C. L. Bain, and C. J. Short, 2025: Closing the Circulation Budget. *JGR Atmospheres*, **130**, doi:10.1029/2024jd041738.

Oertel, A., M. Boettcher, H. Joos, M. Sprenger, and H. Wernli, 2020: Potential vorticity structure of embedded convection in a warm conveyor belt and its relevance for large-scale dynamics. *Weather Clim. Dynam.*, **1**, 127–153, doi:10.5194/wcd-1-127-2020.

Oertel, A., M. Sprenger, H. Joos, M. Boettcher, H. Konow, M. Hagen, and H. Wernli, 2021: Observations and simulation of intense convection embedded in a warm conveyor belt – how ambient vertical wind shear determines the dynamical impact. *Weather Clim. Dynam.*, **2**, 89–110, doi:10.5194/wcd-2-89-2021.

Ooyama, K., 1969: Numerical Simulation of the Life Cycle of Tropical Cyclones. *J. Atmos. Sci.*, **26**, 3–40, doi:10.1175/1520-0469(1969)026¡0003:NSOTLC¿2.0.CO;2.

Ooyama, KV., 1987: Numerical experiments of steady and transient jets with simple model of the hurricane outflow layer. *Preprints, 17th Conf. on Hurricanes and Tropical Meteorology, Miami, FL, Amer. Meteor. Soc*, volume 318, 320.

Orr, L. J., 2024: *Characteristics of Northern Hemisphere Warm Season Tropopause-Level Jet and Associated Trends*. M.S. Thesis, Dept. of Atmospheric and Oceanic Sciences, University of Wisconsin-Madison.

Prince, K. C. and C. Evans, 2022: Convectively Generated Negative Potential Vorticity Enhancing the Jet Stream through an Inverse Energy Cascade during the Extratropical Transition of Hurricane Irma. *Journal of the Atmospheric Sciences*, **79**, 2901–2918, doi:10.1175/JAS-D-22-0094.1.

Rappin, E. D., M. C. Morgan, and G. J. Tripoli, 2011: The Impact of Outflow Environment on Tropical Cyclone Intensification and Structure. *Journal of the Atmospheric Sciences*, **68**, 177–194, doi:10.1175/2009JAS2970.1.

Reboita, M. S., W. Yanase, Z. Wang, C. Fogarty, R. Hart, R. McTaggart-Cowan, J. Beven, C. Earl-Spurr, E. Flauonas, P. Mukhopadhyay, N. A. Aziz, I. C. Beckley, N. Takamura, L. Li, and N. Caltabiano, 2026: Toward Unified Global Frameworks for Cyclone Classification and Phase Transitions. *Bulletin of the American Meteorological Society*, BAMS–D–26–0072.1, doi:10.1175/BAMS-D-26-0072.1.

Rotunno, R. and K. A. Emanuel, 1987: An Air–Sea Interaction Theory for Tropical Cyclones. Part II: Evolutionary Study Using a Nonhydrostatic Axisymmetric Numerical Model. *J. Atmos. Sci.*, **44**, 542–561, doi:10.1175/1520-0469(1987)044¡0542:AAITFT¿2.0.CO;2.

Rotunno, R., W. C. Skamarock, and C. Snyder, 1994: An Analysis of Frontogenesis in Numerical Simulations of Baroclinic Waves. *J. Atmos. Sci.*, **51**, 3373–3398, doi:10.1175/1520-0469(1994)051¡3373:AAOFIN¿2.0.CO;2.

Rowe, S. M. and M. H. Hitchman, 2016: On the Relationship between Inertial Instability, Poleward Momentum Surges, and Jet Intensifications near Midlatitude Cyclones. *Journal of the Atmospheric Sciences*, **73**, 2299–2315, doi:10.1175/JAS-D-15-0183.1.

— 2026: On the Diurnal Cycle in UTLS Mesoscale Potential Vorticity Variability Using 9-km Resolution ECMWF Operational Forecast Analyses: A Climatology of South Pacific Tropical Cyclones During 2016 – 2024. *Journal of the Atmospheric Sciences*, e240190, doi:10.1175/JAS-D-24-0190.1.

Ruppert, J. H., A. A. Wing, X. Tang, and E. L. Duran, 2020: The critical role of cloud–infrared radiation feedback in tropical cyclone development. *Proc. Natl. Acad. Sci. U.S.A.*, **117**, 27884–27892, doi:10.1073/pnas.2013584117.

Sato, K. and T. J. Dunkerton, 2002: Layered structure associated with low potential vorticity near the tropopause seen in high-resolution radiosondes over Japan. *Journal of the Atmospheric Sciences*, **59**, 2782–2800.

Sawada, M. and T. Iwasaki, 2007: Impacts of Ice Phase Processes on Tropical Cyclone Development. *Journal of the Meteorological Society of Japan*, **85**, 479–494, doi:10.2151/jmsj.85.479.

Schaefer, V. J. and W. E. Hubert, 1955: A case study of jet stream clouds. *Tellus*, **7**, 301–307, doi:10.3402/tellusa.v7i3.8906.

Schubert, W., 2004: A generalization of Ertel's potential vorticity to a cloudy, precipitating atmosphere. *metz*, **13**, 465–471, doi:10.1127/0941-2948/2004/0013-0465.

Schubert, W. H., S. A. Hausman, M. Garcia, K. V. Ooyama, and H.-C. Kuo, 2001: Potential Vorticity in a Moist Atmosphere. *J. Atmos. Sci.*, **58**, 3148–3157, doi:10.1175/1520-0469(2001)058¡3148:PVIAMA¿2.0.CO;2.

Schultz, D. M. and P. N. Schumacher, 1999: The Use and Misuse of Conditional Symmetric Instability. *Mon. Wea. Rev.*, **127**, 2709–2732, doi:10.1175/1520-0493(1999)127¡2709:TUAMOC¿2.0.CO;2.

Simpson, R. H., 1978: On The Computation of Equivalent Potential Temperature. *Mon. Wea. Rev.*, **106**, 124–130, doi:10.1175/1520-0493(1978)106¡0124:OTCOEP¿2.0.CO;2.

Skamarock, W., J. Klemp, J. Dudhia, D. Gill, D. Barker, W. Wang, X.-Y. Huang, and M. Duda, 2008: A Description of the Advanced Research WRF Version 3. Technical report, UCAR/NCAR.

Skamarock, W. C., J. B. Klemp, M. G. Duda, L. D. Fowler, S.-H. Park, and T. D. Ringler, 2012: A Multiscale Nonhydrostatic Atmospheric Model Using Centroidal Voronoi Tesselations and C-Grid Staggering. *Monthly Weather Review*, **140**, 3090–3105, doi:10.1175/MWR-D-11-00215.1.

Smith, R. K. and M. T. Montgomery, 2023: *Tropical Cyclones: Observations and Basic Processes*. Number 4 in Developments in Weather and Climate Science, Elsevier, Amsterdam$oOxford Cambridge.

Sobel, A. H., J. Nilsson, and L. M. Polvani, 2001: The Weak Temperature Gradient Approximation and Balanced Tropical Moisture Waves*. *J. Atmos. Sci.*, **58**, 3650–3665, doi:10.1175/1520-0469(2001)058¡3650:TWTGAA¿2.0.CO;2.

Sprenger, M. and H. Wernli, 2015: The LAGRANTO Lagrangian analysis tool – version 2.0. *Geosci. Model Dev.*, **8**, 2569–2586, doi:10.5194/gmd-8-2569-2015.

Steranka, J., E. B. Rodgers, and R. C. Gentry, 1986: The Relationship between Satellite Measured Convective Bursts and Tropical Cyclone Intensification. *Mon. Wea. Rev.*, **114**, 1539–1546, doi:10.1175/1520-0493(1986)114¡1539:TRBSMC¿2.0.CO;2.

Stone, P. H., 1966: On Non-Geostrophic Baroclinic Stability. *J. Atmos. Sci.*, **23**, 390–400, doi:10.1175/1520-0469(1966)023¡0390:ONGBS¿2.0.CO;2.

— 1972: On Non-Geostrophic Baroclinic Stability: Part III. The Momentum and Heat Transports. *J. Atmos. Sci.*, **29**, 419–426, doi:10.1175/1520-0469(1972)029¡0419:ONGBSP¿2.0.CO;2.

Storer, L. N., P. D. Williams, and M. M. Joshi, 2017: Global Response of Clear-Air Turbulence to Climate Change. *Geophysical Research Letters*, **44**, 9976–9984, doi:10.1002/2017GL074618.

Sutcliffe, R. C., 1947: A contribution to the problem of development. *Q.J Royal Met. Soc.*, **73**, 370–383, doi:10.1002/qj.49707331710.

Thompson, C. F. and D. M. Schultz, 2021: The Release of Inertial Instability Near an Idealized Zonal Jet. *Geophysical Research Letters*, **48**, e2021GL092649, doi:10.1029/2021GL092649.

Thompson, C. F., D. M. Schultz, and G. Vaughan, 2018: A Global Climatology of Tropospheric Inertial Instability. *Journal of the Atmospheric Sciences*, **75**, 805–825, doi:10.1175/JAS-D-17-0062.1.

Trenberth, K. E., 1978: On the Interpretation of the Diagnostic Quasi-Geostrophic Omega Equation. *Mon. Wea. Rev.*, **106**, 131–137, doi:10.1175/1520-0493(1978)106¡0131:OTIOTD¿2.0.CO;2.

Tripoli, G. J., 1992: An explicit three-dimensional nonhydrostatic numerical simulation of a tropical cyclone. *Meteorl. Atmos. Phys.*, **49**, 229–254, doi:10.1007/BF01025409.

Tripoli, G. J. and W. R. Cotton, 1981: The Use of Ice-Liquid Water Potential Temperature as a Thermodynamic Variable In Deep Atmospheric Models. *Mon. Wea. Rev.*, **109**, 1094–1102, doi:10.1175/1520-0493(1981)109¡1094:TUOLLW¿2.0.CO;2.

van Mieghem, J., 1951: Hydrodynamic instability. *Amer. Met. Soc.*, **753**, 434–453.

Wang, S., M. T. Montgomery, and R. K. Smith, 2021: Solutions of the Eliassen balance equation for inertially and/or symmetrically stable and unstable vortices. *Quart J Royal Meteoro Soc*, **147**, 2760–2771, doi:10.1002/qj.4098.

Wayne, H., Schubert, and B. T. Alworth, 1987: Evolution of potential vorticity in tropical cyclones. *Quart J Royal Meteoro Soc*, **113**, 147–162, doi:10.1002/qj.49711347509.

Williams, P. D., 2017: Increased light, moderate, and severe clear-air turbulence in response to climate change. *Adv. Atmos. Sci.*, **34**, 576–586, doi:10.1007/s00376-017-6268-2.

Yanai, M., 1964: Formation of tropical cyclones. *Reviews of Geophysics*, **2**, 367–414, doi:10.1029/RG002i002p00367.